Ultrafast Modulation of electronic Structure by coherent Phonon Excitations in ionic Crystals

zur Erlangung des akademischen Grades

doctor rerum naturalium
(Dr. rer. nat.)
im Fach Physik

eingereicht an der
Mathematisch-Naturwissenschaftlichen Fakultät
Institut für Physik
Humboldt-Universität zu Berlin

Präsidentin der Humboldt-Universität zu Berlin
Prof. Dr.-Ing. Dr. Sabine Kunst

Dekan der Mathematisch-Naturwissenschaftlichen Fakultät
Prof. Dr. Elmar Kulke

vorgelegt von
Master of Science
Jannick Weißhaupt

Gutachter:	1. Prof. Dr. Thomas Elsässer
	2. Prof. Dr. Majed Chergui
	3. Prof. Dr. Oliver Benson
Eingereicht am:	29.03.2019
Tag der Disputation:	19.07.2019

Contents

Abstract

This thesis explores the subtle interplay between electronic and nuclear excitation in the Raman effect with time resolved extreme ultraviolet (XUV) absorption spectroscopy. Coherent stimulated Raman scattering, the type of Raman interaction we induce, is a variant of the well known Raman scattering, where a sufficiently short pulse excites nuclear vibrations coherently, i.e. with actual displacement of the nuclei. In standard Raman scattering, due to its incoherent, spontaneous nature, there is no displacement of nuclei. We were able to observe nuclear displacements as small as 10^{-4} Å in real time by their effect on the XUV absorption spectrum. Specifically we studied non-resonant near infrared (NIR) pump XUV probe absorption spectroscopy on lithium borohydride ($LiBH_4$).

Lithium borohydride is an ionic insulator with ~ 7 eV band gap, which is more than four times the photon energy of the pump pulse, which excludes direct excitations of electrons through multi-photon absorption into the conduction band. The exact electronic response of lithium borohydride upon excitation with a NIR pump pulse has been studied by Stingl et. al [SZF+12] with time resolved x-ray diffraction. They observed a quasi-instantaneous electron transfer from BH_4^- anion to Li cation, which is responsible for the relatively large dielectric function, compared to the intra-molecular polarizability of the BH_4^- group alone. This ultrafast induced polarization, or in other words transient electron density, exerts a force onto the nuclei, which are accelerated.

In the XUV absorption experiments in this thesis we concentrate on the Lithium K-edge absorption spectrum around 60 eV, which consists of a strong excitonic peak at the onset of absorption and a plateau at higher energies. Upon excitation with a NIR pulse we observe oscillatory changes in the absorption spectrum with a frequency of 10 THz, which we identify as the effect of coherent phonon excitations of an external A_g phonon mode. The coherent oscillation changes the distance between Li^+ anions and BH_4^- cations, which modifies the electronic environment around the Li anion. XUV absorption spectroscopy, especially x-ray absorption near edge spectroscopy (XANES), is highly sensitive to such changes of the chemical environment around the absorbing atom. We use two different approaches to derive the absolute displacement, which are observed in the experiment.

Our results allow for a fascinating new insight into Raman scattering as they connect a direct observation of the driving mechanism, the induced polarization, with a direct observation of the outcome the oscillatory nuclear displacement. With XUV absorption spectroscopy nuclear displacements in the order of 10^{-4} Å were resolved with sub picosecond accuracy in the time domain.

Zusammenfassung

Diese Arbeit untersucht den subtilen Zusammenhang von elektronischer und nukleare Anregung beim Raman-Effekt mit der Methode der zeitaufgelösten harten UV-Spektroskopie. Wir verwenden kohärente stimulierte Raman-Streuung, ein Spezialfall der weit verbreiteten normalen Raman-Streuung. Bei dieser regt ein hinreichend kurzer kohärenter Lichtimpuls Schwingungen der Kerne an, bei denen die Kerne messbar ausgelenkt werden, wohingegen die Auslenkungen bei normaler Raman-Streuung, wegen deren inkohärenten spontanen Natur, nicht messbar sind. Wir konnten Auslenkung kleiner als 10^{-4} Å in Echtzeit durch ihren Effekt auf das harte UV-Spektrum nachweisen. Diese Ergebnisse konnten mit Lithiumborhydrid als Probe und nicht-resonanter naher Infrarotstrahlung als Anrege-und harter UV-Strahlung als Abfrageimpuls erzielt werden.

Lithiumborhydrid ist ein ionischer Isolator mit etwa 7 eV Bandlücke. Die Bandlücke beträgt somit mehr als vier mal die Photonenenergie des Anregeimpulses, was eine direkte Anregung von Elektronen in das Leitungsband durch Mehrphotonenabsorption ausschließt. Die genaue elektronische Reaktion Lithiumborhydrids auf Anregung durch nahes Infrarotlicht wurde von Stingl et. al. [SZF$^+$12] mit zeitaufgelöster Röntgenbeugung untersucht. Stingl et. al. wiesen einen quasi-instantanen Elektronentransfer vom BH_4^- Anion zum Lithium Kation nach, welcher für die hohe dielektrische Konstante im Vergleich zur puren molekularen Polarisierbarkeit des BH_4^- Tetraeders verantwortlich ist. Diese ultrakurze induzierte Polarisation, oder transiente Elektronendichte, übt eine Kraft auf die Kerne aus, welche dadurch beschleunigt werden und zu schwingen beginnen.

Zum Nachweis dieses Prozesses verwenden wir harte UV-Absorptionsspektroskopie an der Lithium K-Kante von Lithiumborhydrid bei 60 eV. Das Absorptionsspektrum besteht aus einem starken exzitonischen Anteil zu Beginn der Absorption und einem Plateau bei höheren Energien. Bei Anregung durch einen NIR-Impuls beobachteten wir eine oszillatorische Änderung des Absorptionsspektrums mit einer Frequenz von 10 THz, was wir der Modulation der interatomaren Abständen durch kohärente Phononen, und die damit einhergehende Modulation der chemischen Umgebung des absorbierenden Atoms, zuschreiben. Harte UV-Spektroskopie, insbesondere bei niedrigen Energien und nahe der Kante (engl.: x-ray absorption near edge spectroscopy (XANES)), ist hoch sensitiv auf die chemische Umgebung des jeweiligen absorbierenden Atoms. Wir verwenden zwei Ansätze um die nuklearen Auslenkungen quantitativ zu bestimmen.

Unsere Resultate erlauben einen faszinierenden, neuen Einblick in die mikroskopische Natur des Raman-Effekts. Sie verbinden einen direkten Nachweis des antreibenden Mechanismus, der induzierten Polarisation, mit einer direkten Beobachtung des Resultats, die oszillatorische Auslenkung der Kerne. Dabei konnten mit harter UV-Spektroskopie

nukleare Auslenkungen in der Größenordnung von 10^{-4} Å mit Subpicosekundenzeitauflösung aufgelöst werden.

Introduction

X-ray and extreme ultraviolet (XUV) absorption spectroscopy allow for an element specific insight into the chemical and structural environment of the element under study. The first x-ray absorption spectrum was measured by de Broglie in 1913 [dB13]. Time resolved x-ray absorption experiments with picosecond resolution became possible with the development of slicing [SCC+00] or short pulse synchrotron [GBS+05, CCF+04, SBA+03] and laser plasma sources [RWJ+96, NGL+99, ARBC+05]. Time resolved X-ray absorption spectroscopy (XAS) experiments were used to study chemical decomposition [RWJ+96], charge transfer in metal ligand compounds [GBS+05, SBA+03], metal-insulator transitions [CCF+04] and, with the onset of femtosecond and attosecond sources, even ultrafast electron dynamics in solids [SRP+14, RLN16, VWJL+13, CMU+07, Sto92]

X-ray and XUV absorption spectroscopy can be split into two regions, which yield distinct information about the material under study. The region close to the onset of absorption, the so called x-ray absorption near edge spectroscopy (XANES), is highly sensitive to the chemical environment of the absorbing atom, especially its oxidation state. Time resolved XANES is therefore uniquely valuable to unambiguously unravel charge transfer processes of specific elements in a compound, such as transition metals in catalysts and biomolecules. The region several hundreds of eV above the edge, the so called Extended X-ray Absorption Fine Structure (EXAFS), delivers structural information about the compound under study. The measured EXAFS spectrum can be directly used to derive the atomic radial distribution function of the absorbing element, which includes nearest neighbor distances. EXAFS is highly sensitive to structural changes in the material and applicable and highly accurate even for liquids and amorphous solids.

This thesis investigates the intricate interplay between light induced electronic polarization and nuclear excitation in the Raman effect. For many materials the macroscopic optical response, i.e. the refractive index, and the Raman spectrum are known. Less explored is the exact, microscopic spatial shape of the induced polarization, along with possible charge transfer processes within the unit cell, and how it relates to the excitation of nuclear vibration. For an x-ray absorption experiment, which studies this interplay, the following conditions should be satisfied:

- The chemical environment of the absorbing element must change due to the Raman excitation. This forbids the use of stationary Raman scattering as it only increases the spatial size of the nuclear wave packet, which affects the x-ray spectrum only in a very subtle and weak manner. Instead impulsive stimulated Raman (see Sec. 1.1 and Fig. 1.3) should be used, as it creates a coherent nuclear wave packet, which is harmonically oscillating in space.

- The unit cell should contain only one symmetry equivalent atom of the element under study. Otherwise the spectra of the inequivalent atoms overlap and the analysis complicates.
- The material must contain a suitable element, which has an absorption edge that lies within the spectrum of the x-ray or XUV source at hand. It should otherwise preferably only contain light elements and the element under study should make up a large fraction of the material.
- The spatial shape of the induced electronic polarization, i.e. the transient electron density, should be known.

Lithium borohydride ($LiBH_4$) fulfills all these conditions and we chose to use it as exemplary material in this thesis.

We use a Ti:sapphire laser system, which delivers 35 fs short pulses at 800 nm wavelength and 30 mJ pulse energy. The Ti:sapphire laser drives an optical parmetric amplifier (OPA) with a mid-IR output at 1.4 µm (signal). Both waves are used in a two-color high-harmonic generation (HHG) setup to generate femtosecond XUV pulses between 20-100 eV. The XUV pulses are used as pump in a pump-probe XUV absorption spectroscopy experiment. For the desired impulsive stimulated Raman excitation a pump with much lower photon energy than lithium borohydride's band gap of ~ 7 eV is needed to exclude direct excitation of electrons into the conduction band via multi photon absorption.

In this thesis we show how the induced electronic polarization of a non-resonant ultra-short pulse excites nuclear vibrations, which are observed in real time through time resolved x-ray absorption spectroscopy. We use the Bethe-Salpeter equation (BSE), a state of the art solid state theory framework for the theoretical prediction of absorption spectra with electron-hole correlation, absolute Raman spectroscopy and a reevaluation of transient x-ray diffraction data, together with transient XUV absorption to draw a complete picture of the Raman effect.

Outline of this work: Chapter 1 presents the basic experimental and theoretical concepts that are used in this thesis, together with a short historical outline of their development. In chapter 2 the necessary theoretical tools are described. After a short general introduction into solid state theory, the theory of x-ray absorption and the Bethe-Salpeter equation (BSE) framework are presented. The theory of stationary and impulsive Raman is developed in the second half of the second chapter. Chapter 3 describes the high-harmonic generation (HHG) and XUV detection setup, the stability of the XUV source and the sample preparation. In chapter 4 I use the results from x-ray absorption, x-ray diffraction and absolute Raman experiments alongside with theoretical absorption spectra from BSE to describe new insights into the Raman effect. The thesis is completed by a conclusion and its German translation in Chapter 5 and 6 respectively.

1 Basic Concepts

1.1 Spontaneous and impulsive Raman Scattering

The Raman effect, named after its discoverer Chandrasekhara Venkata Raman, is an inelastic scattering process, where photons are scattered by matter and thereby transfer energy and momentum into molecular vibrations. Raman spectroscopy, which measures the scattered light and especially its inelastic frequency shift, quickly became widely used after its discovery in 1928 [RK28b, Ram28, RK28a]. Energy can only be exchanged in discrete vibrational quanta, whose energy equals the Planck's constant times the vibrational frequency, which depends on the masses of the vibrating nuclei and binding forces between them. Different molecules show distinctly different Raman spectra, which allows for their analytical discrimination. There are two main differences between Raman scattering and IR absorption spectroscopy. In Raman spectroscopy one can freely choose the wavelength of the initial radiation, which allows to work in the convenient optical range. Secondly the light source can be monochromatic, in contrast to IR spectroscopy, where a broadband source is needed.

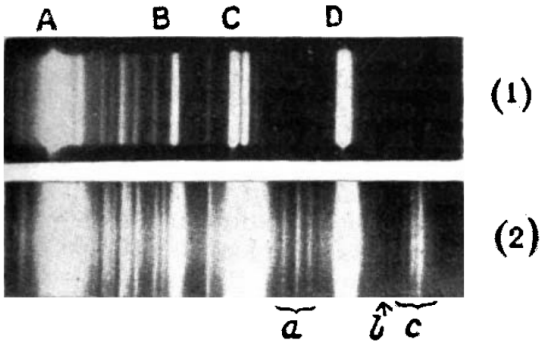

Figure 1.1: Original measurement of Raman and Krishnan published in [RK28b]. (1) shows the spectrum of a quartz mercury lamp , which was used as light source. (2) depicts the scattered spectrum of Toluene, where new lines labeled a, b and c appeared. As described by Raman and Krishnan the position of the lines a,b,c depend on the molecule under study and on the wavelength of the original radiation.

Raman was Professor at the University of Calcutta were he worked on molecular scattering of light. In 1921 he was famously invited to an university congress in Oxford and crossed the Mediterranean sea by ship on his voyage to England. He was intrigued by the deep blue opalescent color of the sea, which Lord Rayleigh [Ray99] attributed to the reflection of the blue color of the sky, which he had explained by Rayleigh scattering. Raman however was not convinced and quenched the reflection with a Nicol prism to discover that in fact the color was not due to the sky's reflection but a property of the water itself. His interest in light scattering of transparent liquids was aroused and after returning to Calcutta he started experimental and theoretical studies on this topic.

In the first experiments Raman and his coworkers used sunlight, which was collected by a retrorefractor, as light source. In 1923 his student Ramanathan first discovered the appearance of a feeble new type of radiation, whose change of depolarization as a function of wavelength could not be explained by existing scattering theories. For the next several years Raman's group tried to investigate this phenomenon in more detail. The results were however inconclusive due to the extremely weak nature of the new scattering phenomenon.

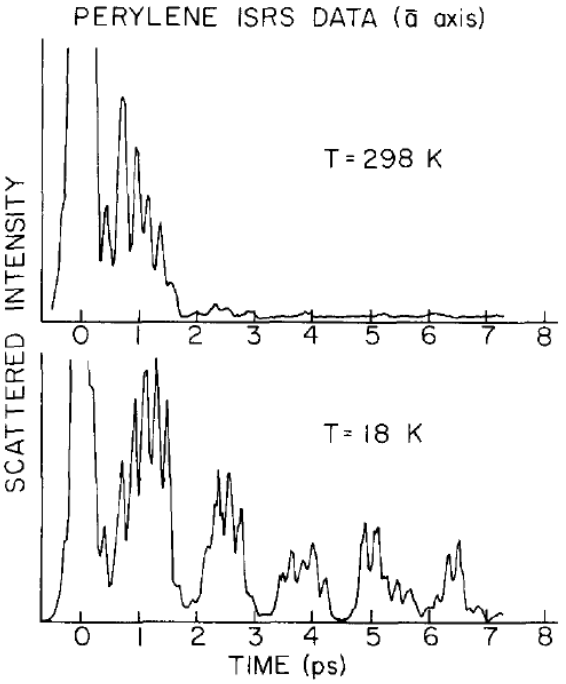

Figure 1.2: Early impulsive stimulated Raman scattering (ISRS) experiment on α-perylene published by de Silvestri et al. [DSFI$^+$85]. The plot shows the intensity of a probe beam that is scattered off an ISRS induced transient grating. The probe intensity oscillates with multiple frequencies, which can directly be related to the different vibrational modes that are oscillating coherently, i.e. we see the effect of actual nuclear displacement.

In 1927 Venkateswaran undertook studies with glycerin and discovered that the scattered light was green instead of the usual blue. This lead them to investigate the phenomenon further by blocking parts of the solar spectrum with optical filters. They discovered that the scattered light was frequency shifted to the red and Raman quickly saw the analogy the previously published Compton effect, i.e. that light could be inelastically scattered off matter. They observed that the new, scattered region in the spectrum became sharper when they used more filters on the solar light. This lead them to change their light source from the sun to a mercury quartz lamp, which delivers sharp emission lines. With the new setup they discovered that the scattered spectrum consists of sharp lines (see Fig. 1.1) and that the frequency shift of these lines depends on the molecule and are equal to the vibrational frequencies of IR absorption measurements. The mercury quartz lamp experiments published in [RK28a] were the first to measure what we today would call a Raman spectrum.

An important theoretical contribution was done by Placzek [Pla34] in 1934. Beforehand the amplitude of Raman spectra could only be calculated by summing over many unoccupied states, which was not feasible even for the simplest of materials at the time. Placzek however connected the amplitudes to the first derivative with respect to the nuclear displacements of the electronic polarizability, the so called Raman tensor. The symmetry properties of the Raman tensor could be derived so that with polarized Raman spectroscopy the symmetry of each vibrational mode could be inferred. On the other hand his derivation highlighted the light-induced change in the electron density, as described by the polarizability, as the driving force behind the excitation of the vibrational modes. This connection shall be the investigated further in this thesis.

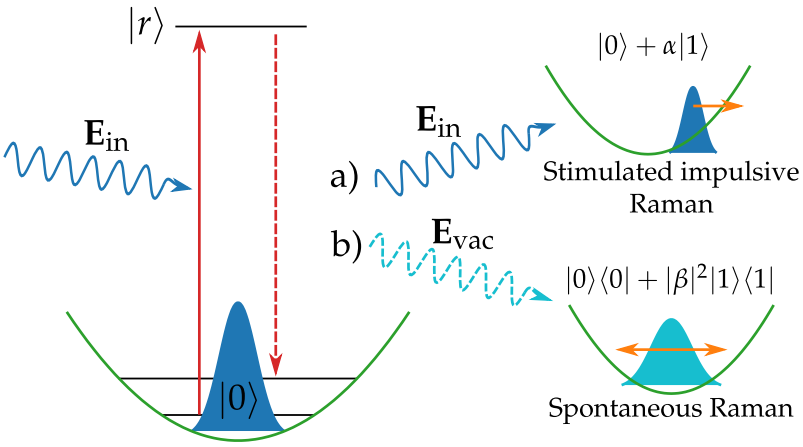

Figure 1.3: Schematic representation of the spontaneous and stimulated impulsive Raman effect. In both processes the nuclear vibrational wave packet is raised to an electronically excited state $|r\rangle$ through dipole interaction with the laser field and immediately deexcited through a) stimulated emission with a mode within the spectrum of the incoming pulse, hence the term impulsive or b) spontaneous emission, i.e. interaction with the vacuum fluctuation field. a) leads to a coherent superposition of the excited states and the ground state and a actual displacement of the nuclear wave packet. b) on the other hand leads to an incoherent superposition, i.e. statistical mixture, of the excited states and the ground state and hence the final state is only broadened in width and still stationary.

In spontaneous Raman spectroscopy incident monochromatic light is shined on a sample and the spontaneously inelastically scattered light is recorded, which gives insight into the Raman active vibrational excitations of the material. Due to the random phase relation between the incident and scattered light the molecular ensemble does not show collective coherent atomic displacement. It should be noted that this type of Raman spectroscopy dominates till this day because of its simplicity and analytical prowess. With the advent of pulsed, ultrashort lasers however new types of Raman spectroscopy became feasible.

Stimulated Raman spectroscopy emerged in the mid 1980s and was applied to various solids and liquids [LFSK78, VTH83, DSFI$^+$85, RWJ$^+$87, CM88, WLWN91, DWN92]. Early studies [LFSK78] observed the quantum beating at the difference frequency $\Delta\omega_{ij} = \omega_i - \omega_j$ between two excited modes i and j. Later studies as e.g. [DSFI$^+$85] observed the oscillation of the various excited modes directly.

There are two techniques for stimulated Raman, which both must ensure that light at the Raman shifted frequency is available for stimulated emission. Either one directly uses two driving frequencies, whose frequency difference is already tuned to a Raman mode of the material under study or one starts with a single frequency with sufficiently high intensity and uses a long interaction volume. The forward scattered Raman radiation that is spontaneously emitted at the beginning of the volume and propagates with the main beam will be amplified by stimulated emission and increase exponentially. Both processes are so effective that they even can be used in a light generation scheme.

The development of sub picosecond pulsed lasers spawned a new member of the Raman spectroscopy family, namely impulsive stimulated Raman scattering (ISRS). Here a very

short optical pulse coherently and impulsively drives vibrational modes of the material. This leads to actual displacements of the nuclei, i.e. non-vanishing expectation values for the position operator, which can be measured by a second ultrashort pulse in the time domain. The vibrational mode and nuclear displacement thus can be seen as an oscillation in the time domain (see Fig. 1.2), whereas a standard Raman spectrum shows frequency domain information. The process is only effective if the driving pulse is shorter than a period of the respective vibrational mode, therefore the term impulsive. In frequency domain this is equivalent to saying, that the Raman shifted frequency must be within the spectral width of the optical pulse.

Spontaneous and impulsive Raman scattering are often described in a perturbative approach (see Fig. 1.3). A dipole interaction with the incident electric field raises the nuclear wave packet into an electronically excited state [1], from which it is deexcited through a) stimulated emission with $\mathbf{E}_{\text{in}}$ or b) spontaneous emission though coupling with the vacuum field for a) stimulated impulsive and b) spontaneous Raman scattering. In both cases the photon energy of the emitted field differs by a vibrational energy quantum $\hbar\omega_{\text{vib}}$ from the initial photon energy. Impulsive stimulated Raman is a coherent process and so its vibrational final state is coherent superposition in this case a so called coherent state, i.e. $|f\rangle = |\alpha\rangle$, which for weak excitation can be approximated as a superposition of first and second vibrational fock state $|\alpha\rangle \approx \frac{|0\rangle+\alpha|1\rangle}{\sqrt{1+|\alpha|^2}}$. A coherent state oscillates harmonically in space.

For spontaneous Raman the deexcitation interaction is spontaneous emission (see b) in Fig. 1.3), which is incoherent in the sense that the final state is a statistical mixture, which in the weak excitation limit can be represented by the density matrix $\rho = \left(1-|\beta|^2\right)|0\rangle\langle 0| + |\beta|^2|1\rangle\langle 1|$.

The harmonic motion of the ISRS final state directly affects the optical properties of the material and thus can be readily mapped by a probe pulse. Spontaneous Raman, on the other hand, only leads to a vibrationally hotter material, which basically does not change its optical properties.

[1] Note that one should distinguish here between Resonance Raman, where the transition energy between the ground state and the excited state $|r\rangle$ is close to the photon energy and the standard non-resonant Raman. In Resonance Raman one can describe the whole process through an excursion of the nuclear wave packet from the ground state potential surface to the electronically excited surface and back [PLM90]. The momentum is then gained through motion in the excited potential surface. This description is not valid in the case of non-resonant Raman scattering.

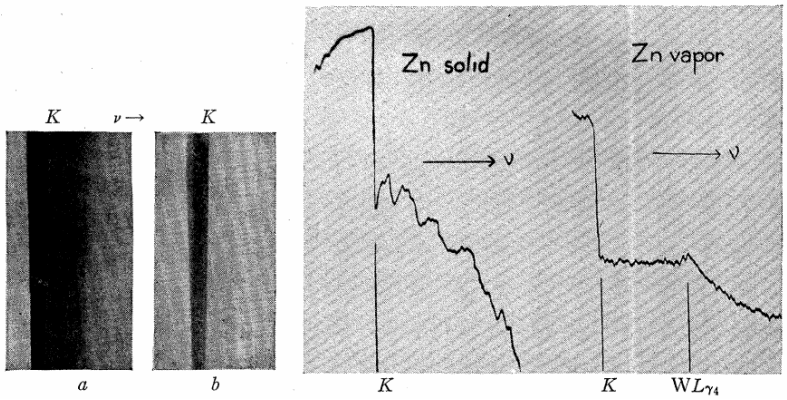

Figure 1.4: X-ray absorption spectra at the K-edge of (a) solid Zinc and (b) Zinc vapor as measured by Hanawalt [Han31]. Solid Zinc shows oscillations next to the absorption edge due to the scattering of the photo electron off neighboring atoms, whereas the vapor does not, due to the lack of neighbors. This is one of the first EXAFS spectra, although it was not fully understood at the time it was measured.

1.2 Extreme Ultraviolet and X-ray Absorption Spectroscopy

The first x-ray absorption spectrum was recorded by de Broglie in 1913 [dB13]. Surprisingly 18 years after the discovery of x-rays by Röntgen. He used a single crystal under Bragg condition as dispersive element, i.e. a Bragg monochromator, and recorded the spectrum on a photographic plate. He did not use a sample but recorded the K-edge of Bromine and silver from the photographic emulsion. He noted a steep onset of absorption at material specific energies followed by generally decreasing absorption with higher photon energy. Shortly thereafter the energies were understood to be proportional to the atomic number squared. A feature that helped to establish the atomic number in the periodic system as an important quantity in addition to the atomic mass.

The first observation of the importance of the chemical environment in X-ray absorption spectroscopy (XAS) was performed by Hanawalt [Han31], who studied the x-ray absorption spectrum of various compounds in gaseous and solid phase. He noted significant changes in the spectrum between gaseous and solid phase. For gaseous zinc, which forms a mono atomic vapor, he found the complete disappearance of fine structures above the absorption edge (see Fig. 1.4) in comparison with the solid phase. At that time experimenters mostly noted the position and relative strength of peaks in the absorption spectrum but were unable to extract physical properties of the system due to the lack of quantitative theory.

In the 1960s the appearance of more brilliant x-ray sources and improved monochromators allowed for more systematic studies of x-ray absorption spectra. Van Nordsthand performed such a systematic review [Nor60] and found a dependence of the position and shape of the spectrum and especially onset of the absorption on the chemical environment of the absorbing atom. He noted the dependence on the oxidation state, the so called chemical shift. In his studies van Nordsthand used XAS to analyze catalytically active compounds, in his case containing transition metals.

Transition metals can occur in different oxidation states in different compounds and during catalysis, which make them an appealing target for XAS studies. Catalysis is an important field for XAS until this day because catalysis typically happens in the liquid phase or at a surface where XAS is applicable and other methods such as x-ray diffraction do not excel and secondly catalytic compounds often have specific active atoms, often transition metals, which can be observed exclusively by XAS.

Van Nordsthand [Nor60] extracted information from the region close to the absorption edge, nowadays called x-ray absorption near edge spectroscopy (XANES) and established its link to chemical properties around the absorber. In 1969 and 1971 Sayers, Stern and Lytle published two papers [SLS69, SSL71] that established a link between structural information and the oscillating part of the spectrum several 100 eV above the edge, the so called Extendend x-ray absorption fine structure (EXAFS).

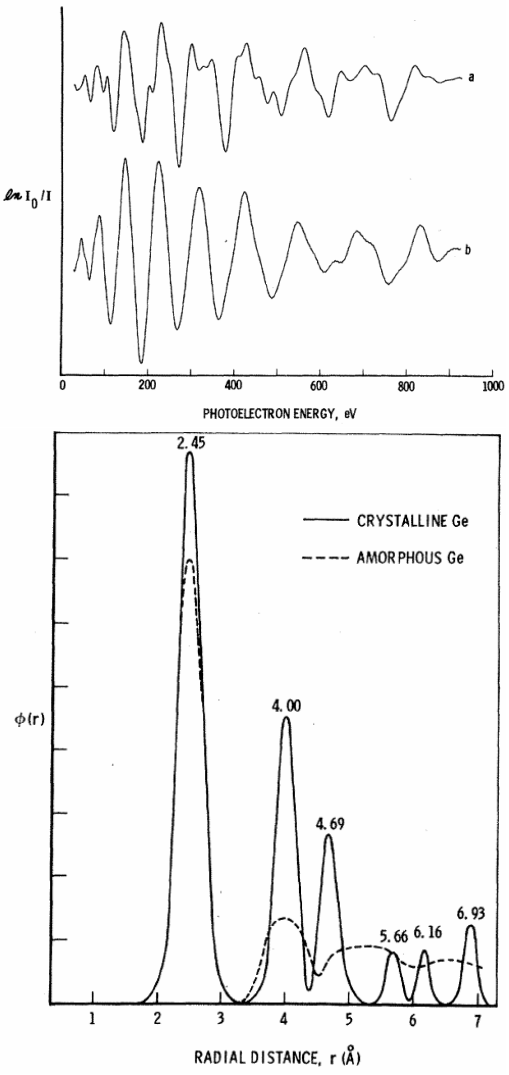

Figure 1.5: Top panel: Oscillating part of the experimental absorption spectrum of crystalline (top) and amorphous (bottom) germanium as published in [SSL71]. Bottom panel: Radial distribution function of crystalline and amorphous germanium, which was retrieved from the data shown in the top panel. Both phases show a distinct peak at 2.45 Å, which represents the bond length of germanium. The crystalline phase shows several more distinct peaks, whereas for the amorphous phase the distribution function becomes more and more blurred, which shows long range order for crystalline germanium and lack thereof for the amorphous phase.

In 1969 they developed a point scattering formula [SLS69], which for the first time, yielded good quantitative agreement for the EXAFS spectrum. In 1971 [SSL71] they showed that their point scattering formula for EXAFS can be formally inverted and yields the radial distribution function of the atomic density. They applied their finding on the experimentally acquired spectra of crystalline and amorphous germanium and could retain the germanium bonding distance within 1% accuracy and could directly retrieve the amorphous or crystalline character from the radial distribution function (see Fig. 1.5). Nowadays stationary or quasi-stationary EXAFS is a standard technique [Sto92] for the characterization of amorphous and disordered matter.

In the 1990s new sources were developed, that allow for the generation of picosecond and femtosecond pulses. Synchrotrons were equipped with the so called slicing scheme. Here

a long ~ 100 ps electron bunch copropagetes and interacts with an optical or near infrared pulse, which modifies the electron bunch's momentum distribution. With a bending magnet the modified electrons can be separated and used to generate sub-picosecond x-ray pulses in an undulator or wiggler. The flux of a slicing scheme is rather low because only a very small fraction, to be precise the ratio of laser pulse duration and initial electron bunch duration, is used to actually generate radiation. The temporal resolution of such scheme is in most experiments in the low picosecond regime but down to 200 fs are possible [BJS+07, SLR+15]. The first femtosecond x-ray absorption study was performed in 2009 by Bressler et. al. [BMP+09].

Laser generated plasma sources produce x-ray radiation by focusing an ultrashort laser onto a solid or liquid, typically metallic target. The high intensity of the laser turn part of the target into a hot plasma, which emits characteristic lines as well as a broad continuum, which both can be used for XAS.

Raksi et. al. [RWJ+96] showed in 1996 the feasibility of picosecond time resolved X-ray absorption spectroscopy (TRXAS) with a plasma source with an experiment on the sulfur K-edge of sulfur hexafluoride (SF_6) in the gas phase. They observed a strong decrease of the main absorption peak upon photo dissociation of the molecule. Their temporal resolution was however insufficient to resolve dissociation dynamics.

Chergui and coworkers performed experiments on Ruthenium tris-bipyridine [GBS+05] in 2005 and were able to show that its long lived excited state exhibits a Ruthenium atom with +3 oxidation state (Ru^{III}), while its ground state exhibits a Ruthenium with +2 oxidation state (Ru^{II}). They concluded that the absorption process must include a metal to ligand charge transfer (MLCT). Chergui and coworkers used the ALS beam line with a special electron bunch mode, which was electronically synchronized with a Ti:Sapphire laser. They reached a temporal resolution of ~ 80 ps, which was limited by the x-ray pulse duration. The measured excited state spectrum showed a blue shift of the $2p_{3/2} \rightarrow 4d_{3/2}$ main feature and the appearance of a new $2p_{3/2} \rightarrow 4d_{5/2}$ peak, both indicating a +3 oxidation state Ruthenium in the excited state. This study shows the great potential of TRXAS in obtaining the electronic structure of excited states.

Since the 2000s the development in high-harmonic generation (HHG) table top sources and free electron lasers has spawned new interest in the field of x-ray absorption spectroscopy. Especially the low femtosecond to attosecond temporal resolution of HHG sources and their relatively high brilliance opens new possibilities in the field of electronic structure and dynamics research. In 2013 Vura-Weis and coworkers [VWJL+13] performed a study about the excited state coordination chemistry of hematite iron oxide (α-Fe_2O_3) using a HHG source. They observed a red shift of the $M_{2,3}$ Fe edge upon photo excitation with 400 nm, indicating a metal to ligand charge transfer (MLCT) from Fe^{3+} to Fe^{2+}. The MLCT excited state decays with 240 fs decay time into a long lived trap state, whose nature is still under debate. This study however clearly shows the ability of TRXAS to reveal the nature of short lived intermediate excited states. Other studies [CMU+07, FFH+05, TCS+16] have exploited the attosecond time resolution that is possible with HHG to directly observe ultrafast electron dynamics. In [SRP+14] Schultze and coworkers observed sub-fs electron

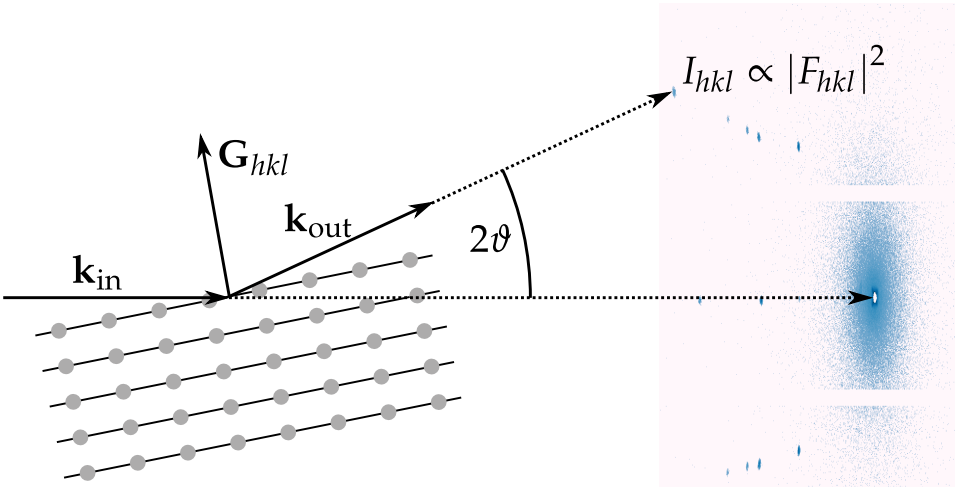

Figure 1.6: Schematic of x-ray diffraction from a single crystal. A (plane) wave with wave vector $\mathbf{k}_{in}$ is scattered by the electrons in the crystal. If constructive interference between a certain set of planes with Miller index hkl is achieved, light is effectively scattered by the crystal and measured as a spot on the detector. The image on the right is measured with the rotating crystal method. Here the crystal is rotated so that various different planes are under Bragg condition, while the detector is recording.

dynamics in Silicon with TRXAS at the Si $L_{2,3}$ edge upon photo excitation with a few femtosecond near infrared pulse. Pertot et. al. [PSM+17] explored TRXAS in the water window at the carbon K-edge. They observed a light induced ionization in CF_4 with subsequent dissociation dynamics from CF_4^+ to CF_3^+. They observe the appearance of several new bands due to the lower symmetry of firstly CF_4^+ due to the Jahn-Teller effect, which leads to a spontaneous symmetry breaking of the T_d symmetry of CF_4, and secondly due to the planar D_{3h} symmetry of CF_3^+.

1.3 Time resolved x-ray diffraction and transient electron densities

X-ray diffraction is one of the, if not the, most powerful and widely used experimental technique to uncover the microscopic structure of matter. The first x-ray diffraction image was recorded in 1912 by Friedrich, Knipping und Laue [FKL13]. Laue considered crystals as 3D gratings, which lead him to perform the diffraction experiment but complicated his analysis. In 1913, based on Laue's initial measurement, W.L. Bragg presented the idea that x-ray diffraction could be explained through interference between simple planes within the materials [Bra13a], which greatly simplified the analysis, and allowed him to derive the famous Bragg law

$$n\lambda = 2d \sin\vartheta,$$

and uncover, together with his father W.H. Bragg, the microscopic structure of various fundamental materials, such as diamond and rock salt [Bra13b, BB13]. Bragg spawned the idea that the intensities of the different diffraction peaks encode the electron density, which

can be recovered with a Fourier series [Bra15]. This idea was put into practice in 1925 in a series of papers by Duane and Havighurst [Dua25, Hav25, Hav27]. It took another forty years until real high quality electron densities could be recovered [Daw67] and x-ray crystallography was established as the highly accurate and reliable method, which it is today.

After this short historical introduction let us now see how the structural information of a material can be extracted from x-ray diffraction data. Fig. 1.6 depicts a single crystal experiment with monochromatic incoming light with wave vector $\mathbf{k}_{in}$. If the single crystal is aligned so that there is constructive interference between a certain set of planes, often labeled with the Miller index hkl, light will be scattered effectively with wave vector $\mathbf{k}_{out}$. The scattered light appears as a spot on the detector. The condition for constructive interference can be expressed with the Laue law

$$\mathbf{G}_{hkl} = \mathbf{k}_{out} - \mathbf{k}_{in}$$

with the reciprocal lattice basis vectors $\mathbf{b}_i$ and the reciprocal lattice vector $\mathbf{G}_{hkl}$ of plane hkl according to

$$\mathbf{G}_{hkl} = h\mathbf{b}_1 + k\mathbf{b}_2 + l\mathbf{b}_3$$

The Laue law includes the Bragg law but is often preferred as it yields both scattering angles ϕ_{hkl} and ϑ_{hkl}, whereas the Bragg law only describes the latter. Typically the crystal is rotated in a single crystal experiment to collect multiple spots from different planes hkl. In other words it is necessary to collect the intensities and diffraction angles for as many hkl as possible. The intensities and electron density are related by

$$\begin{aligned} F_{hkl} &= \frac{1}{V_{uc}} \int_{V_{uc}} \rho(\mathbf{r}) e^{-i\mathbf{G}_{hkl}\cdot\mathbf{r}} \, d^3r \\ \rho(\mathbf{r}) &= \sum_{hkl} F_{hkl} \, e^{i\mathbf{G}_{hkl}\cdot\mathbf{r}} \\ I_{hkl} &\propto |F_{hkl}|^2 \end{aligned}$$

The measured intensities are proportional to the modulus square of the Fourier amplitudes of the electron density. The electron density can recovered with high precision from the measured intensities, i.e. $|F_{hkl}|^2$, although the phase of the complex quantity F_{hkl} is not measured [2].

The information in the x-ray diffraction data is nicely separated (see Fig. 1.7). From the diffraction angles $\vartheta_{hkl}, \phi_{hkl}$ (together with the crystal rotation) one can deduce the lattice of the system, i.e. the lattice constants and the lattice system or the lattice vectors. From the lack of certain reflexes hkl, so called forbidden reflexes, one can deduce the space group

[2] This is the so called phase problem for which there is no trivial solution. Typically various constraints to the electron density are applied, e.g. that it is positive and that it consists of well defined, distinct peaks from the core atoms. Then recovering the electron density is solved as an iterative, inverse problem.

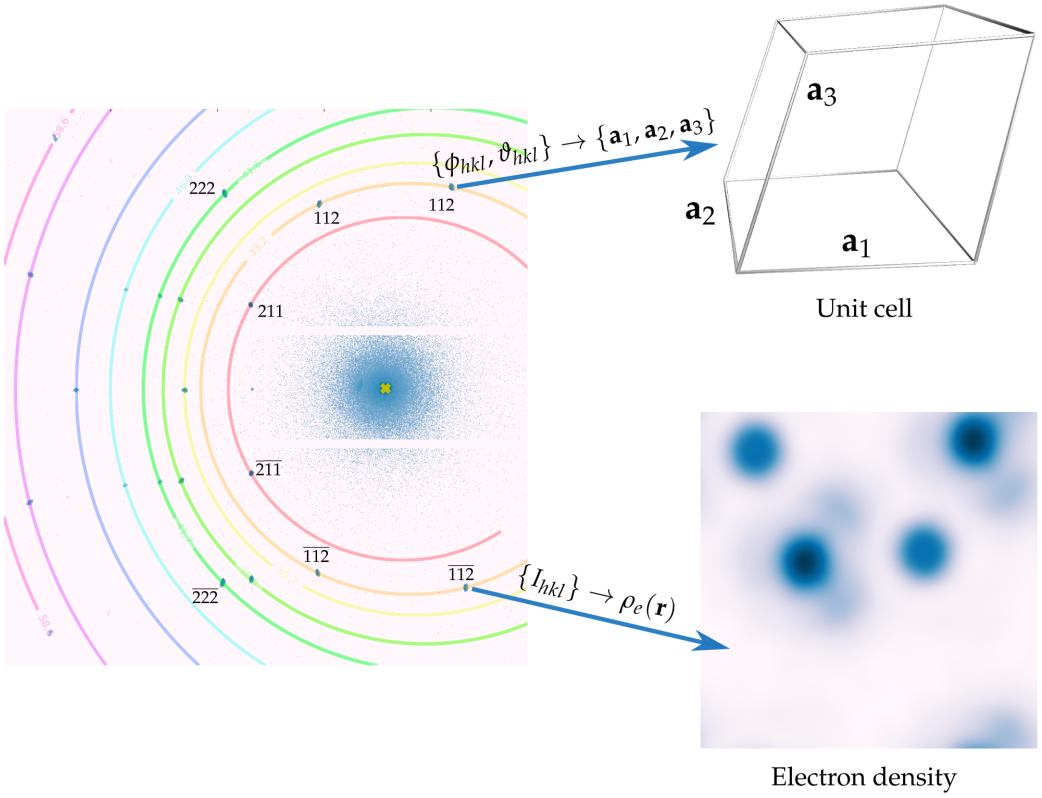

Figure 1.7: Data extraction from a x-ray diffraction recording. From x-ray diffraction images (see one exemplary image recorded with the rotating crystal method on the left), the lattice, i.e. unit cell (right top), and the electron density (right bottom) can be extracted. The image on the left shows various reflexes, which are labeled with their Miller index. The ellipses are equipotential surfaces of the azimuthal scattering angle.

of the material, i.e. the internal symmetry of the unit cell. From the measured intensities I_{hkl} of the reflexes one can deduce the actual electron density of the material.

The first time resolved x-ray diffraction experiments with sub-picosecond temporal resolution were performed in the mid 1990s [SLC+96, RRU+97]. Time resolved x-ray diffraction is a quite straightforward extension of its static variant. The x-ray scattering can be viewed as an instantaneous interaction and the time-dependent scattering intensities $I_{hkl}(t)$ can be measured through a pump probe experiment. In time resolved experiments, due to the increased complexity and low flux of pulsed sources, typically only a very small set of reflexes hkl are measured [3], which would be insufficient to reconstruct the electron density from scratch. The reconstruction of the transient electron density $\rho(\mathbf{r}, t)$ is build upon the static reconstruction. The change in the structure factor $\Delta F_{hkl}(t)$ is used as a small perturbation for the known static structure factors, which alleviates the phase problem as the static phases are known and overcomes the problem of the small set of recorded reflexes. A majority of time resolved x-ray diffraction studies concentrated on changes of the unit cell, i.e. the lattice constants, through phonons [BZG+04, CSB+00, RPJG+99], phase transitions [CTS+01] or non-thermal melting [SCST+99]. Changes of the unit cell

[3] Typically in the order of ten reflexes are measured in time resolved studies, whereas for static diffraction ten thousands of reflexes need to be measured for a high quality electron density reconstruction

are much easier to detect and reconstruct than changes of the electron density alone, as they affect the scattering angle of x-ray diffraction, which spatially moves the spots on the detector.

Stingl et. al. [SZF+12] measured the transient electron density upon non-resonant excitation for the prototype ionic material lithium borohydride ($LiBH_4$). Their reconstructed transient electron density is used in this thesis. Stingl et. al. used powder diffraction and recorded 16 allowed and 8 forbidden reflexes. Three of them with strongest intensity changes are shown in Fig. 1.8.

They observed a fully reversible, instantaneous charge transfer from the BH_4 anion to the lithium cation, which was visible in the transient electron density. This charge transfer is responsible for the refractive index, i.e. a larger polarizability, as one would expect from the molecular polarizability of the BH_4 tetrahedron within the Clausius–Mossotti relation alone.

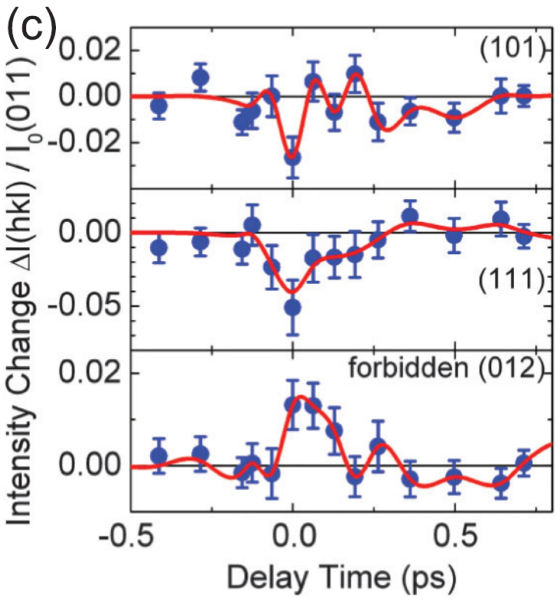

Figure 1.8: Transient intensity change $^{\Delta I_{hkl}(t)}/_{I_{011}}$ upon non-resonant excitation in lithium borohydride as measured by Stingl et. al [SZF+12].

Many important quantities can be derived from the (transient) electron density once it is known. In this thesis we focus on the interaction between the light-induced polarization and nuclear excitation. The (transient) Coulomb potential can be directly calculated with the (transient) electron density with the Poisson equation (see Sec. 2.4.1). The additional Coulomb forces onto the nuclei are zero in the static case, as the crystal lattice is in the ground state, and become non-zero in the transient case, which causes nuclear motions.

2 Theoretical Background

2.1 Extreme Ultraviolet (XUV) and X-ray Absorption Spectroscopy

X-ray absorption spectroscopy (XAS) is a powerful tool to probe structural and chemical properties of solids, liquids and gases. XAS is inherently element specific as absorption edges occur close to the atomic transition energies, which are only slightly, $\pm 10\,\mathrm{eV}$, shifted by the chemical environment. For example the atomic Li 1s binding energy is 55 eV and Li K-edges occur at 55 eV (neutral Li) to 63 eV (Li^+ ion). X-ray absorption spectra are typical split into two regions (see Fig. 2.1). XANES is the region around the edge, which is highly sensitive to the chemical properties around the absorbing site. Here the final states are bound electron hole pair states, which complicates the theoretical calculations. EXAFS is the region several tens of eV above the edge. Here the final state are free photo electron states. EXAFS allows for a relatively simples analysis of the structure around the respective site as the photo electron is diffracted off neighboring atoms, which leads to oscillations in the absorption spectrum, due to interference, between the outgoing and scattered electron wave. A Fourier transform can be directly transformed into a radial distribution function of remarkable ($\sim 1\%$ nearest neighbor distance) accuracy with a simple Fourier transform[1]. In other words the wavelength of the oscillations are the nearest neighbor distances. In the following section we will focus on XANES. If a plane wave electric field travels inside a material the electric field is given by

$$\mathbf{E}(\mathbf{r},\omega) = \mathbf{E}_0(\omega)\exp(i\mathbf{k}\cdot\mathbf{r})$$

with the dispersion relation

$$\mathbf{k}^2 = \frac{\omega^2}{c^2}n^2(\omega)$$

The corresponding intensity reads

$$\begin{aligned} I(\mathbf{r},\omega) &= I_0(\omega)\exp\left(-\frac{2\omega\kappa(\omega)}{c}d\right) \\ &= I_0(\omega)\exp(-\alpha(\omega)d) \end{aligned} \tag{2.1}$$

where d is the optical path length in the medium and $\alpha(\omega) = \frac{2\omega\kappa(\omega)}{c}$ the linear attenuation coefficient. Eq. (2.1) is the famous Lambert-Beer law, which describes linear absorption of

[1] To be precise the contribution of the edge and the ω^{-2} tail should first be subtracted and the dependence on the photon energy $\varepsilon_2(E_{ph})$ must be replaced with the k-vector of an electron wave via $E_{ph} = E_{gap} + \frac{\hbar^2k^2}{2m_e}$, which yields $\varepsilon_2(k)$

light in a medium. We want to connect the refractive index n with the dielectric function

$$\sqrt{\varepsilon_r} = \sqrt{\varepsilon_1 + i\varepsilon_2} = n_0 + i\kappa$$

Simple algebra yields

$$\varepsilon_1 = n^2 - \kappa^2 \qquad \varepsilon_2 = 2n\kappa$$

or the inverse relation

$$n = \sqrt{\frac{1}{2}\left(\varepsilon_1 + \sqrt{\varepsilon_1^2 + \varepsilon_2^2}\right)} \qquad \kappa = \sqrt{\frac{1}{2}\left(\sqrt{\varepsilon_1^2 + \varepsilon_2^2} - \varepsilon_1\right)}$$

In the x-ray region both real and imaginary part of the susceptibility are typically small, which means $\varepsilon_1 \approx 1$, $\varepsilon_2 \ll 1$. Then one can approximate

$$\kappa \approx \frac{\varepsilon_2}{2\sqrt{\varepsilon_1}} \approx \frac{\varepsilon_2}{2}$$
$$n \approx \sqrt{\varepsilon_1 + \frac{\varepsilon_2^2}{4\varepsilon_1}} \approx \sqrt{\varepsilon_1} + \frac{\varepsilon_2^2}{8\varepsilon_1^{\frac{3}{2}}} \approx 1$$

ε_1 and ε_2 are related by the Kramers-Kronig relations. For the next paragraph we will follow section 2 from [GJ14] and section 4.3 from [BL16]. The interaction Hamiltonian between light and matter can be written via minimal coupling including spin as

$$H_{\text{int}} = \frac{e}{m}\mathbf{p}\cdot\mathbf{A} + \frac{e^2}{2m}\mathbf{A}^2 + \frac{e}{m}\mathbf{s}\cdot\mathbf{B}$$

The spin interaction with the magnetic field was added and coulomb gauge ($\nabla\mathbf{A} = 0$) was used. $\mathbf{A}$ and $\mathbf{B}$ can either be the vector potential and magnetic field operator for quantized light or the vector potential and magnetic field for classical light. The $\mathbf{A}^2$ can be neglected here. Fermi's Golden Rule yields the imaginary refractive index $\kappa(\omega)$ as

$$\kappa(\omega) = \frac{\pi e^2}{2\omega^2 m^2 \varepsilon_0 V_{\text{uc}}} \left|\left\langle f\middle|\hat{O}\middle|i\right\rangle\right|^2 \delta(E_f - E_i - \hbar\omega)$$
$$\hat{O} = \left(\mathbf{e}_{\text{pol}}\cdot\hat{\mathbf{p}} + i\hat{\mathbf{s}}\cdot\left(\mathbf{k}\times\mathbf{e}_{\text{pol}}\right)\right)e^{i\mathbf{k}\cdot\mathbf{r}}.$$

At this point the momentum operator is typically replaced by $\mathbf{p} = \frac{im}{\hbar}\left[\hat{H}, \mathbf{r}\right]$ and a Taylor expansion of the plane wave term $e^{i\mathbf{kr}}$ is used. This leads to a multi-pole expansion of the matrix element, which reads

$$\kappa = \frac{\pi e^2}{2\varepsilon_0 V_{\text{uc}}} |\langle f|\hat{o}|i\rangle|^2 \delta(E_f - E_i - \hbar\omega)$$

with $\hat{o}$ being the multi-pole expanded interaction operator

$$\hat{o} = \hat{o}_{E_1} + \hat{o}_{E_2} + \hat{o}_{E_3} + \hat{o}_{M_1} + \cdots$$
$$\hat{o}_{E_1} = \mathbf{e}_{\text{pol}}\cdot\mathbf{r}$$
$$\hat{o}_{E_2} = \frac{i}{2}\left(\mathbf{e}_{\text{pol}}\cdot\mathbf{r}\right)\left(\mathbf{k}\cdot\mathbf{r}\right)$$
$$\hat{o}_{E_3} = -\frac{1}{6}\left(\mathbf{e}_{\text{pol}}\cdot\mathbf{r}\right)\left(\mathbf{k}\cdot\mathbf{r}\right)^2$$
$$\hat{o}_{M_1} = \frac{\hbar}{2m}(E_f - E_i)\left(\mathbf{k}\times\mathbf{e}_{\text{pol}}\right)\left(\mathbf{L} + 2\mathbf{s}\right)$$

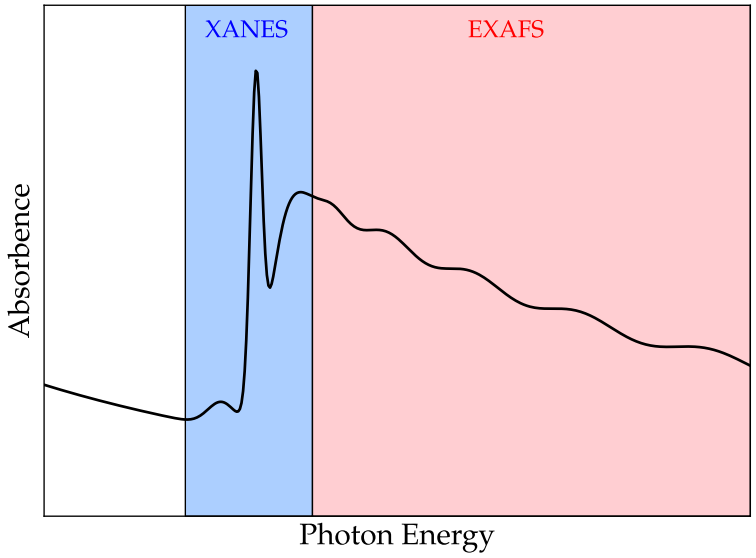

Figure 2.1: Sketch of an x-ray absorption spectrum. The blue region is called x-ray absorption near edge spectroscopy (XANES) and is dominated by a strong excitonic peak. The XANES region is related to chemical properties at the absorbing site of the material and can be used to e.g. determine the oxidation state of the elements under study. Different oxidation states typically have different exciton binding energies due to screening, which leads to a considerable shift of the exciton peak. Before the main peak a small pre-edge feature is visible, which is often a dipole forbidden quadrupole transition. The red region is called Extendend x-ray absorption fine structure (EXAFS) region, which typically shows oscillations due to diffraction of the excited photo electrons off neighboring atoms.

$\hat{o}_{E_1}$, $\hat{o}_{E_2}$ and $\hat{o}_{E_3}$ are the electric dipole quadrupole and octopole operator respectively and $\hat{o}_{M_1}$ the magnetic dipole operator. For XAS the dipole operator always dominates the spectrum and all other operators add only small contributions and can often be neglected. The quadrupole term comes into play at several keV photon energy due to the increase of the k-vector especially if dipole forbidden transitions are possible below the edge, which gives rise to the so called pre-edge features. These are often of great interest as they are highly sensitive to the symmetry around the absorbing elements and allow for detection of changes in the symmetry. The selection rules for the change in angular momentum Δl and change in spin Δs are

$$E_1\text{: } \Delta l = \pm 1$$

$$E_2\text{: } \Delta l = 0, \pm 2$$

$$E_3\text{: } \Delta l = \pm 1, \pm 3$$

$$M_1\text{: } \Delta l = 0, \Delta s = 0, \pm 1$$

From these rules we see that within the dipole approximation K, L_1 and M_1 edges, where the initial state is of s character ($l = 0$), probe p-states. L_{23} and M_{23} edges on the other hand probe s and d states.

The initial state $|i\rangle$ is typically the ground state of the system $|0\rangle$ and is relatively easy to

calculate within an effective one-particle theory such as density functional theory (DFT) or GW. The sum over the final states is however extremely difficult to perform. A suitable subset of all excited states that contribute significantly must be recognized, e.g. one, two or more particle excited states. The other difficulty is that excited states are significantly harder to calculate than ground states. The simplest approximation is to assume that the final state is equal to the ground state, except that one electron advanced from a valence or core state $|v\mathbf{k}\rangle$ to an conduction band state $|c\mathbf{k}\rangle$[2] . This implies that the material does not adapt at all to the excitation and we end up with a pure one particle excitation. The imaginary part of the dielectric tensor can then be expressed as

$$\varepsilon_2(\omega)_{ij} = \frac{e^2}{\varepsilon_0 V_{uc}} \sum_{cv\mathbf{k}} \langle c\mathbf{k}|\hat{r}_i|v\mathbf{k}\rangle\langle v\mathbf{k}|\hat{r}_j|c\mathbf{k}\rangle\delta(\varepsilon_{c\mathbf{k}} - \varepsilon_{v\mathbf{k}} - \omega) \tag{2.2}$$

Within this approximation the knowledge of the one-particle band structure, i.e. energies and transition matrix elements, suffice to calculate the dielectric function and x-ray absorption spectrum (see Fig. 2.2). This is however often a very poor approximation because typical solids adapt quite strongly to excitations and two particle excitations, especially excitons, play a major role and strongly distort the spectrum. In the next section we will describe the BSE method that allows for the inclusion of many body effects and gives a much better accuracy.

2.2 Bethe-Salpeter Equation

Historically full ab initio calculations of optical, UV and x-ray absorption spectra have remained difficult due to the various couplings and effects that are possible in an optical excitation of a solid. For UV and x-ray spectra of insulators and semiconductors, excitonic effects play a major role and greatly affect the absorption spectrum. An exciton is a bound electron-hole pair, that is formed between an electron, which is excited to the conduction band, with the hole it left behind. By definition this is a two-particle effect and goes beyond typical one-electron theories such as DFT or GW. Excitons that span multiple unit cells and display a binding energy of in the order tens of meV or less are referred to as Wannier excitons. Wannier excitons are not bound and display a center of mass kinetic energy. Wannier excitons are typical for excitations between valence and conduction band in materials with a high dielectric constant such as semiconductors. Frenkel excitons on the other hand are localized within one unit cell with a binding energy of typically several hundreds of meV. Frenkel excitons are typical for materials with a low dielectric constant such as insulators and (organic) molecular crystals. Excitons from an excitation between core and conduction band state are typically Frenkel excitons due to the highly localized core state and low screening of highly localized charges. The most simple description of an

[2] In principle the k vectors of conduction and valence state can be different and a sum over all $\mathbf{k}$ and $\mathbf{k}'$ has to be performed. The dipole operator however only allows transitions with $\Delta\mathbf{k} = 0$ so one sum can be omitted

[3] The optical gap is the onset of electronic absorption whereas the direct band gap is the smallest difference between some valence and conduction state of the same k vector

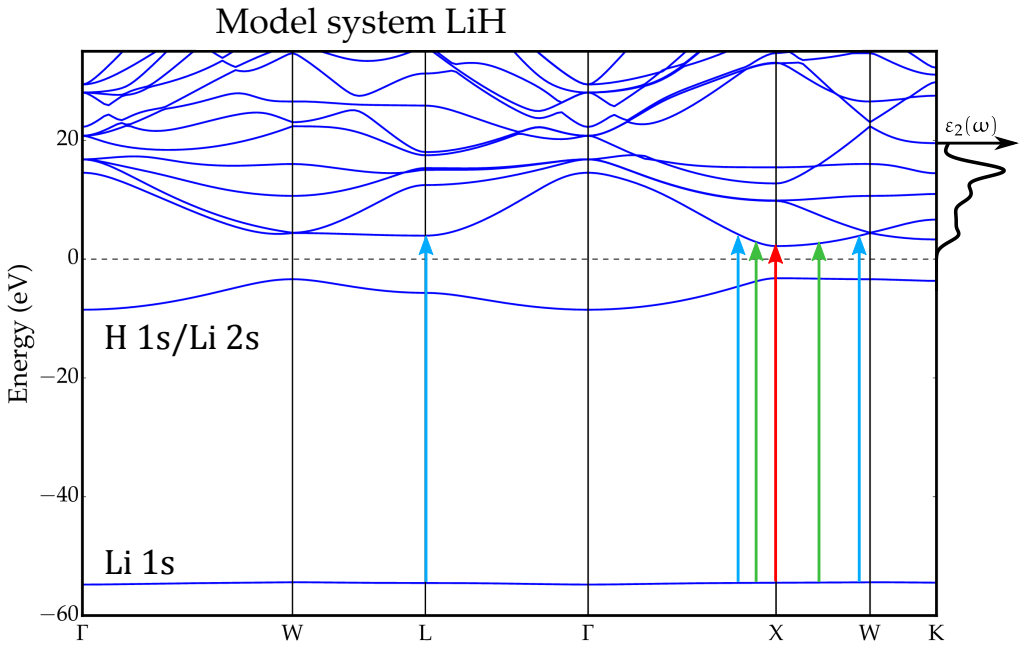

Figure 2.2: Graphical depiction of Eq. (2.2) with the lithium hydride (LiH) K-edge as an example. The absorption spectrum is a sum over all dipole allowed transitions that are vertical in the band structure, i.e. do not change the k-vector, weighted with the respective dipole transition matrix element. As a consequence the optical gap is equal to the direct band gap [3]within this approximation

exciton in a solid is as an Hydrogen atom like system with a screened Coulomb interaction, where the screening is caused by the other electrons of the system. The approximate Hamiltonian is

$$H_{e-h} = -\frac{\hbar^2}{2m_e}\Delta_e - \frac{\hbar^2}{2m_h}\Delta_h - \frac{e^2}{4\pi\varepsilon_0\varepsilon_r|\mathbf{r}_e - \mathbf{r}_h|}$$

with the well known eigenvalues

$$E_n = -13.6\,\mathrm{eV}\cdot\frac{\mu}{\varepsilon_r^2 n^2 m_e} \qquad\qquad \mu = \frac{m_e m_h}{m_e + m_h}$$

For a typical semiconductor ε_r is in the order of 10 and the reduced mass μ, where m_e and m_h are the effective electron and hole masses respectively, is in the order of 0.1, which means an exciton binding energy in the order of 10 meV, i.e. a Wannier exciton. This is a relatively small correction to the optical band gap in terms of energy. Even in this level of sophistication dielectric function around the band gap is strongly changed (see Eq. 10.105 in [HKK94], the so called Elliott formula for Wannier excitons as depicted in Fig. 2.3).

This approach however yields unsatisfactory results for most cases as it neglects several important many-body aspects. First the k-dependence of $\varepsilon_r(k)$ was neglected, i.e. $\varepsilon_r(\mathbf{r}-\mathbf{r}')$ was assumed to be purely local. However the finite screening length scale of a system is important, especially for core holes, that are very localized. The other unsatisfactory approximation is that the Hilbert space of the system is assumed to be the vacuum Hilbert space, which means that the interaction of the exciton with the other (quasi-) electrons is neglected.

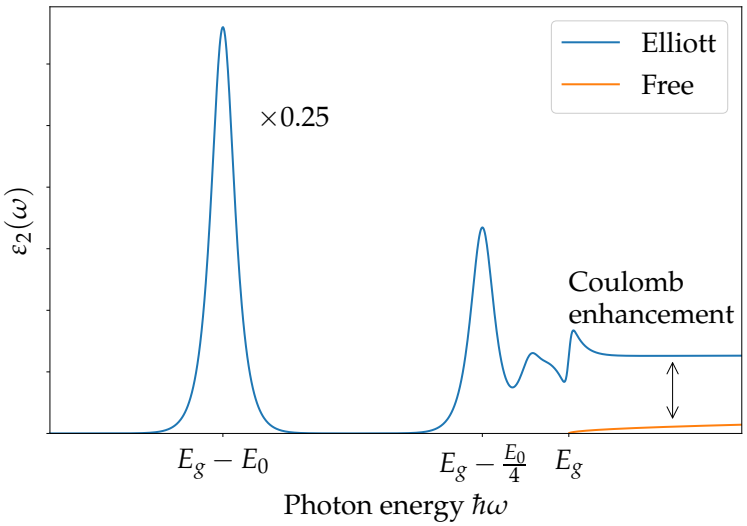

Figure 2.3: Dielectric function of a semiconductor with excitonic effects, calculated with the Elliott formula (Eq. 10.105 in [HKK94]) in comparison to the dielectric function without excitonic effects (labeled Free). For both cases a parabolic valence and conduction band was assumed. Without excitonic effect the dielectric function is zero below the gap and approximately a square root function after the gap, i.e. it increases gradually after the gap. With coulomb attraction between the electron and hole, i.e. excitonic effects, the situation changes drastically. The dielectric function exhibits several exciton peaks below the band gap with the typical $1/n^2$ energy spacing. At the band gap the dielectric function does not gradually increase but is basically constant at a high value, compared to the free electron gas case, after the gap, an effect that is called coulomb enhancement.

One approach to overcome these problems is the Bethe-Salpeter equation (BSE). It was first derived in 1951 by Hans Bethe and Edwin Salpeter [SB51] for relativistic, bound fermions, governed by the Dirac equation. The BSE approach uses the two-particle Green's function similar to the GW approach, which uses the one particle Green's function. The one-particle Green's function yields the in principle correct one-particle excitation spectrum, while the two-particle Green's function yields the correct two-particle spectrum, i.e. excitations involving two particles such as excitons. we will follow a description of BSE [OTPAD09], which uses wave functions and Hamiltonians rather than Green's function. Both descriptions are however equivalent.

The wave function of BSE is a two particle function of electron $\mathbf{r}_e$ and hole $\mathbf{r}_h$ coordinate, which can be expanded into suitable solutions of a one-particle theory $\psi_{v\mathbf{k}}$ and $\psi_{c\mathbf{k}}$ as following

$$\phi^\lambda(\mathbf{r}_e, \mathbf{r}_h) = \sum_{cv\mathbf{k}} A^\lambda_{vc\mathbf{k}} \psi^*_{vk}(\mathbf{r}_h)\psi_{ck}(\mathbf{r}_e) \tag{2.3}$$

Here c and v run over the conduction and valence bands respectively. The wave vector $\mathbf{k}$ is summed over the first Brillouin zone. $A^\lambda_{vc\mathbf{k}}$ is the expansion coefficient of eigenstate λ. Suitable choice of which valence and conduction bands are summed over determines, which types of excitons can be described by this wave function. For optical excitons we

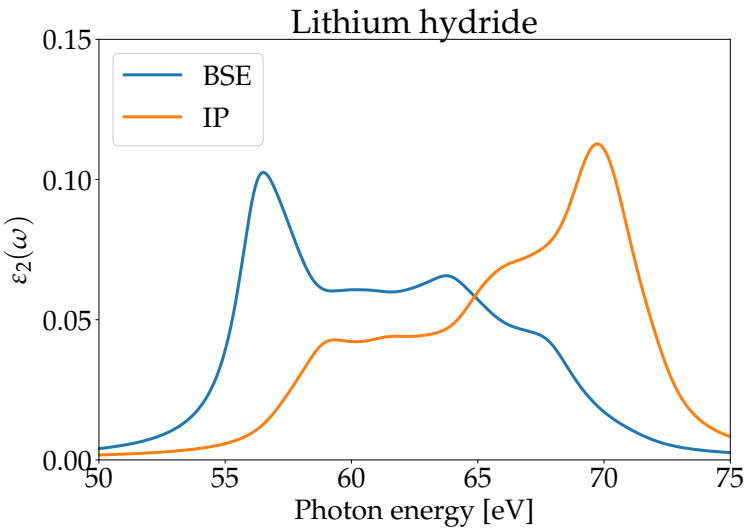

Figure 2.4: Imaginary part of the dielectric function of Lithium hydride at the Li K-edge, calculated with the EXCITING code. The dielectric function shows strong excitonic effects as seen from the difference between the BSE and the independent particle (IP) result.

would choose c and v to run over the first valence and conduction bands. For an XUV or x-ray edge we would choose c to run over the respective core states.

In the Hamiltonian formulation the wave function must satisfy a BSE Schroedinger equation

$$H_{bse}\ \phi^{\lambda}(\mathbf{r}_e, \mathbf{r}_h) = E^{\lambda}\phi^{\lambda}(\mathbf{r}_e, \mathbf{r}_h)$$

The eigenvectors $\phi^{\lambda}(\mathbf{r}_e, \mathbf{r}_h)$ are the exciton wave functions and their modulo square are the joint probability density of electron and hole. The BSE-Hamiltonian can be split into three summands.

$$H_{bse} = H_{diag} + H_{dir} + H_{exc}$$

The diagonal part H_{diag} contains the one-particle energies and is already diagonal in the basis of Eq. (2.3). The direct part H_{dir} is a direct but screened coulomb interaction, while the exchange part H_{exc} is an exchange interaction but unscreened. Before we state explicit formulas for the three parts of the Hamiltonian, we first rewrite the Schrödinger equation into a matrix equation using Eq. (2.3)

$$\sum_{v'c'\mathbf{k}'} H^{bse}_{vc\mathbf{k},v'c'\mathbf{k}'} A^{\lambda}_{v'c'\mathbf{k}'} = E^{\lambda} A^{\lambda}_{vc\mathbf{k}}$$

Now the BSE problem has been reduced to the inversion of $H^{bse}_{vc\mathbf{k},v'c'\mathbf{k}'}$ in order to find the Eigenvalue E^{λ} and Eigenvectors $A^{\lambda}_{vc\mathbf{k}}$, which can be used to calculate the dielectric function.

In this basis the three summands of the BSE can be written as follows. The diagonal term simply contains the energies from the one-particle calculation and is, as its name implies,

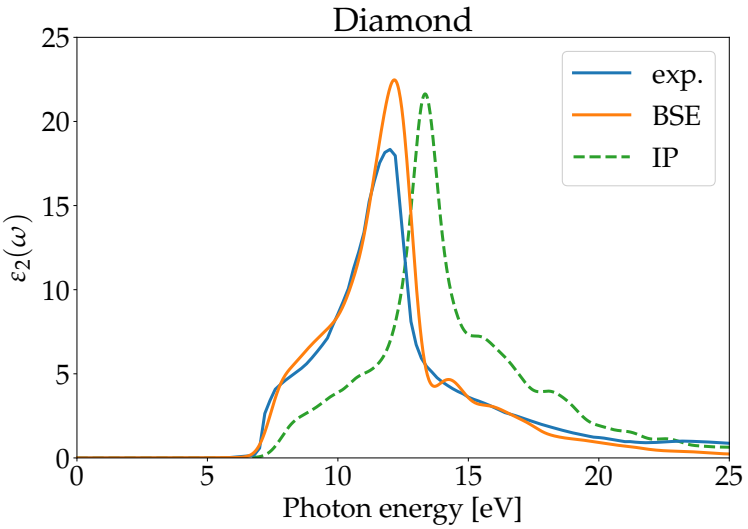

Figure 2.5: Imaginary part of the dielectric function $\varepsilon_2(\omega)$ at the onset of optical absorption, i.e. above the band gap from experiment (exp.) [PT64], the BSE method and the IP method. Both BSE and IP were calculated with the EXCITING code. BSE shows good agreement with the experiment with only one free parameter, namely broadening of the spectrum. Although no new peaks appear in BSE compared to IP the spectrum is still strongly affected by the electron hole interaction.

already diagonal in this basis.

$$H^{\text{diag}}_{vck,v'c'k'} = (\varepsilon_{ck} - \varepsilon_{vk})\delta_{cc'}\delta_{vv'}\delta_{kk'}$$

The energies of the hole ε_{vk} are counted negatively. The direct term is now a simple Hartree Coulomb interaction term, except that the Coulomb potential is replaced by a screened Coulomb potential. The screening is accounted for by the dielectric function $\varepsilon_r(\mathbf{r}, \mathbf{r}', \omega = 0)$ of the material, which is calculated within the one-particle theory, e.g. GW or DFT.

$$\begin{aligned} H^{\text{dir}}_{vck,v'c'k'} &= -\iint \psi_{vk}(\mathbf{r})\psi^*_{ck}(\mathbf{r}')W(\mathbf{r},\mathbf{r}')\psi^*_{v'k'}(\mathbf{r})\psi_{c'k'}(\mathbf{r}')\,\mathrm{d}^3\mathbf{r}\,\mathrm{d}^3\mathbf{r}' \\ &= \langle ck|\langle v'k'|\hat{W}|vk\rangle|c'k'\rangle \\ W(\mathbf{r},\mathbf{r}') &= \frac{e^2}{4\pi\varepsilon_0}\int \frac{\varepsilon^{-1}(\mathbf{r},\mathbf{r}'')}{|\mathbf{r}''-\mathbf{r}'|}\,\mathrm{d}^3\mathbf{r}'' \end{aligned}$$

The exchange term is usually of smaller magnitude and opposite sign than the direct term. In this case this means that the energy is increased by the exchange term. The exchange term is relatively small in this case as it involves brackets between hole and valence states like $\langle ck|\hat{V}|vk\rangle$ that are small for core holes because of the small overlap. In the case of a triplet exciton, i.e. a state where hole and electron spin add to a $|S = 1\rangle$ state, the exchange term vanishes similarly to Hartree-Fock.

$$\begin{aligned} H^{\text{exc}}_{vck,v'c'k'} &= -\frac{e^2}{4\pi\varepsilon_0}\iint \frac{\psi^*_{v'k'}(\mathbf{r}')\psi^*_{ck}(\mathbf{r})\psi_{vk}(\mathbf{r})\psi_{c'k'}(\mathbf{r}')}{|\mathbf{r}-\mathbf{r}'|}\,\mathrm{d}^3\mathbf{r}\,\mathrm{d}^3\mathbf{r}' \\ &= \langle v'k'|\langle ck|\hat{V}|vk\rangle|c'k'\rangle \end{aligned}$$

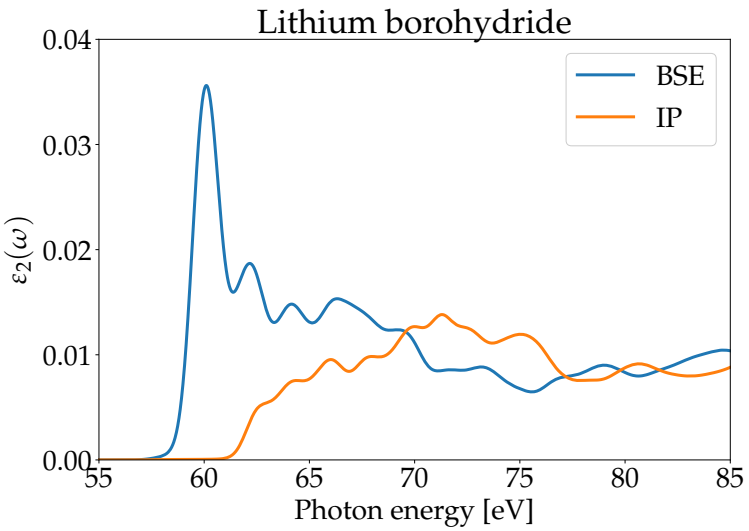

Figure 2.6: Imaginary part of the dielectric function of lithium borohydride, calculated by Eric Shirley as published in [WRW+17]. Lithium borohydride shows a strong exciton peak at 60 eV in the BSE calculation in contrast to the IP result, where no such peak is observed.

With all these ingredients the dielectric function can be calculated with linear response theory.

$$\varepsilon_2(\omega)_{ij} = \frac{8\pi^2}{\Omega} \sum_{\lambda} \sum_{vc\mathbf{k}} \left|A^{\lambda}_{vc\mathbf{k}}\right|^2 \frac{\langle c\mathbf{k}|\hat{p}_i|v\mathbf{k}\rangle\langle v\mathbf{k}|\hat{p}_j|c\mathbf{k}\rangle}{\varepsilon_{v\mathbf{k}} - \varepsilon_{c\mathbf{k}}} \delta(E^{\lambda} - \omega)$$

This formula is similar to the simple one-particle linear response result (Eq. (2.2)) except that the matrix elements are weighted according to the BSE eigenvectors $\left|A^{\lambda}_{vc\mathbf{k}}\right|^2$ and the simple one-particle energies are replaced by the BSE eigenvalues E^{λ}.

The calculations of x-ray absorption spectra of lithium borohydride (see Fig. 2.6) were performed by Eric. L Shirley. He used a BSE code developed by himself, which is a slight variation from the most recent version of the OCEAN code [VSRK11]. In the BSE scheme firstly a SCF calculation is performed to find the one-particle energies and wave functions. Here a pseudo potential DFT treatment with an LDA exchange correlation functional was used. The basis was a plane-wave basis with 100 Rydberg energy cutoff [4] and a $4 \times 4 \times 4$, $(1/2, 1/2, 1/2)$-shifted Monkhorst-Pack k-grid was used. BSE requires all electron wave function and is not readily compatible with pseudo potential results. An OPF scheme developed by Shirley [Shi04] was used. OPF is a method for k-space interpolation and basis reduction, which also allows for the reconstruction of core wave function from pseudo potential wave functions. The BSE Hamiltonian was solved with 235 bands, of which 16 were occupied [5]

[4] The plane waves k-vectors run over the inverse lattice so the basis is $\{|\mathbf{k}\rangle\}$ with $\mathbf{k} = h\mathbf{b}_1 + k\mathbf{b}_2 + l\mathbf{b}_3$ and $\frac{\hbar^2\mathbf{k}^2}{2m} < 100$ Rydberg.

[5] 16 bands means 32 electrons per unit cell. There are four units of $LiBH_4$. Li and H both contribute one electron per atom,while boron contributes three. The Li 1s and B 1s states are treated within the pseudo potentials.

2.3 Phonons within the Born-Oppenheimer-Approximation

In principle all elementary excitations in a solid are combined excitations of nuclei and electrons, e.g. phonon modes, i.e. vibrational excitation of the nuclei, will always be accompanied by movement of the electrons. In some cases such as soft-modes this has been shown to be of great importance and cannot be neglected. In many other cases, however, electron and nuclear motion can be safely decoupled due to the large mass ratio of the two species. The typical scheme to decouple electron and nuclear degrees of freedom is the Born-Oppenheimer approximation (BOA), which will be described in detail in Sec. 2.3.1. It leads to an effective electronic potential for the nuclei, which often can be reasonably well described by a harmonic approximation (Sec. 2.3.2), and therefore yields an extremely simple description of nuclear motion.

2.3.1 Born-Oppenheimer-Approximation

In this subsection we will loosely follow [Czy16]. The electrons and nuclei that form a solid have a very large mass ratio of at least $\frac{m_p}{m_e} \approx 1836$ for the hydrogen atom and respectively more for heavier nuclei. In a simple estimation the typical time scale is at least by a factor $\sqrt{\frac{m_p}{m_e}} \approx 43$ faster for electrons. This different timescale encourages an approximation that separates nuclear and electronic degrees of freedom, the Born-Oppenheimer-Approximation by Max Born and Robert Oppenheimer [OB27].

The full general solid state Hamiltonian is given by:

$$\hat{H} = \underbrace{\hat{T}_e + \hat{V}_{ee} + \hat{V}_{ne}}_{\hat{H}_0} + \hat{T}_n + \hat{V}_{nn}$$

with $\hat{T}_n, \hat{T}_e$ the kinetic energy operators and $\hat{V}_{ij}$ the bare coulomb interaction within the species (ee: electrons, nn: nuclei) and between nuclei and electrons (ne). First we look on solutions of the electronic problem with frozen (e.g. classical) nuclear coordinates $\mathbf{R}$, which is given by the $\hat{H}_0(\mathbf{R})$ Hamiltonian.

$$\hat{H}_0|\phi_i(\mathbf{R})\rangle = \varepsilon_i|\phi_i(\mathbf{R})\rangle \tag{2.4}$$

The solutions to Eq. (2.4) span the Hilbert space of the electronic problem for every fixed $\mathbf{R}$

$$\sum_i |\phi_i(\mathbf{R})\rangle\langle\phi_i(\mathbf{R})| = \mathbb{I},$$

therefore the full wave function $|\Psi\rangle$ must be expandable by this set of vectors as

$$\langle\mathbf{R}|\Psi\rangle = \sum_i \chi_i(\mathbf{R})|\phi_i(\mathbf{R})\rangle$$

Insertion in the full Hamiltonian yields

$$\begin{aligned}(\hat{H} - E)\langle\mathbf{R}|\Psi\rangle &= \sum_i \big(\hat{H}_0 + \hat{T}_n - E\big)\chi_i(\mathbf{R})|\phi_i(\mathbf{R})\rangle \\ &= \sum_i \big(\varepsilon_i(\mathbf{R}) + \hat{T}_n - E\big)\chi_i(\mathbf{R})|\phi_i(\mathbf{R})\rangle = 0\end{aligned}$$

After multiplication from the left with $\langle\phi_j(\mathbf{R})|$

$$= \sum_i \langle\phi_j(\mathbf{R})|\hat{T}_n\chi_i(\mathbf{R})|\phi_i(\mathbf{R})\rangle + (\varepsilon_j - E)\chi_j(\mathbf{R}) = 0$$

Evaluating the first term with the product rule and $\hat{T}_n = \sum_l -\frac{\hbar^2}{2M_l}\partial^2_{\mathbf{R}_l}$ yields

$$\partial^2_{\mathbf{R}_l}\chi_i(\mathbf{R})\phi_i(\mathbf{R}) = \phi_i(\mathbf{R})\partial^2_{\mathbf{R}_l}\chi_i(\mathbf{R}) + 2(\partial_{\mathbf{R}_l}\chi_i(\mathbf{R})(\partial_{\mathbf{R}_l}\phi_i(\mathbf{R})) + \chi_i(\mathbf{R}\partial^2_{\mathbf{R}_l}\phi_i(\mathbf{R})$$

The first term of A_{ji} represents the standard kinetic energy of the nuclei and so it is useful to separate it from the more complicated other two terms in the following Schroedinger equation for $\chi(\mathbf{R})$.

$$(\hat{T}_n + \hat{V}_{nn} + \varepsilon_j)\chi_j(\mathbf{R}) + \sum_i \hat{A}_{ji}\chi_i(\mathbf{R}) = E\chi_j(\mathbf{R})$$

$$A_{ji} = \sum_l \frac{\hbar^2}{2M_l}\left(\langle\phi_j(\mathbf{R})|\partial^2_{\mathbf{R}_l}|\phi_i(\mathbf{R})\rangle + 2\langle\phi_j(\mathbf{R})|\partial_{\mathbf{R}_l}|\phi_i(\mathbf{R})\rangle\partial_{\mathbf{R}_l}\right)$$

The first term can be interpreted as the kinetic energy of the electrons due to the movement of the nuclei. The Born-Oppenheimer-Approximation is now to neglect both terms in A_{ji}, e.g. to set $A_{ji} = 0$. This leads to two equations of motion for nuclei and electrons

$$\begin{aligned}
&\text{electrons :} && (\hat{T}_e + \hat{V}_{ee} + \hat{V}_{en}(\mathbf{R}))|\phi_i(\mathbf{R})\rangle = \varepsilon_i(\mathbf{R})|\phi_i(\mathbf{R})\rangle \\
&\text{nuclei :} && (\hat{T}_n + \hat{V}_{nn} + \varepsilon_i(\mathbf{R}))\chi_i(\mathbf{R}) = E\chi_i(\mathbf{R}) \\
&\text{wavefunction :} && \langle\mathbf{R}|\Psi\rangle = \sum_i \chi_i(\mathbf{R})|\phi_i(\mathbf{R})\rangle \\
& && \langle\mathbf{r},\mathbf{R}|\Psi\rangle = \Psi(\mathbf{r},\mathbf{R}) = \sum_i \chi_i(\mathbf{R})\phi_i(\mathbf{R})
\end{aligned}$$

If one is interested in ground state or near ground state properties one typically solves the electronic problem with frozen classical nuclei first at some initial point for the nuclear positions, e.g. the experimental value. Then one can proceed to iteratively find the global minimum of the energy landscape $E_n = \varepsilon(\mathbf{R}) + V_{nn}(\mathbf{R})$

$$\min_{\mathbf{R}}(\varepsilon(\mathbf{R}) + V_{nn}(\mathbf{R})) = E_n(\mathbf{R}_0)$$

$\mathbf{R}_0$ is now the ground state structure of our theoretical description. From this starting point one can now solve the quantum mechanical nuclear problem with for example the harmonic approximation to be discussed next.

2.3.2 Normal modes within the harmonic approximation

The nuclear problem near the ground state is now given by the Hamiltonian

$$\hat{H}_n = \hat{T}_n + \underbrace{\hat{\varepsilon} + \hat{V}_{nn}}_{\hat{V}_{\text{eff}}}$$

We expand $\hat{V}_{\text{eff}}$ in a Taylor series at $\mathbf{R} = \mathbf{R}_0$ and new coordinates $\mathbf{X} = \mathbf{R} - \mathbf{R}_0$

$$\begin{aligned} V_{\text{eff}}(\mathbf{X}) &= V_{\text{eff}}(0) + \underbrace{\partial_{\mathbf{X}} V_{\text{eff}}(\mathbf{X})|_0}_{=0}\mathbf{X} + \frac{1}{2}\sum_{ij} \partial_{X_i}\partial_{X_j} V_{\text{eff}}(\mathbf{X})\big|_0 X_i X_j + \mathcal{O}(\mathbf{X}^3) \\ &\approx V_{\text{eff}}(0) + \frac{1}{2}\mathbf{X}^t\mathbf{K}\mathbf{X} \end{aligned}$$

with $K_{ij} = \partial_{X_i}\partial_{X_j} V_{\text{eff}}(\mathbf{X})$. $\partial_{\mathbf{X}} V_{\text{eff}}(\mathbf{X})|_0$ must vanish because $\mathbf{R}_0$ is a minimum of the effective potential. The Hamiltonian now reads

$$\begin{aligned} \hat{H}_n &= \hat{T}_n + \frac{1}{2}\mathbf{X}^t\mathbf{K}\mathbf{X} \\ &= \sum_l \frac{\hat{p}_l^2}{2M_l} + \frac{1}{2}\mathbf{X}^t\mathbf{K}\mathbf{X} \end{aligned}$$

The coordinate transform

$$Q_l = M_l^{1/2} X_l$$

is helpful to remove the explicit mass dependency of the kinetic energy operator. Then

$$\xi = M^{-1/2}\mathbf{P} \qquad \text{or} \xi = -i\hbar\boldsymbol{\nabla}_{\mathbf{Q}}$$

In this coordinate system the Hamiltonian reads

$$\hat{H}_n = \frac{1}{2}\xi^t\xi + \frac{1}{2}\mathbf{Q}^t \underbrace{\mathbf{M}^{-1/2}\mathbf{K}\mathbf{M}^{1/2}}_{=\mathbf{K}}\mathbf{Q}$$

The nuclear problem is now reduced to finding the eigenvalues ω_i^2 and eigenvectors $\mathbf{l}_i$ of $\mathbf{K}$. In the Eigenbasis the Hamiltonian is given by

$$\hat{H}_n = \sum_i \frac{\zeta_i^2}{2} + \frac{1}{2}\omega_i^2\hat{q}_i^2 \qquad \text{and} \quad \mathbf{Q} = \sum_i q_i\mathbf{l}_i$$

which is a set of uncoupled harmonic oscillators. Each term of the sum, e.g. each mode can be separately solved with

$$\begin{aligned} \hat{H}_i &= \frac{\zeta_i^2}{2} + \frac{1}{2}\omega_i^2\hat{q}_i^2 \\ \hat{H}_i|\psi_i\rangle &= \epsilon_i|\psi_i\rangle \end{aligned}$$

The expectation value for the nuclear displacement is then

$$\langle X\rangle = \mathbf{M}^{-\frac{1}{2}}\sum_i \langle q_i\rangle\mathbf{l}_i \tag{2.5}$$

The full nuclear wave function is then a product state, i.e.

$$|\chi\rangle = \prod_i |\psi_i\rangle$$

with $|\psi_i\rangle$ being the wave function of a single oscillator. A state $|0\rangle = |0_1 i_2 \dots 0_{3N}\rangle$ would for example represent the nuclear ground state. A state $|\alpha_i\rangle = |0\rangle_1|0\rangle_2 \dots |\alpha\rangle_i \dots |0\rangle_{3N}$ would represent a state where all modes are in the ground state, except for the i-th which is in the a coherent state with coherent parameter α ($E \propto |\alpha|^2$, $\langle x\rangle \propto \operatorname{Re}\alpha$). This however still represents a coherent movement of all nuclei due to the vectorial nature of the eigenvectors and modes. The nuclear displacement of a coherent state in mode i is given by

$$\langle R\rangle_\alpha = M^{-1/2}\langle Q\rangle_\alpha = M^{-1/2}\operatorname{Re}(\alpha)\cdot\mathbf{l}_i$$

2.4 The Raman Effect

The Raman effect is an inelastic scattering process for light, where a photon with energy $\hbar\omega_0$ interacts with matter and experiences a frequency shift to an energy of $\hbar\omega_0 \pm \Delta E$. As a consequence the material is either excited or de-excited upon this interaction. The effect was discovered by Chandrasekhara Venkata Raman and coworkers in 1928 [6] and quickly established as a widely used type of spectroscopy. Raman spectroscopy allows for the study of vibrational and rotational modes of of gases, liquids or solids. The frequencies of such modes lie in the infrared, Raman spectroscopy however allows for a study of such modes in the optical region. Spontaneous Raman spectroscopy requires a monochromatic light source, whose frequency can be off resonant to transitions of the material, while IR spectroscopy requires a broadband source that contains exactly the frequencies of the modes, which are under study. For materials with inversion symmetry IR and Raman spectroscopy yield complementary information as a particular mode is either Raman or IR active. An IR active vibrational mode displays a finite transition dipole moment $\mathbf{d} = -e\langle f|\mathbf{r}|i\rangle$, while a Raman active mode displays a finite Raman polarizability tensor $\frac{\partial \chi}{\partial q_\alpha}$. Because of their different symmetry, $\mathbf{d}$ transforms as x, y, z and a tensor transforms as $x^2, xy, xz, y^2 \ldots$, a mode can either be Raman or IR active if the material exhibits inversion symmetry. Without inversion symmetry a vibrational mode can be both IR and Raman active.

The simplest theoretical approach of the Raman effect is purely classical. We will assume that a monochromatic light field

$$\mathbf{E} = \mathbf{E}_0 \cos(\omega_0 t)$$

interacts with matter via the polarization (solid) or the dipole moment (molecules).

$$\begin{aligned} \mathbf{P} &= \chi \mathbf{E} = \chi \mathbf{E}_0 \cos(\omega_0 t) && \text{(solids)} \\ \mathbf{p} &= \alpha \mathbf{E} = \alpha \mathbf{E}_0 \cos(\omega_0 t) && \text{(molecules)}, \end{aligned} \tag{2.6}$$

where $\mathbf{P}$ is the macroscopic polarization, χ the electronic susceptibility, $\mathbf{p}$ the molecular dipole moment and α the molecular polarizability. Historically the molecular notation for the Raman effect dominates, while in this thesis we will dominantly use the solid state notation. Classically we will assume that the material is already vibrating coherently e.g. by thermal excitation. The electric susceptibility should depend on the nuclear normal coordinates and can be expanded in a Taylor series.

$$\chi(\mathbf{q}) = \chi_0 + \sum_\alpha \frac{\partial \chi}{\partial q_\alpha} q_\alpha + \mathcal{O}(\mathbf{q}^2)$$

Classically excited normal coordinates are oscillating harmonically

$$q_\alpha = q_{\alpha,0} \cos(\omega_\alpha t)$$

[6] For a historical introduction see Sec. 1.1

Inserting both equations into Eq. (2.6) and using a trigonometric identity yield

$$\mathbf{P} = \chi_0 \mathbf{E}_0 \cos(\omega_0 t) + \frac{1}{2}\mathbf{E}\sum_\alpha \frac{\partial \chi}{\partial q_\alpha} q_\alpha [\cos((\omega_0 - \omega_\alpha)t) + \cos((\omega_0 + \omega_\alpha)t)]$$

The polarization oscillates at $\omega_0 \pm \omega_\alpha$, which gives rise to the Stokes (-) and anti-Stokes (+) Raman line, which are observed in the experiment. The classical approach shows some important properties of the Raman effect such as the existence of the Stokes and anti-Stokes line and the interaction of light and vibrations via $\frac{\partial \chi}{\partial q_\alpha}$ (solids) or $\frac{\partial \alpha}{\partial q_\alpha}$, also called the Raman polarizability. The tensorial nature of this Raman polarizability leads to many important aspects regarding the symmetry of the material and the mode under study. However it fails to predict an absolute scattering amplitude and it predicts equal intensity for the Stokes and anti-Stokes line, which is not observed in the experiment. The next level of sophistication is the semi-classical approach[7], which can be used to describe coherent impulsive Raman scattering, which is central to this thesis. Starting point is the electromagnetic field energy within matter in the Power-Zienau-Woolleyg gauge

$$\begin{aligned}
H_{\text{field}} &= \frac{1}{2}\int \mathbf{E}\cdot\mathbf{D}\, d^3\mathbf{r} + \text{magnetic.} \\
\mathbf{D} &= \varepsilon_0 \mathbf{E} + \mathbf{P} \\
\mathbf{P}(\mathbf{r}) &= \int \chi(\mathbf{r}-\mathbf{r}')\mathbf{E}(\mathbf{r}')\, d^3\mathbf{r}' \\
H_{\text{field}} &= \frac{1}{2}\varepsilon_0 \int \mathbf{E}^2\, d^3\mathbf{r} + \frac{1}{2}\varepsilon_0 \int \mathbf{E}(\mathbf{r}) \int \chi(\mathbf{r}-\mathbf{r}')\mathbf{E}(\mathbf{r}')\, d^3\mathbf{r}'\, d^3\mathbf{r}
\end{aligned}$$

As the second term contains a convolution in real space it is generally favorable to switch to k-space. We define the Fourier transformations as

$$\begin{aligned}
\chi(\mathbf{r}-\mathbf{r}') &= \frac{1}{(2\pi)^3}\int \chi(\mathbf{k}) e^{-i\mathbf{k}(\mathbf{r}-\mathbf{r}')}\, d^3\mathbf{k} \\
\mathbf{E}(\mathbf{r}) &= \frac{1}{(2\pi)^3}\int \mathbf{E}(\mathbf{k}') e^{-i\mathbf{k}'\mathbf{r}}\, d^3\mathbf{k}'
\end{aligned}$$

The transformed Hamiltonian reads

$$H_{\text{field}} = \frac{1}{2(2\pi)^3}\varepsilon_0 \int |\mathbf{E}(\mathbf{k})|^2\, d^3\mathbf{k} + \frac{1}{2(2\pi)^3}\varepsilon_0 \int \mathbf{E}(-\mathbf{k})\chi(\mathbf{k})\mathbf{E}(\mathbf{k})\, d^3\mathbf{k}$$

Similar to the classical approach we assume that χ depends on the k vector and the normal coordinates $\mathbf{q} = \{q_1(\mathbf{k}_q), ..., q_\alpha(\mathbf{k}_q), ...\}$ and can be expanded into a Taylor series

$$\chi(\mathbf{k}) = \chi_0(\mathbf{k}) + \sum_{\alpha,\mathbf{k}_q} \frac{\partial \chi(\mathbf{k})}{\partial q_\alpha(\mathbf{k}_q)} q_\alpha(\mathbf{k}_q) + \mathcal{O}(q_\alpha^2)$$

The sum over α represents different modes within the unit cell, while the sum over $\mathbf{k}_q$ represents different phases between the unit cells. In other words we have to sum over the

[7] Quantum mechanical matter but classical electromagnetic field

complete Phonon band structure, where α is the band index and $\mathbf{k}_q$ the k-vector. We can insert the truncated series into the field Hamiltonian

$$H_{\text{field}} = \underbrace{\frac{\varepsilon_0}{2(2\pi)^3}\int \mathbf{E}(-\mathbf{k})(1+\chi_0)\mathbf{E}(\mathbf{k})\,d^3\mathbf{k}}_{\text{Field energy}} + \underbrace{+\frac{1}{2(2\pi)^3}\varepsilon_0\sum_{\alpha,\mathbf{k}_q}\int \mathbf{E}(-\mathbf{k})\frac{\partial\chi(\mathbf{k})}{\partial q_\alpha(\mathbf{k}_q)}q_\alpha(\mathbf{k}_q)\mathbf{E}(\mathbf{k})\,d^3\mathbf{k}}_{\text{Raman}}$$

The first term is the electromagnetic field energy in matter with a purely electronic susceptibility. It describes how the electron density relocates under the influence of an external electric field. The second term, which is responsible for Raman scattering, describes the effect of the change in electron density in response to the nuclei. If an external electric field is present the electron density adjusts, which leaves the nuclei not in their energetically optimal positions anymore, which means that there is a force exerted to the nuclei. To introduce quantum mechanical effects we can replace the classical coordinates q_α by the position operator $\hat{q}_\alpha$

$$H_{\text{raman}} = \frac{\varepsilon_0}{2(2\pi)^3}\sum_{\alpha,\mathbf{k}_q}\int \mathbf{E}(-\mathbf{k})\frac{\partial\chi(\mathbf{k})}{\partial q_\alpha(\mathbf{k}_q)}\hat{q}_\alpha(\mathbf{k}_q)\mathbf{E}(\mathbf{k})\,d^3\mathbf{k}$$

For optical phonon modes with an almost flat dispersion around $k \approx 0$ it is a good approximation to assumes that $\frac{\partial\chi(\mathbf{k})}{\partial q_\alpha(\mathbf{k}_q)}\hat{q}_\alpha(\mathbf{k}_q)$ is diagonal with regard to $\mathbf{k}, \mathbf{k}_q$, which means that we can drop the sum over $\mathbf{k}_q$ and replace $\mathbf{k}_q$ by k, which yields

$$H_{\text{raman}} = \frac{\varepsilon_0}{2(2\pi)^3}\sum_{\alpha}\int \mathbf{E}(-\mathbf{k})\frac{\partial\chi(\mathbf{k})}{\partial q_\alpha(\mathbf{k})}\hat{q}_\alpha(\mathbf{k})\mathbf{E}(\mathbf{k})\,d^3\mathbf{k}$$

$$\frac{1}{(2\pi)^3}\int d^3\mathbf{k} \to \frac{1}{V_{\text{uc}}}\sum_{\mathbf{k}}$$

where V_{uc} is the unit cell volume. Together with the definition of the (molecular) Raman polarizability

$$\frac{\partial\alpha(\mathbf{k})}{\partial q_\alpha(\mathbf{k})} = \varepsilon_0 V_{\text{uc}}\frac{\partial\chi(\mathbf{k})}{\partial q_\alpha(\mathbf{k})}$$

yields the Raman Hamiltonian its final form

$$\boxed{H_{\text{raman}} = \frac{1}{2V_{\text{uc}}^2}\sum_{\alpha,\mathbf{k}}\mathbf{E}(-\mathbf{k})\frac{\partial\alpha(\mathbf{k})}{\partial q_\alpha(\mathbf{k})}\hat{q}_\alpha(\mathbf{k})\mathbf{E}(\mathbf{k})}$$

H_{raman} can now be used as a perturbation to a nuclear system. The transition rate according to Fermi's golden rule is

$$\begin{aligned} t_{fi} &= \frac{2\pi}{\hbar}|\langle f|H_{\text{raman}}|i\rangle|^2\delta(E_i - E_m - \hbar\Delta\omega) \\ &= \frac{2\pi}{\hbar V_{\text{uc}}^2}\sum_{\alpha,\mathbf{k}}\left|\mathbf{E}(-\mathbf{k})\frac{\partial\alpha_{ij}(\mathbf{k})}{\partial q_\alpha(\mathbf{k})}\mathbf{E}(\mathbf{k})\right|^2|\langle f|\hat{q}_\alpha|i\rangle|^2\delta(E_i - E_m - \hbar\Delta\omega) \end{aligned} \quad (8)$$

$$\hat{q}_\alpha = \sqrt{\frac{\hbar}{2\omega_\alpha}}\left(a_\alpha + a_\alpha^\dagger\right)$$

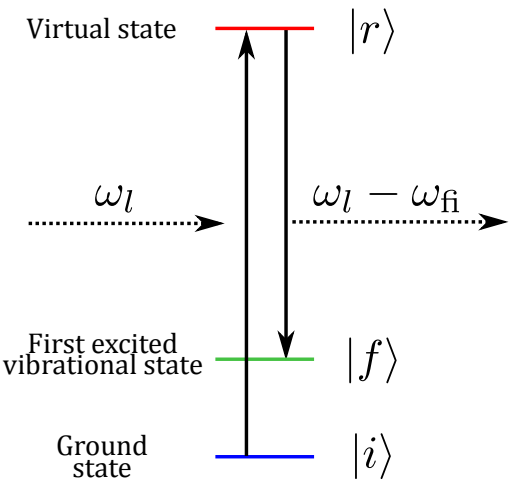

Figure 2.7: Stokes Raman scattering. An incoming photon with frequency ω_l is inelastically scattered to $\omega_l - \omega_{fi}$. The process can be thought of an electron being excited into a virtual state $|r\rangle$ and de-excited by emission of a photon into the final, vibrational state $|f\rangle$.

The quantum-mechanical operators for the phonon coordinates yield the correct behavior for the relative intensities of Stokes and Anti-Stokes scattering, e.g. if the initial state is the ground state $|i\rangle = |00\dots0_\alpha\dots0\rangle$ there are only Stokes lines. The Matrix element $\langle f|\hat{q}_\alpha|i\rangle$ is only finite in the harmonic case if vibrational quantum number changes by $\Delta v = \pm 1$, i.e. $\Delta\omega = \pm\omega_\alpha$, which directly observed in the experiment.

So far we based our theory on the Taylor expansion of the susceptibility, which leaves us with the determination of $\frac{\partial\alpha}{\partial q_\alpha}$ from ab-initio theory or experimental means. One possibility would be to calculate $\alpha(\mathbf{q})$ with DFT or BSE within the BOA and simply take the derivative in $\frac{\partial\alpha}{\partial q_\alpha}$ by sampling $\alpha(\mathbf{q})$ for some values of q_α around the ground state. A full quantum mechanical treatment of the Raman effect is also possible, which allows to calculate the intensities of the Raman peaks purely from ground state properties. Here the dipole operator is used as a perturbation to the molecular or solid state Hamiltonian of the system within time dependent perturbation theory.

$$H_{pert} = -\mathbf{E}\cdot\mathbf{d} = -\frac{1}{2}\left(\mathbf{E}_0 e^{-i\omega_0 t} + \mathbf{E}_0^* e^{i\omega_0 t}\right)\cdot\mathbf{d}$$

Time dependent perturbation theory allows us to expand the perturbed wave function in powers of the perturbation

$$|i'\rangle = \left|i^{(0)}\right\rangle + \left|i^{(1)}\right\rangle + \cdots$$

where $|i'\rangle$ is the fully perturbed state, $\left|i^{(0)}\right\rangle$ is the unperturbed ground state and $\left|i^{(i)}\right\rangle$ is the i-th order correction due to the external perturbation. Restricting to first order gives

$$\begin{aligned}\left|i^{(1)}\right\rangle = \frac{1}{\hbar}\sum_{r\neq i}\frac{\left\langle r^{(0)}\middle|\mathbf{d}\middle|i^{(0)}\right\rangle}{\omega_{ri}-\omega_0}\left|r^{(0)}\right\rangle\mathbf{E}_0\, e^{-i(\omega_{ri}+\omega_0)t} + \\ + \frac{\left\langle r^{(0)}\middle|\mathbf{d}\middle|i^{(0)}\right\rangle}{\omega_{ri}+\omega_0}\left|r^{(0)}\right\rangle\mathbf{E}_0^*\, e^{-i(\omega_{ri}+\omega_0)t}\end{aligned} \tag{2.7}$$

[8] Here it seems as if the transition rate depends on the size of the unit cell because of the $\frac{1}{V_{uc}^2}$ factor. However V_{uc} cancels out when $\mathbf{E}(\mathbf{k})$ is actually computed from $\mathbf{E}(\mathbf{r})$. For a plane wave $\mathbf{E}(\mathbf{k}) = \mathbf{E}_0\cdot V_{uc}\delta(\mathbf{k}-\mathbf{k}_0)$ holds, where $\mathbf{E}_0$ is the usual field in V/m, which can be derived from an experiment.

The two terms stem from the two exponential terms in the electric field. The first is a resonant term as the denominator can approach zero for $\omega_{ri} \to 0$, while the second term's denominator is always larger than zero. The transition dipole moment, whose modulus square is proportional to the Raman peak's intensities is given by

$$\begin{aligned}\mathbf{d}_{fi} &= \langle f' | \mathbf{d} | i' \rangle \\ &= \underbrace{\left\langle f^{(0)} \middle| \mathbf{d} \middle| i^{(0)} \right\rangle}_{\text{Dipole transitions}} + \underbrace{\left\langle f^{(1)} \middle| \mathbf{d} \middle| i^{(0)} \right\rangle + \left\langle f^{(0)} \middle| \mathbf{d} \middle| i^{(1)} \right\rangle}_{\text{Raman scattering}} + \cdots \end{aligned} \tag{2.8}$$

The first term is the unperturbed dipole transition and the second and third term are responsible for the Raman effect. They represent a correction to the dipole transition, due to the fact, that the wave function adapts to the external field. In other words the initial state adapts to the external electric field and the final states are also changed by the presence of this field. One can now insert Eq. (2.7) into Eq. (2.8), which is a rather lengthy calculation. The interested reader is referred to [Der02] for a complete derivation. The result is the so called Raman transition polarizability tensor

$$\alpha_{fi} = \frac{1}{\hbar} \sum_{r \neq f,i} \frac{\langle f^{(0)} | \mathbf{d} | r^{(0)} \rangle \langle r^{(0)} | \mathbf{d}^{\intercal} | i^{(0)} \rangle}{\omega_{rf} + \omega_0 + i\Gamma_r} + \frac{\langle r^{(0)} | \mathbf{d} | i^{(0)} \rangle \langle f^{(0)} | \mathbf{d}^{\intercal} | r^{(0)} \rangle}{\omega_{rf} - \omega_0 - i\Gamma_r} \tag{2.9}$$

Its modulus square is proportional to the intensity of the respective Raman line and the induced dipole is given by

$$\mathbf{p}^{(1)}(\omega_0 \pm \omega_{fi}) = \alpha_{fi} \mathbf{E}_0(\omega)$$

2.4.1 Perturbational Treatment of Impulsive Raman via the Raman Polarizability

We consider a situation in which a crystal is hit by an ultrashort light pulse, which is non-resonant to all transitions of the crystal, i.e. the dielectric function $\varepsilon(\omega)$ is approximately real for the full spectrum $S(\omega) = \frac{1}{Z}|E(\omega)|^2$ of the light pulse. In particular, we consider the situation that the photon energy is above all phonon transitions, i.e. $\hbar\omega_l > \hbar\omega_i \; \forall \, i$ but below the electronic transitions, i.e. $\hbar\omega_l < E_{gap}$. We will follow the derivation from [DRN94] in this subsection.

The Raman Hamiltonian is given by

$$\hat{H}(t) = \sum_i \frac{\zeta_i^2}{2} + \frac{1}{2}\omega_i^2 \hat{q}_i^2 + \hat{F}_i(t)$$

where $F(t)$ is the external perturbation due to the light pulse and is given by

$$\hat{F}(t) = -\frac{\partial \alpha}{\partial q_i} \underbrace{|E(t)|^2}_{I(t)} \hat{q}_i$$

For better readability we will drop in the following the index i for momentum and position operator, i.e. we only consider a single mode.

$$\hat{H} = \frac{\zeta^2}{2} + \frac{1}{2}\omega^2 \hat{q}^2 - \frac{\partial \alpha}{\partial q} I(t) \hat{q}$$

or using creation and annihilation operators

$$\hat{H} = \hbar\omega_i \hat{n} + \frac{\partial\alpha}{\partial q_i} I(t) \sqrt{\frac{\hbar}{2\omega}} \left(\hat{a}^\dagger + \hat{a}\right)$$

The Heisenberg equation of motion for $\hat{a}(t)$ reads

$$\begin{aligned}\partial_t \hat{a} &= -\frac{i}{\hbar}\left[\hat{H}, \hat{a}\right] = -i\omega_i[\hat{n}, \hat{a}] - \frac{i}{\sqrt{2\hbar\omega}} \frac{\partial\alpha}{\partial q_i} I(t) \underbrace{\left[\hat{a}^\dagger, \hat{a}\right]}_{=-1} \\ &= -i\omega_i \hat{a} + \frac{i}{\sqrt{2\hbar\omega}} \frac{\partial\alpha}{\partial q_i} I(t)\end{aligned}$$

This is a typical inhomogeneous differential equation and the solution of which is

$$\begin{aligned}\hat{a} &= e^{-i\omega_i t}\hat{a}_0 + \frac{i}{\sqrt{2\hbar\omega}} e^{-i\omega_i t} \int_{-\infty}^{t} e^{i\omega_i t'} \frac{\partial\alpha}{\partial q_i} I(t')\, dt' \\ &= e^{-i\omega_i t}\hat{a}_0 + e^{-i\omega_i t}\gamma(t)\end{aligned}$$

with $\gamma(t)$ defined as

$$\gamma(t) = \frac{i}{\sqrt{2\hbar\omega}} \frac{\partial\alpha}{\partial q_i} \int_{-\infty}^{t} e^{i\omega_i t'} I(t')\, dt' \tag{2.10}$$

The temporal evolution of the displacement, momentum and energy of the phonon mode (under the assumption that it was in the ground state before the excitation) are

$$\begin{aligned}q(t) &= \sqrt{\frac{\hbar}{2\omega_i}} \left\langle 0 \middle| \hat{a}(t) + \hat{a}^\dagger(t) \middle| 0 \right\rangle = \sqrt{\frac{2\hbar}{\omega_i}} |\gamma(t)| \sin(\omega_i t - \phi) \\ p(t) &= \sqrt{2\hbar\omega_i} |\gamma(t)| \cos(\omega_i t - \phi) \\ E(t) &= \hbar\omega_i \left(|\gamma(t)|^2 + \frac{1}{2} \right)\end{aligned} \tag{2.11}$$

We see that, if $\gamma(t)$ follows a step function the time, the mode will just oscillate harmonically and the displacement will be proportional to $|\gamma|$. From the definition of $\gamma(t)$ it is clear that $|\gamma|$ will change drastically during the external light pulse is present and will become constant afterwards.

If the pulse is short and we are only interested in the behavior at long times we can essentially set the upper integration bound in Eq. (2.10) to ∞. The integral then becomes a Fourier transformation and γ can be stated as following

$$\gamma(t) \overset{t\to\infty}{=} \frac{i}{\sqrt{2\hbar\omega}} \frac{\partial\alpha}{\partial q_i} \mathcal{F}(E(t)^2)(\omega_i) \tag{2.12}$$

where (F) denotes the Fourier transform. The amount of excitation of the respective modes with frequency ω_i depends both on the Raman coefficient $\frac{\partial\alpha}{\partial q}$ and on the value of the Fourier transform of $|E(t)|^2$ at the frequency ω_i. This is a consequence of the impulsive nature of coherent impulsive Raman excitation. Modes will only be excited if the (Fourier limited) light pulse is shorter than their oscillation period. Chirp plays a minor role if the

chirped pulse is still shorter than the oscillation period of the phonon mode. For a simple Gaussian pulse with pulse duration σ_t the Fourier transformation of its squared electric fields yields.

$$\mathcal{F}_\omega(E(t)^2) = \frac{E_0^2\sigma_t}{\sqrt{2}} e^{-\frac{\sigma_t^2\omega^2}{4}} \tag{2.13}$$

This is a Gaussian peak centered at $\omega = 0$ with width of $\Delta\omega = \frac{\sqrt{2}}{\sigma_t}$.

For a typical phonon frequency of $f \approx 1 - 30\,\mathrm{Thz}$ the pulse must be in the sub-picosecond to 30 fs range to effectively excite phonon modes. All phonon modes are excited according to their Raman coefficient up to a cutoff frequency given by $\sim \frac{1}{\pi\sigma_t}$ ($\frac{1}{e}$ value). This entire process can be imagined as a very short force impulse exerted to the nuclei caused by the (quasi instantaneous) displacement of the electrons according to their polarizability α and the external electric field. If the phonon mode's period is similar or shorter than the force pulse the force acts effectively like a delta spike.

2.4.2 Microscopic Picture: Transient Electron Density Approach

In a crystalline material the steady-state electron density $\rho_0(\mathbf{r})$, transient electron density $\Delta\rho(\mathbf{r}, t)$ and total electron density $\rho(\mathbf{r}, t) = \rho_0(\mathbf{r}) + \Delta\rho(\mathbf{r}, t)$ can be effectively studied by x-ray diffraction with Angstrom spatial resolution and femtosecond temporal resolution [CSG+99, CSB+00, CTS+01, BZG+04, RPJG+99, SZF+12].

We now consider the same situation as in the previous subsection, namely that a crystalline material in it's ground state is hit by a femtosecond light pulse, which is non-resonant to all transitions of the material. We assume that the transient electron density is known beforehand (either from a solution to the time dependent Schrödinger equation or experimentally measured by e.g. time resolved x-ray diffraction) and we are interested in the nuclear response.

The electronic Coulomb potential ϕ in the Coulomb gauge is given by

$$-\boldsymbol{\nabla}^2\phi(t) = \varepsilon_0(\rho_0 + \Delta\rho(t))$$

and the steady state electronic potential is given by

$$-\boldsymbol{\nabla}^2\phi_0 = \varepsilon_0\rho_0$$

In the periodic case, i.e. a crystal, it is especially helpful to rewrite these equations in k-space

$$\begin{aligned} k^2\tilde{\phi}(\mathbf{k}, t) &= \varepsilon_0(\tilde{\rho}_0(\mathbf{k}) + \Delta\tilde{\rho}(\mathbf{k}, t)) \\ \tilde{\phi}(\mathbf{k}, t) &= \frac{\varepsilon_0}{k^2}(\tilde{\rho}_0(\mathbf{k}) + \Delta\tilde{\rho}(\mathbf{k}, t)) \end{aligned}$$

After Fourier transform back to real space we get

$$\phi(\mathbf{r}, t) = \mathcal{F}_{\mathbf{k}}^{-1}\Big(\frac{\varepsilon_0}{k^2}(\tilde{\rho}_0(\mathbf{k}) + \Delta\tilde{\rho}(\mathbf{k}, t))\Big) \tag{2.14}$$

The force exerted to the nucleus i with charge $Z_i e$ is given by

$$\begin{aligned}\mathbf{F}_i &= -Z_i e \nabla_{\mathbf{r}} \phi(\mathbf{r}, t)|_{\mathbf{R}_i} = -Z_i e \underbrace{\nabla_{\mathbf{r}} \phi_0}_{=0} - Z_i e \nabla_{\mathbf{r}} \Delta\phi|_{\mathbf{R}_i} \\ &= -Z_i e \nabla_{\mathbf{r}} \Delta\phi|_{\mathbf{R}_i}\end{aligned}$$

We can also rewrite this in k-space

$$\mathbf{F}_i = i \cdot Z_i e \cdot \varepsilon_0 \mathcal{F}_{\mathbf{k}}^{-1}\left(\frac{\mathbf{k}}{k^2} \Delta\tilde{\rho}(\mathbf{k}, t)\right) \tag{2.15}$$

Finally we can define the total force vector $\mathbf{F}$ by combining all force vectors $\mathbf{F}_i$

$$\mathbf{F} = \begin{pmatrix} \mathbf{F}_0 \\ \mathbf{F}_1 \\ \vdots \\ \mathbf{F}_i \\ \vdots \\ \mathbf{F}_N \end{pmatrix}$$

The excitation of a Raman mode j with eigenvector $\mathbf{l}_j$ is proportional to the scalar product of eigenvector with the force vector, i.e.

$$\left|\frac{\partial \alpha}{\partial q_j}\right|^2 \propto \left|\mathbf{F} \cdot \mathbf{l}_j\right|$$

This emphasizes the complementary character of the two descriptions in this and the previous subsection.

3 Experiment

3.1 Overview of the experimental setup

Ultrafast time resolved absorption spectroscopy requires both pump and probe pulses that are temporally short and whose relative delay can be tuned with sufficient accuracy. The probe pulse must span the spectral region of interest and the pump pulse must be able to excite the material under study. There are numerous possibilities to combine different pump and probe pulses from different sources, which suits various scientific questions (see Sec. 1.2). For the experiments in this thesis we used pulses from a titanium sapphire (Ti:sapphire) laser at 800 nm wavelength from which both pump and pulses are derived. We use a two-color high-harmonic generation (HHG) scheme to generate femtosecond XUV pulses between 50-100 eV as a probe in this setup. The physics and details of the HHG can be found in Sec. 3.3, details of the temporal and and spectral properties of the pump can be found in Sec. 3.5. In this thesis we used optical pump pulses directly derived from the laser, i.e. at 800 nm wavelength. In Fig. 3.1 a schematic of the experimental setup is shown. The output of the Ti:sapphire laser, which is described in detail in Sec. 3.2, is sent onto a first 1:2 beam splitter and the $^2/_3\widehat{=}$20 mJ portion is sent into the optical parmetric amplifier (OPA). The OPA is described in detail in Sec. 3.2. It produces around 3 mJ output for the signal at 1.4 µm and 2 mJ for the idler at 1.9 µm. The OPA is tunable around a wide range of mid-IR frequencies. In all experiments in this thesis we fixed the signal wavelength to $\lambda_{\text{signal}} = 1.4\,\mu\text{m}$. The signal is then sent to the HHG-chamber and a gas cell, in which the harmonics are produced. The remaining portion of 10 mJ are split again by a 1:1 beam splitter. One part is, together with the idler from the OPA, used in another experiment. The remaining 5 mJ are split again by a 9:1 beam splitter. The 4.5 mJ are sent into the HHG vacuum chamber and the gas cell and the other 500 µJ are used as the pump pulse. Before the gas cell and high harmonic generation signal (mid-IR) and IR beam are combined in a collinear fashion with a dichroic mirror, that reflects IR and transmits mid-IR. Both IR and mid-IR are then focused by a $f = 1$ m focusing mirror into the gas cell. A delay stage (not shown) in the IR arm is used to overlap both beams temporally. The gas pressure in the HHG-cell is stabilized by a control loop gas valve, which sets the gas flux so that the pressure is constant inside the cell. In the experiment we used argon for two color HHG and Neon for single color HHG with a pressure of few hundreds of mbar. In the gas cell the XUV radiation is produced and travels through a differential pumping stage to the recombination chamber. The differential pumping chamber uses its own turbo pump and vacuum connections with a small diameter to reduce the gas flux from the HHG-chamber to the recombination chamber. In the recombination chamber a first thin metal filter is used to block the IR and mid-IR radiation. The remaining XUV radiation hits

a toroidal mirror under grazing incidence for higher reflectivity and is focused into the sample. The XUV radiation afterward travels through a dielectric hole mirror, i.e. just a standard mirror with a small central hole to let the XUV through. After the pump beam is split off by its beam splitter it travels through a $\lambda/2$ plate and a polarizing optic, which can be used to adjust the pump power and a delay stage, which determines the pump-probe delay. After the delay stage the pump beam is focused into the sample by a curved mirror with 1.5 m focusing length. It is recombined with the XUV probe in the recombination chamber with mirror with a small hole. On this mirror XUV probe and IR pump are spatially close and can be focused into the same spot on the sample almost colinearly. Behind the sample another metallic mirror is placed to filter out the pump beam, which is necessary because the camera is also very sensitive to IR and optical frequencies. The XUV radiation is dispersed by a grating and detected by a CCD camera. The detection setup is described in detail in Sec. 3.4. There are choppers in both the pump and the probe arm. The chopper in the pump arm runs at 12.5 Hz and allows to take pumped and unpumped frames consecutively in time at a rate of 25 Hz. The use of a chopper greatly reduces noise (see Sec. 3.5). The chopper in the probe arm is necessary because the CCD camera needs time to read out the image, during which it should not be exposed with light, because the sensor is still sensitive and the generated electron hole pairs will appear in the next image. The probe chopper runs at 25 Hz and is synchronized with the pump chopper such that the probe is open at the center of the pump opening (closing) window.

3.2 Laser system and OPCPA

Ultrafast absorption spectroscopy requires pulses that are sufficiently short in time and span the full spectral region of interest. Standard High harmonic generation fulfills the first requirement but not the second one, as its spectrum famously consists of equally spaced harmonics with gaps of no radiation in between. If one drives the HHG process with a superposition of two light pulses with frequencies with high least common multiple the HHG spectrum becomes continuous (Sec. 3.3), as favorable for absorption spectroscopy. We obtain the two distinct frequencies from a Ti:Sapphire laser with 800 nm central wavelength and an OPA, which delivers 1.4 µm (signal) and 1.9 µm (idler) [1]. The experiments in this thesis were performed with the signal.

Since its discovery as gain medium for femtosecond Kerr lens mode-locked lasers, Ti:sapphire has proven to be of unique value for ultrafast spectroscopy in the near infrared and beyond. Ti:sapphire is sapphire (Al_2O_3) doped with titanium atoms, typically with a concentration in the order of 0.1%, which form the active Ti^{3+} centers. Ti:sapphire offers a high emission cross section, large gain bandwidth from $\approx 650\,\text{nm} - 1100\,\text{nm}$, high thermal conductivity, especially at low temperatures and a high optical damage threshold. The Ti:Sapphire system we used is commercially available (KMLABS Red Dragon) delivers 30 W at a repetition rate of 1 kHz , i.e. 30 mJ pulse energy, with 35 fs pulse duration. It consists

[1] Signal and idler are the two outputs of an OPA. By definition signal is the one with higher frequency and idler the one with lower frequency

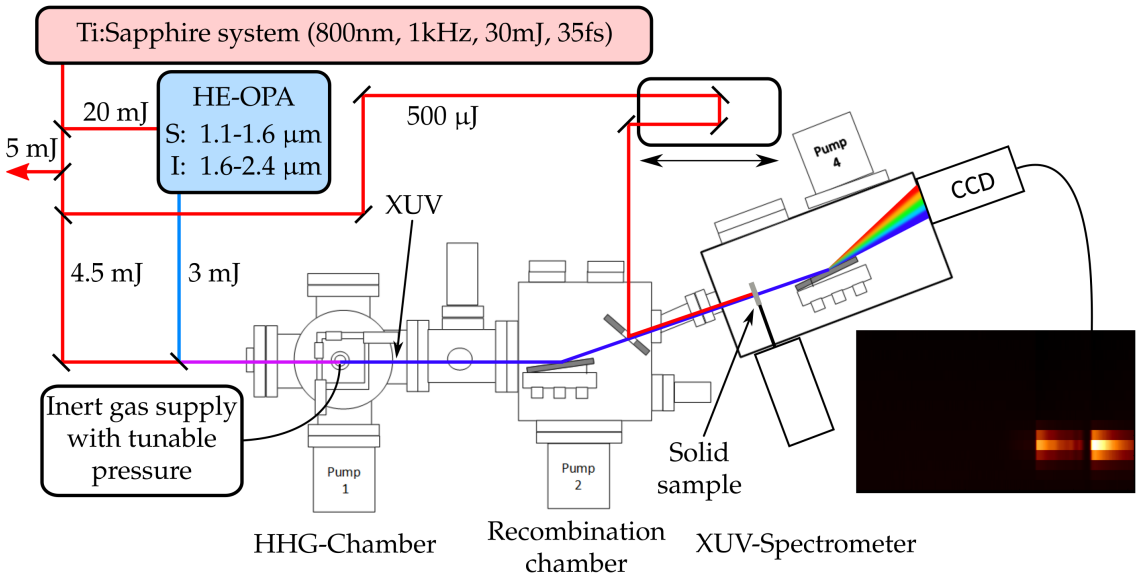

Figure 3.1: Schematic of the experimental setup. The output of the Ti:sapphire laser is used to drive an OPA, which produces mid-IR radiation at 1.4 µm, which is overlapped in time and space with the original 800 nm radiation in a gas cell, filled with a noble gas. This leads to the generation of continuous HHG radiation, which is collinear to the driving field. The HHG beam is focused onto the sample by a toroidal mirror and after it penetrated the sample dispersed by a grating and recorded on a CCD camera. The sample is pumped by a fraction of the 800 nm beam, whose delay can be tuned with a delay stage. In this arm 500 µJ are available, in the experiment in this thesis only pump pulse energies of few µJ were typically used. The pump power was reduced with a $\lambda/2$ plate and a polarizing optic, which for simplicity are not shown in this figure.

of a Ti:sapphire oscillator, which delivers 400 mW at 80 MHz repetition rate. After the oscillator the pulse is chirped and sent into an regenerative amplifier, which reduces the repetition rate to 1 kHz. After sufficient round trips in the regenerative amplifier the pulse energy is amplified to 3 mJ. All Ti:sapphire crystals are cooled by a gaseous Helium cooling system to reduce thermal lensing, as the thermal conductivity of sapphire increases at lower temperatures. The still heavily chirped pulse is then sent through two multi-pass amplifiers, which increase the mean power to 40 W. The chirp of the pulse is removed in the compressor, which yields pulses with 30 mJ pulse energy and 35 fs pulse duration. A major problem with such high power lasers, which we also encountered is thermal lensing in windows, as a consequence of optical degradation of the window material. This especially happens in the windows of the vacuum chambers, as these are relatively close to the focal point in the Ti:sapphire crystals and so the beam is still small and the intensity is high. This problem could eventually be solved by using sapphire as window material instead of fused silica.

Optical parametric amplifiers (OPA) have found widespread use from UV to infrared spectroscopy to fundamental quantum research. OPAs are devices that use the $\chi^{(2)}$ nonlinear polarization in nonlinear crystals to convert a high frequency wave into two low frequency waves, or in a photon picture to split a high energy photon into two low energy photons. The generated frequencies are connected by the so called energy conservation

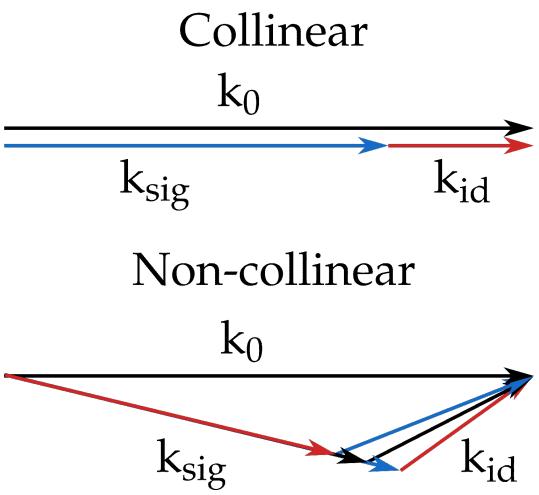

Figure 3.2: Sketch of the two phase matching setups in an OPA. At the top is the collinear setup, where all k vectors are parallel and phase matching is achieved solely with their magnitude, i.e. by adjusting the refractive index. At the bottom is the non-collinear setup, where phase matching is achieved by vectorial addition of the k vectors. As a result the k vectors of different frequencies within one beam, here depicted the idler, are not collinear anymore.

condition

$$\omega_0 - \omega_{sig} - \omega_{id} = 0,$$

In order to effectively generate light, phase matching must be satisfied as well

$$\mathbf{k}_0 - \mathbf{k}_{sig} - \mathbf{k}_{id} = 0, \tag{3.1}$$

where index 0, sig, id represent the pump, signal and idler respectively. This condition is often called momentum conservation in connection with the photon picture. Two basic geometries for an OPA are possible. Firstly the collinear geometry, where $\mathbf{k}_0 \parallel \mathbf{k}_{sig} \parallel \mathbf{k}_{id}$. In this case an effective choice of polarization geometry, nonlinear crystal and crystal orientation is necessary to fulfill Eq. (3.1), as now the refractive index is the only free parameter. Eq. (3.1) can then be rewritten to

$$n(\omega_0)\omega_0 - n(\omega_{sig})\omega_{sig} - n(\omega_{id})\omega_{id} = 0$$

For the polarization one can choose $\mathbf{E}_{sig} \parallel \mathbf{E}_{sig} \perp \mathbf{E}_0$, called type I phase matching or in type II phase matching either $\mathbf{E}_{id} \parallel \mathbf{E}_0 \perp \mathbf{E}_{sig}$ or $\mathbf{E}_{sig} \parallel \mathbf{E}_0 \perp \mathbf{E}_{id}$. Type II phase matching offers a larger phase matching bandwidth and is therefore preferred for ultrashort pulses. Secondly the non-collinear geometry, where the beams are not collinear and the vector character of Eq. (3.1) can be exploited. The non-collinear setup offers a higher phase matching bandwidth. The disadvantage is that one of the generated beams, signal or idler, obtains an angular chirp. The angular chirp, which is a dependence of the direction of the emitted light upon the frequency, is caused by the geometric satisfaction of the phase matching condition (see Fig. 3.2). The beam with the angular chirp is effectively unusable and so it is typically dumped.

The difference frequency mixing process needs two different waves to begin with. Often super continuum generation in a thin, e.g. sapphire plate, is used to generate all frequencies in the desired range for the signal, which can then be used to seed the process. As long as the pump intensity is much higher than of the idler or signal, the amplification of signal and idler is essentially exponential.

In the experiment we used a commercially available OPA (LIGHT CONVERSION HE-TOPAS), which is tunable between 1.16 µm to 1.6 µm for the signal and 1.6 µm to 2.6 µm for the idler and offers a conversion efficiency around 30%. We split 20 W from the Ti:sapphire laser to serve as pump in the OPA. In the OPA the pump is split four fold. A sub-µJ fraction is used for supercontiunuum generation in a thin sapphire plate. The super continuum is overlapped in time and space with another fraction of the pump in the first difference frequency mixing crystal to generate signal and idler. The OPCPA uses Barium borate (BBO, formula $Ba(BO_2)_2$) for all frequency mixing stages. The frequencies that are produced are determined by the orientation of the BBO, i.e. phase matching, and the delay between super continuum and pump as the super continuum pulses are heavily chirped. Both parameters can be adjusted in order to pick the desired frequency for signal and idler. The signal is send to the second and third nonlinear crystal to be amplified, while the idler generated in the first and second crystal is dumped. The total output power, i.e. signal plus idler reaches $\approx 6\,\mathrm{W}$ after the third and last nonlinear crystal. The power between signal and idler is split according to

$$I_{sig} = I_{total}\frac{\omega_{sig}}{\omega_0} \qquad I_{id} = I_{total}\frac{\omega_{id}}{\omega_0} \qquad I_{total} = I_{sig} + I_{id}$$

After the OPA signal and idler are separated by a dichroic mirror. In the experiments in this thesis the signal with wavelength of 1.4 µm and 3.5 W power were used.

3.3 Generation of Ultrashort XUV Pulses with High-Harmonic-Generation

High-harmonic generation (HHG) is an optical non linear process, that converts light with a fundamental frequency ω_0 to light of a high multiple $n\omega_0$ ($n > 10$) of the fundamental. Under non-resonant condition every order of non-linear polarization $\mathbf{P}^{(n)} \propto \mathbf{E}^n$ becomes smaller by a factor $\sim E/E_{at}$, where E_{at} is the characteristic atomic field of the material[2], i.e. higher harmonics become weaker by their order and the lowest orders dominate the whole optical response and can be realistically used for frequency conversion. In the late 1980s [MGJ+87] it was discovered that noble gases upon irradiation by high intensity ($I > 10^{14}\ \mathrm{W\,cm^{-2}}$) ultra short pulses emit very high harmonics up to the 21st order [FLL+88]. These first experiments already outlined the typical spectral shape of HHG. Only odd harmonics are visible as well defined peaks and the intensity decreases

[2] For simplicity the characteristic atomic field is often taken to be the Coulomb field of the hydrogen at one Bohr radius distance, which yields $E_{at} \approx 0.51\,\mathrm{kV\,nm^{-1}}$.

for the first few orders but for $n \gtrsim 5$ reaches a plateau of almost constant intensity up to a sharp cutoff.

The general physics of the process was soon understood and theoretical models that could reproduce the general shape of the experimental spectra were developed. Corkum published the so called three step model in 1993 [Cor93] that despite its extreme simplicity captures the most important features . The three step model divides HHG into three separate processes, namely ionization, acceleration in the vacuum and recombination. In the first step the bound electron tunnels through the Coulomb barrier, which is distorted by the linear external potential. In his original paper Corkum uses a semi classical (WKB) tunneling model but other methods such as direct solutions to the time-dependent Schroedinger equation (TDSE) are possible as well. After the ionization a classical treatment of the electron is used and the electron is assumed to be at the atomic position with zero velocity directly after ionization. The coulomb interaction is neglected in this step. This leads to the extremely simple equation of motion

$$\ddot{\mathbf{r}}_e = -\frac{e}{m_e}\mathbf{E}_0 \cos(\omega_0(t - t_0))$$

which can be solved analytically. The maximum kinetic energy the electron can extract from the external field is

$$E_{\text{kin,max}} = 3.17 U_p \qquad\qquad U_p = \frac{e^2 E_0^2}{4 m_e \omega_0^2}$$

with the ponderomotive potential U_p. The extracted kinetic energy depends on the phase of the field with respect to the point in time of ionization and is optimal around $\frac{1}{6}\pi$. Smaller phases lead to a shorter excursion time and distance and higher phases to longer excursion time and distance, both however with smaller kinetic energy. These two types of trajectories are often simply labeled short and long trajectories. The last step, recombination, occurs when the electron returns to the nucleus. Due to the high kinetic energy of the electron this occurs on an attosecond timescale and the process emits an attosecond pulse, which is extremely broad and continuous in frequency space. The process with the maximal emitted photon energy is when the electron recombines with the ion. Then it emits the ionization potential I_p in addition to the kinetic energy, so the cutoff is

$$E_{\text{cutoff}} = 3.17 U_p + I_p$$

More advanced models solve the time-dependent Schroedinger equation (TDSE), typically in the dipole approximation with

$$i\hbar \partial_t |\psi\rangle = \left(\frac{p^2}{2m} + V(r) - e\mathbf{E}\mathbf{r} \right) |\psi\rangle$$

within various levels of approximation such as the strong field approximation (SFA). The emitted harmonics calculated with the transient dipole

$$d(t) = -\langle \psi | e\mathbf{r} | \psi \rangle$$

and the HHG spectrum $S(\omega)$ as

$$S(\omega) \propto |d(\omega)|^2$$

So to recap the general physics of HHG. An electron is extracted from its atom by strong field ionization and accelerated by the field into the vacuum. After the field switches sign it is accelerated back into its atom, where it arrives with a kinetic energy gain, which depends on the phase of the field at extraction. These excess kinetic energy is emitted as light and is responsible for HHG. The emitted spectrum of a single cycle is continuous.

In a multi period driving pulse the interference between HHG from different half periods gives rise to the peaks at uneven harmonics. If $E_s(t)$ is the field from a single half cycle and A_n is its amplitude, the full field is given by

$$\begin{aligned} E_{tot}(t) &= \sum_{n=-\infty}^{n=\infty} (-1)^n E_s(t - n\frac{\lambda}{2c}) A_n \\ E_{tot}(\omega) &= \sum_{n=-\infty}^{n=\infty} (-1)^n A_n E_s(\omega) e^{-i\omega n \frac{\lambda}{2c}} \\ &= E_s(\omega) \underbrace{\sum_{n=-\infty}^{n=\infty} A_n (-1)^n e^{-i\omega n \frac{\lambda}{2c}}}_{=f(\omega)} \\ S(\omega) &\propto |E_s(\omega)|^2 \cdot |f(\omega)|^2 \end{aligned} \tag{3.2}$$

The half cycle spectrum $|E_s(\omega)|^2$, which would be continuous is modulated by a $|f(\omega)|^2$ due to interference between the half cycles. The $(-1)^n$ factor leads to constructive interference only between odd harmonics. For a simple rectangular intensity profile $A_n = \{1 \text{ for } 0 < n \leqslant N,\ 0 \text{ else}$ one can solve the sum analytically and find

$$|f(\omega)|^2 = \frac{\sin^2((N+1)x)}{\sin^2 x} \qquad\qquad x = \pi\left(\frac{\omega}{\omega_0} - \frac{1}{2}\right)$$

which peaks at odd harmonics and the peaks show a spectral width $\Gamma \propto 1/N$, i.e. the shorter the driving pulse is in time the broader the HHG peaks become. A more realistic HHG spectrum with an Gaussian intensity profile is shown in Fig. 3.3. The qualitative behavior is however quite similar. A single atom principally emits into the full solid angle with a dipole angular dependence. Experimentally we observe an exclusive emission into forward direction. The reason is that for a macroscopic gas cell a coherent emission is necessary in order to effectively radiate light. This condition is called phase matching and quantitatively the coherence length

$$L_{coh} = \frac{\pi}{|\Delta \mathbf{k}|}$$

must be larger than the gas cell. $\Delta\mathbf{k}$ is the wave vector mismatch between laser light and the respective HHG mode of order γ as

$$\Delta \mathbf{k} = \mathbf{k}_{hhg} - \gamma \mathbf{k}_l$$

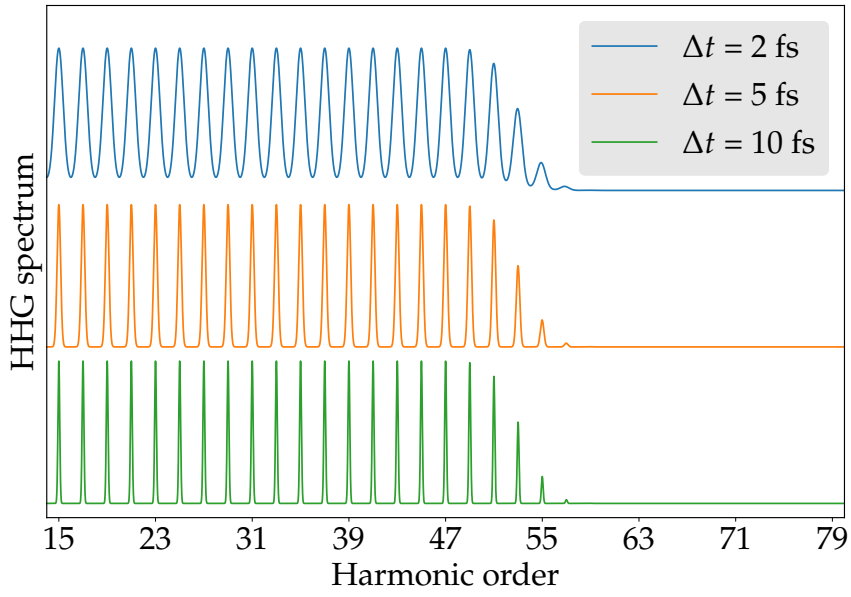

Figure 3.3: Sketch of the qualitative behavior of a HHG spectrum with a Gaussian envelope (for A_n), calculated with Eq. (3.2). For a higher time duration of the envelope the peaks become successively sharper. Note that the time duration of the envelope is functionally related but not equal to the time duration of the driving pulse due to the non linear nature of the HHG process.

The direction of the HHG's k vector $\mathbf{k}_{hhg}$ is in principle free and emission occurs in those directions were L_{coh} is smaller than the gas cell length. The phase matching condition can only be strictly zero in forward direction. If we assume that it is fulfilled in forward direction, i.e. $\mathbf{k}_{hhg} = \gamma \mathbf{k}_l$, we find that for a small angular mismatch ϑ

$$|\Delta k| \approx \vartheta\gamma|\mathbf{k}_l| \approx \vartheta\gamma\frac{2\pi}{\lambda_l}$$

The phase matching condition for the angle now reads

$$L_{coh} = \frac{\pi}{|\Delta \mathbf{k}|} = \frac{\lambda_l}{2\gamma\vartheta} > L_{cell}$$
$$\vartheta < \frac{\lambda_l}{2\gamma L_{cell}}$$

We see that the higher the harmonic order and the longer the gas cell, the smaller the cone of emission. For a typical configuration with a Ti:Sapphire laser around 800 nm and a 5 mm gas cell the maximum angle of emission for the 30^{th} harmonic is $1.5 \times 10^{-4\circ}$, which means that the HHG beam has basically the same divergence as the original beam.

In forward direction the phase matching condition can be expanded as

$$\delta k = \frac{\omega_{hhg}}{c}\Delta n_{at} + \frac{\omega_{hhg}}{c}\Delta n_{el} + k_{geo} + k_{dip} \tag{3.3}$$

with the contributions

atomic refractive index $\Delta n_{at} = n(\omega_{hhg}) - n(\omega_l)$

plasma refractive index $\Delta n_{pl} = n_{pl}(\omega_{hhg}) - n_{pl}(\omega_l)$

$$n_{pl} = \sqrt{1 - \frac{\omega_{pl}^2}{\omega^2}} \approx 1 - \frac{\omega_{pl}^2}{2\omega^2} \text{ with the plasma frequency } \omega_{pl} = \sqrt{\frac{\rho_{pl} e^2}{\varepsilon_0 m_e}}$$

Gouy phase $\frac{\omega_{hhg}}{\omega_l} \partial_z \arctan \frac{z}{z_r} = \frac{\omega_{hhg}}{\omega_l} \frac{1}{z_r} \left(1 + \frac{z^2}{z_r^2}\right)^{-1}$

dipole phase shift $k_{dip} = \alpha \partial_z I(z)$

Δn_{at} is the difference refractive index of the neutral gas between hhg and fundamental frequency. The plasma refractive index contribution Δn_{pl} is caused by ionized part of the neutral gas. The high intensity ionizes a fraction of the gas in the cell, which has a qualitatively and quantitatively different refractive index. The last two terms are the Gouy phase, which is a consequence of the focusing geometry, which is used in most experiments, and the nonlinear dipole phase, which occurs because the emission phase from the three step HHG process depends on the intensity.

Experimentally the gas pressure, intensity of the beam and focus position in relation to the cell can be changed in order to achieve phase matching, therefore the dependence of each term on these parameters is important. For phase matching, i.e. $\delta k = 0$ a set of conditions has to be found so that all terms cancel each other out. One can typically distinguish two regimes. For relatively low energy harmonics $E < 100$ eV, low pressure $p < 100$ mbar, relatively small pulse energy and a short focus geometry the last terms dominate and can be tuned to cancel each other out. The geometric (Gouy) phase is always positive so the nonlinear phase must be negative, which implies decreasing intensity, i.e. the cell must be behind the focus.

The other extreme case is a relatively high pressure, high pulse energy and long focus geometry, where the first two terms dominate. The first term is always negative because the refractive index at the hhg frequency is very close to one and can be approximated by

$$\Delta n_{at} \approx 1 - n(\omega_l) = \chi_{at} \rho_{at}$$

where χ_{at} is the susceptibility per density and ρ_{at} is the density of the gas. The plasma contribution is always positive and can be approximated by

$$\Delta n_{pl} = \frac{\omega_{pl}^2}{2\omega_l^2} = \frac{\rho_{pl} e^2}{2\varepsilon_0 m_e \omega_l^2}$$

Phase matching can only be achieved if a non negligible fraction γ_{pl} of the gas is ionized and the plasma density $\rho_{pl} = \gamma_{pl} \rho_{at}$ if sufficiently high. The fraction γ_{pl} for which phase matching is achieved is given by

$$\begin{aligned} \gamma_{pl} &= \frac{2\varepsilon_0 m_e \chi_{at} \omega_l^2}{e^2} \\ &\approx 0.04 \quad \text{for } \lambda = 800 \text{ nm and argon gas} \end{aligned}$$

If we include the Gouy phase for our experimental conditions the ionization radio reduces to $\gamma_{pl} \approx 0.02$ as the positive contribution of the Gouy phase adds to the positive contribution of the plasma refractive index.

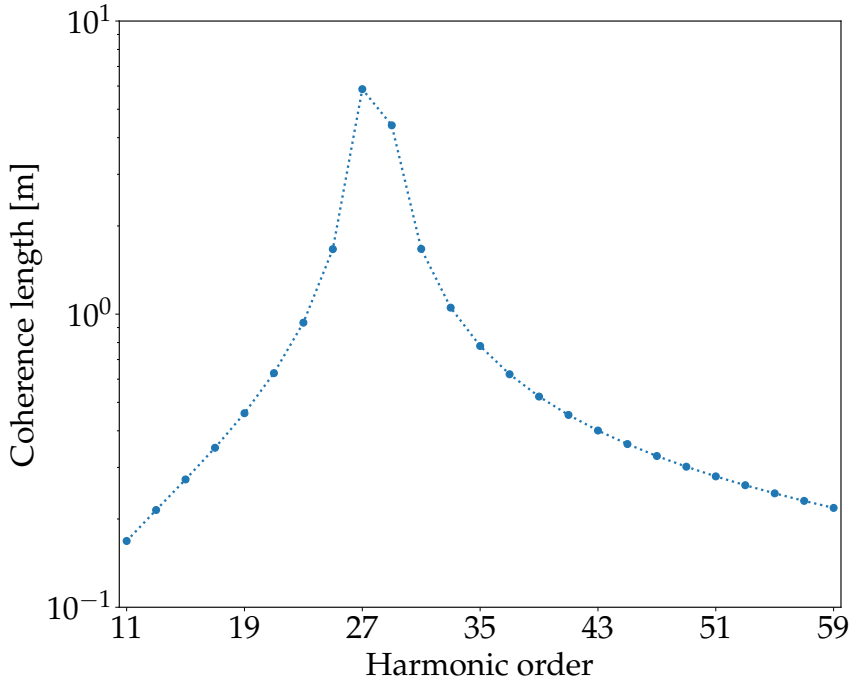

Figure 3.4: Simulated coherence length of a phase matched HHG source according to Eq. (3.3). Phase matching is achieved around the 27^{th} harmonic. The plasma dispersion, which is the only frequency dependent term, is sufficiently low so that for the full range the coherence length is larger than 0.1 m, i.e. phase matching is achieved.

3.4 XUV Detection Setup

An XUV spectrometer is a device that is able to measure the spectrum of an XUV light source by dispersing its wavelength and subsequent detection of the light. For XUV and soft x-rays these two steps are separated into two subdevices, while for hard x-ray it is possible to perform both steps with one device. The requirements of an XUV spectrometer, are relatively difficult to entirely fulfill without compromise due to the lack of optical devices in the XUV range and necessity to operate the device in vacuum due to the strong absorption of air in this wavelength range. The parameters of an XUV spectrometer are:

Quantum efficiency The quantum efficiency is the ratio of detected and incoming photons. It is determined by the reflectivity/transmittivity of the involved optical elements and the intrinsic quantum efficiency of the detector.

Spectral resolution

Spectral range

There are two main approaches to disperse by wavelength. In high-flux facilities such as synchrotrons or free electron lasers and in the hard x-ray range monochromators are often used. Monochromators only transmit a well defined wavelength of the light source, whereas all the other radiation is discarded. This wavelength can be tuned, which allows for scanning over the desired wavelength range.

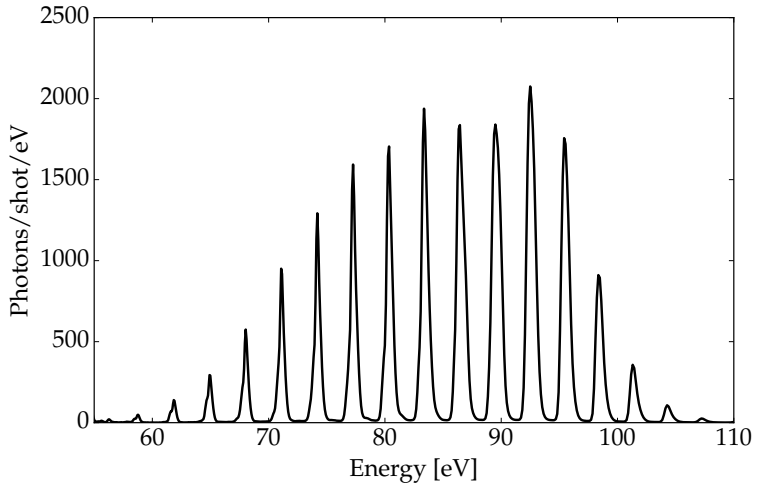

Figure 3.5: Single color HHG spectrum of our XUV source with Neon gas as target and a zirconium filter.

The other approach is to disperse the light spatially and to detect the different frequencies on a detector with spatial resolution. In the XUV range typically a grating is used to disperse the light. The spectral resolution now depends both on the dispersive element and on the spatial resolution of the detector. A full spectrum can be obtained simultaneously with this configuration.

The flux from HHG sources is relatively low and measurement time is crucial so we employed the latter scheme. A schematic of the XUV spectrometer used for this thesis can be found in Fig. 3.1. All of its elements are in a vacuum chamber that can reach a vacuum of p $\sim 10^{-7}$ mbar with a turbo pump. At 10^{-7} mbar XUV absorption of air is negligible. The XUV beam is focused into the sample externally by a toroidal mirror. After the sample the light passes a thin metal foil, which is in a motorized filter wheel. The metal foil together with its framing metal shield prevent optical frequencies from the pump beam or the XUV generation to pass to the detector, which is also highly sensitive to optical light. We used aluminum and zirconium foils with 100 nm thickness. Aluminum is transparent up to its L-edge of ~ 72.6 eV and Zirconium up to its M-edges at ~ 178 eV but with lower transmittivity at low energies due to its N-edge. Both Aluminum and Zirconium form oxide layers, which reduces their transmittivity. Aluminum forms a passivation layer of roughly 4 nm upon oxidation stops. In Fig. 3.6 typical transmittivity of the metal filters is shown. After passing the metal foil the light is dispersed by a concave blaze grating and detected on a CCD camera. The grating is a Hitachi aberration corrected concave blaze grating (Model Nr. Hitachi 001-0437*1,2). Its technical parameters can be found in Tab. 3.1 The surface of the grating is curved in the plane of the light so that it acts as a focusing and dispersive device at the same time. The curvature focuses the light in the spectral dimension into the CCD camera. The distance between sample, i.e. focal point and CCD both are two times the focal length of the grating. The grating is build for a grazing incidence geometry with an input angle of 87° to increase reflectivity.

The reflectivity (courtesy to H. Stiel for providing this data) is around 10% for the first

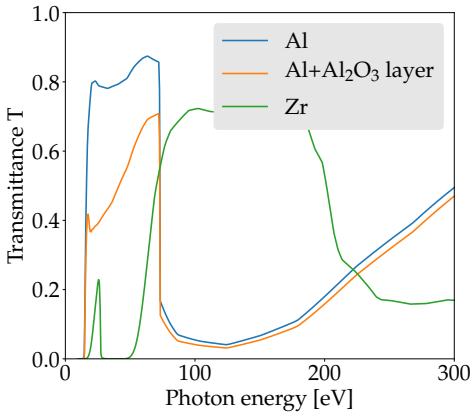

Figure 3.6: Transmittance of 100 nm thin metal foils, which can be used to block visible light in the experiment. Aluminum is used for low XUV energies between 40 eV and 72 eV and Zirconium for the high energy region up to 200 eV. Aluminum forms an aluminum oxide (Al_2O_3) layer of maximally 4 nm on both sides. The transmittance of an oxidized foil is shown in orange.

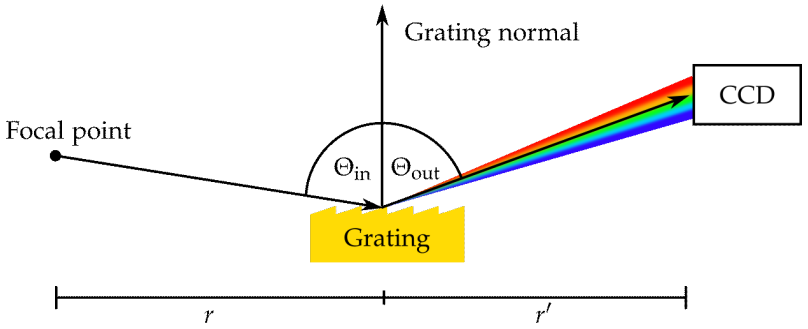

Figure 3.7: Schematic of the blaze grating geometry. XUV light is focused externally into the focal point and afterwards hits the grating under an angle of $\Theta_{in} = 87°$. The output angle depends now according to Eq. (3.4) on the wavelength, i.e. photon energy, so that on the CCD detector the different photon energies are spatially separated

order and between 1% and 10% for the second order (see Fig. 3.8). In the experiment the second order poses a problem as it overlays the first order at half the energy. Therefore only an octave of photon energies can be measured without distortion. In the experiment one has to make sure that no radiation at twice the photon energy region of interest is reaching the detector. In the experiment this was taken care of by the aluminum foil that effectively blocks light above 72 eV. The relatively high reflectivity is achieved, in addition to the grazing incidence, by blazing the grating. The grating's surface consists of a saw-tooth like structure as shown in Fig. 3.7. The periodicity of the saw-tooths determines the grating constant and consequently the dispersion of the XUV light, i.e. the output angle for a given photon energy. This leaves the blaze angle, which is the opening angle of the saw-tooth, as a free parameter and it can be chosen to optimize the reflectivity of the first order. The blaze wavelength is the wavelength of XUV light where direct reflection with regard to the blaze surface is achieved. As a result the reflectivity of the first order is increased and reduced the other orders, especially the zeroth.

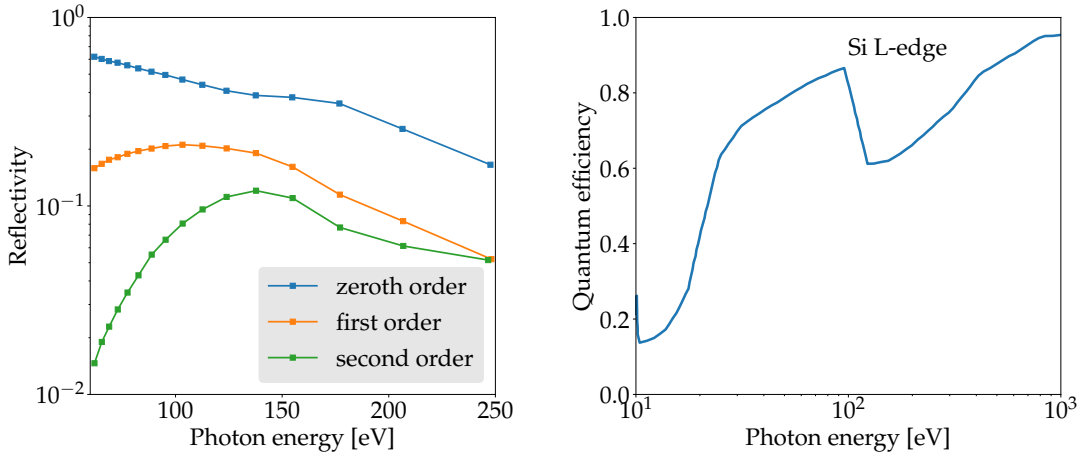

Figure 3.8: (Left) Reflectivity of the Hitachi grating, which was used in the experiments, as a function of photon energy. The first order is measured by the CCD camera and its reflectivity contributes to the total quantum efficiency of the detection setup. The first order reflectivity is between 16 and 20% in the broad energy region of interest of 60-150 eV. For the second order twice the photon energy of interest matters, as the second order appears at twice the angle. At for example 60 eV the the discrimination of the second order is only $R_1(60\,eV)/R_2(120\,eV) \approx 15\%/10\% \approx 0.7$, which means that one has to block light at twice the photon energy beforehand as the discrimination of the grating does not suffice. Courtesy to Holger Stiel for this data. **(Right)** Quantum efficiency of the GREATEYES GE 1024 256 BI UV1 CCD camera, used in the experiment, as reported by the manufacturer. The quantum efficiency is above 60% in the spectral region of interest and is therefore only a minor factor in the overall efficiency of the detection setup. The CCD chip is made from silicon and at the silicon L edge the extremely short penetration depth leads to a decrease in efficiency.

The relation between photon energy and position on the camera, i.e. pixel index, needs to be determined and calibrated on order to obtain meaningful spectra. The standard grating equation is

$$m\lambda = \frac{\sin\Theta_{in} - \sin\Theta_{out}}{g} \tag{3.4}$$

where m is the refraction order, g is the grating constant and Θ_{in}, Θ_{out}, r and r' are illustrated in Fig. 3.7. The relation between output angle and position on the detector

$$\tan\Theta_{out} = \frac{r'}{x}$$

g	Curvature	Θ_{blaze}	λ_{blaze}	Θ_{in}	r	r'
$1200\,mm^{-1}$	5649 mm	3.2°	10 nm	87°	273 mm	235 mm

Table 3.1: Technical parameters of the grating used in the experiments. g is the grating constant, Θ_{blaze} is the blaze angle, which is the the opening angle of the saw tooth like blaze structure, λ_{blaze} is the blaze wavelength, i.e. the wavelength of ideal reflection. Θ_{in}, r, r' are illustrated in Fig. 3.7

can be inserted into Eq. (3.4), which yields

$$\lambda(x) = \frac{\sin\Theta_{in} - \left(1 + \left(\frac{x}{r'}\right)^2\right)^{-1/2}}{gm}$$

or in photon energy

$$E_\gamma(x) = \frac{hc \cdot mg}{\sin\Theta_{in} - \left(1 + \left(\frac{x}{r'}\right)^2\right)^{-1/2}} \tag{3.5}$$

with c the speed of light and h Planck's constant. The trigonometric relation $\sin\arctan x = \frac{1}{\sqrt{1+x^{-2}}}$ was used. In a practical calibration the position x has to be replaced by $x = (n_p + n_0)d_p$, where d_p is the pixel width, n_p the pixel index and n_0 an offset. The spectral calibration can be acquired with a HHG spectrum with the known energy difference between the peaks of $\Delta E = 2\hbar\omega_0$, ω_0 being the center frequency of the driving laser. The absolute scale can be determined by well known edges, such as the Aluminum and silicon L-edges. In Eq. (3.5) all parameters except for n_0 are known with a relatively high accuracy. However to allow for a small correction in all those parameters the grating constant g was also considered as a free parameter. A fit (see Fig. 3.9) of Eq. (3.5) to a calibration measurement yielded

$$g = 1207(6)\,\mathrm{mm}^{-1}$$
$$n_0 = 1265(5)\ \text{pixel},$$

which is in good agreement to the manufacturer's value of $g = 1200$. Exemplary spectra that can be used to extract reference energies can be seen in Fig. 3.10. The continuous two-color spectrum (top left) can be used to extract the exact edge-position and the single-color spectrum (top right) can be used to extract the relative energy spacing.

In the XUV region there are two types of detectors. Detectors that directly detect the XUV light, e.g. with a light active semiconductor layer or detectors that first convert XUV into optical light, which can be detected with a standard optical camera.

Examples of the first kind are CCD and CMOS detectors. CCD detectors offer the highest quantum efficiency in the XUV range together with good readout rate and spatial resolution. CMOS detectors are similar to CCD detectors but offer a higher readout rate at the prize of a reduced quantum efficiency. An example of the second kind are Micro channel plates (MCP). An MCP is an array of micro structured electron multiplier tubes, which is typically used together with a phosphorus screen,where the accelerated electrons produce visible light. MCPs offer significantly lower quantum efficiency of $\sim 10\%$ and higher noise due to the nonlinear amplification process. They are however insensitive to optical light and can be used to detect electrons and ions as well.

In the experiments we used an back-illuminated charge-coupled device (CCD) from GREATEYES (Model GE 1024 256 UV1) with 1024×265 pixels and a pixel size of $26\,\mu m \times 26\,\mu m$. A back-illuminated CCD is specifically designed for a high quantum efficiency in the XUV region. In front-illuminated CCDs the incoming light has to penetrate electrodes

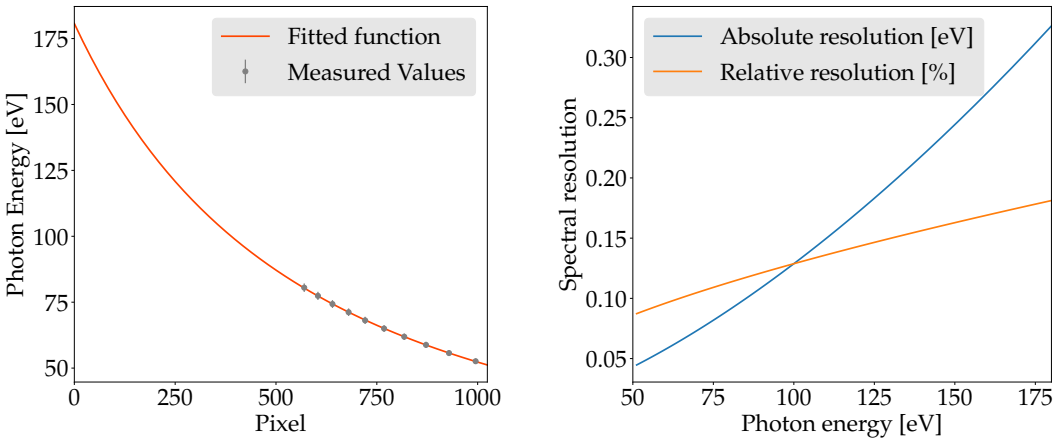

Figure 3.9: Spectral properties of the camera. Left: Fit of measured high harmonic peaks to Eq. (3.5). The fit yielded $g = 1207(6)\,\mathrm{mm}^{-1}$ and $n_0 = 1265(5)$. Right: Pixel-limited spectral resolution of the camera according to Eq. (3.6). Blue is the absolute spectral resolution in eV and yellow the relative resolution, i.e. $\delta E/E$

and an oxide junction, which both are typically transparent for visible light. In the XUV region both are not transparent, which significantly lowers the quantum efficiency. In a back illuminated CCD the back of the CCD is thinned in an etching process, so that light from the back can reach the active silicon layer.

The pixel limited spectral resolution is given by

$$\delta E = \partial_x E_\gamma(x) d_p = E_\gamma(x) \frac{x d_p}{r'^2 \left(\sin\Theta_{in} - \left(1 + \left(\frac{x}{r'}\right)^2\right)^{-1/2} \right) \left(1 + \left(\frac{x}{r'}\right)^2\right)^{3/2}} \tag{3.6}$$

and plotted in Fig. 3.9. The resolution is not constant over the spectrum as its dependence is non-linear. It reaches from ~50 meV at 50 eV (1/1000) to ~300 meV at 180 eV (1/600). This is the lower bound for the resolution. Other factors that limit the resolution are the quality of the grating, the imaging of the focal point and the initial size of the focal point. The initial size of the focal point depends on the alignment of the toroidal mirror in the recombination chamber, while the imaging depends on the alignment of the grating. The actual resolution was estimated as $\delta E(60\,\mathrm{eV}) \leqslant 150\,\mathrm{meV}$ from a HHG spectrum generated by a strongly chirped driving pulse, which leads to sharper HHG peaks. The bandwidth of the peak was probably still intrinsic and not limited by the detector's resolution.

The readout rate of the camera is maximally 3 MHz per pixel, which means 90 ms readout time for a full image. The readout time can be reduced by vertical binning. In the experiment typically a 16-fold vertical binning and readout rate of 1.5 MHz was used, which leads to a readout time of 10 ms. The electronic noise of the camera has two components. In every pixel thermal excitation of electron hole pairs is possible, which is called dark current. The camera can be cooled to reduce this effect. The other contribution is readout noise from the ad converter, which depends on the readout rate. In our experiments the shot-to-shot fluctuations of the HHG is the dominate source of the noise.

3.5 Stability of the XUV Source

In pump probe spectroscopy the noise of the overall experiment determines the smallest non-linear signal one is able to measure with for a given duration of the entire experimental scan. As the experimental error only decreases with the one over the square root of the acquisition time, it quickly becomes unfeasible to further reduce the error significantly, for instance if one arrives at a given noise level after one day of experiment time it would take almost a third of a year to reduce the noise level by another order of magnitude. This illustrates the importance to directly design the experiment such that the noise is reduced in the first place. In laser driven pump probe experiments there are three main sources of noise, which are photon shot noise, detection noise and source instability.

Shot noise originates from the fundamental quantum nature of light in the detection process. A detector can either detect a photon or not. Thus, even for a light source with constant intensity (e.g. coherent laser radiation) one gets in a certain time interval a discrete number of detected photons, hence the name shot noise. The measured number of photons exhibits stochastic fluctuations and its standard deviation is given by

$$\delta N = \sqrt{N} \qquad \frac{\delta N}{N} = \frac{1}{\sqrt{N}}$$

The relative error decreases as one over the square root of the photon number, which is proportional to the intensity. The shot noise can basically [1] only be reduced by increasing the photon flux of the probe or the quantum efficiency of the detector, i.e. by increasing the number of detected photons. If neither can be readily improved, which is unfortunately often the case, the limit of the experiment with regard to the shot noise is reached. Typical "standard" light sources such as thermal and coherent light sources exhibit a Poisson photon statistics.

Detector noise is quite specific to the kind of detector in use. In the case of a CCD the main components are thermal noise caused by thermal excitation of electron hole pairs, which is proportional to the acquisition time and readout noise, which is caused by electronic noise in the analog digital converter and occurs once per acquisition. Both detector contributions are negligible in our case.

The dominant noise in our experiment originates from the instability of the HHG source, i.e. fluctuations in the intensity between consecutive probe pulses. In a pump-probe experiment we want to compare the transmitted intensity of the pumped and unpumped sample, i.e. measure $\Delta I = I_p - I_{up}$ or the relative change $^{\Delta I}/_{I}$. In our experiment it was not possible to record a pumped and unpumped spectrum with originally the same probe pulse, e.g. by splitting off half of the probe and sending it through an unpumped region

[1] It is often stated that the shot noise in the $^{1}/\sqrt{N}$ sense is the ultimate limit, which is not true. In the LIGO experiment, which detected gravitational waves [LIG16] to win the Nobel prize, special optical parametric oscillator (OPO) based light sources were used, that emit squeezed states to decrease the noise below the shot noise limit [LIG13]. This significantly reduced the noise level in the frequency region of interest for gravitational wave detection and was crucial for the first detection of gravitational waves in 2016. This highly specialized technique is however not applicable in normal pump probe experiments.

of the sample, which would be the optimal strategy. Instead we measured pumped and unpumped spectra consecutively in time, which is essentially determined by the readout rate of the XUV camera (see Sec. 3.1). If the probe intensity I_0 of one acquisition fluctuates by δI_0 the difference ΔI will fluctuate by

$$\begin{aligned} \delta\Delta I &= \sqrt{2\delta I_0^2 - 2\,\mathrm{Cov}\left[I_p, I_{up}\right]} \\ &= \sqrt{2}\;\delta I_0 \quad \text{for uncorrelated } I_p \text{ and } I_{up} \end{aligned} \tag{3.7}$$

where $\mathrm{Cov}\left[I_p, I_{up}\right]$ is the covariance or correlation between consecutive measurements. An actual time series of the HHG sources used in the experiment can be found in Fig. 3.10. The data were taken with a lithium borohydride sample and active pump beam. It is a small part of the data, from which the time resolved results in Chap. 4 were derived. The spectra at the top show the superior spectral coverage of the two-color HHG source. In the central panel the normalized total, i.e. integrated over the spectrum, flux per shot of the respective sources however shows that the spectral coverage comes at a cost of higher fluctuations of the two-color HHG source. The standard deviation of tc-HHG is with $\sigma_{tc} = 12.6\%$ almost a factor of five larger than that of the sc-HHG with $\sigma_{tc} = 2.6\%$. The noise spectra, i.e. the modulo squared of the Fourier transform of the time series (the bottom panel) show a very similar behavior for both HHG types, with only a displacement by a constant factor of $\sigma_{tc}^2/\sigma_{sc}^2$ as significant difference. Both spectra show a significant increase of noise towards low frequencies and a plateau like behavior towards high frequencies, with a convergence of the plateau around 6 Hz. The dashed lines indicate the respective shot noise limit. In our case as we are well beyond the plateau further improvement cannot be gained by faster acquisition.

The reason behind the reduction of noise by fast consecutive measurement of pumped and unpumped frames can be understood with Eq. (3.7). A positive correlation between two summands in a difference such as ΔI reduces its error, while a negative correlation would increase it. In the noise spectrum of a time series positive correlation between consecutive points shows up in the low frequency range, such as in Fig. 3.10, while a negative correlation would show up in the high frequency range. Typically laser driven sources only show positive correlations, which come from low frequency fluctuations such as e.g. air flow or heating effects. Negative correlation would be the tendency to alternate between high and low power pulses for which there is typically no mechanism.

The quick succession of alternating pump and unpumped measurements effectively allows to drop the noise level to the value at the high frequency end of the noise spectrum. All low frequency components are filtered out, which yields a decrease in noise by a factor of ≈ 2.5 for both sources, which means a six fold decrease in measurement time.

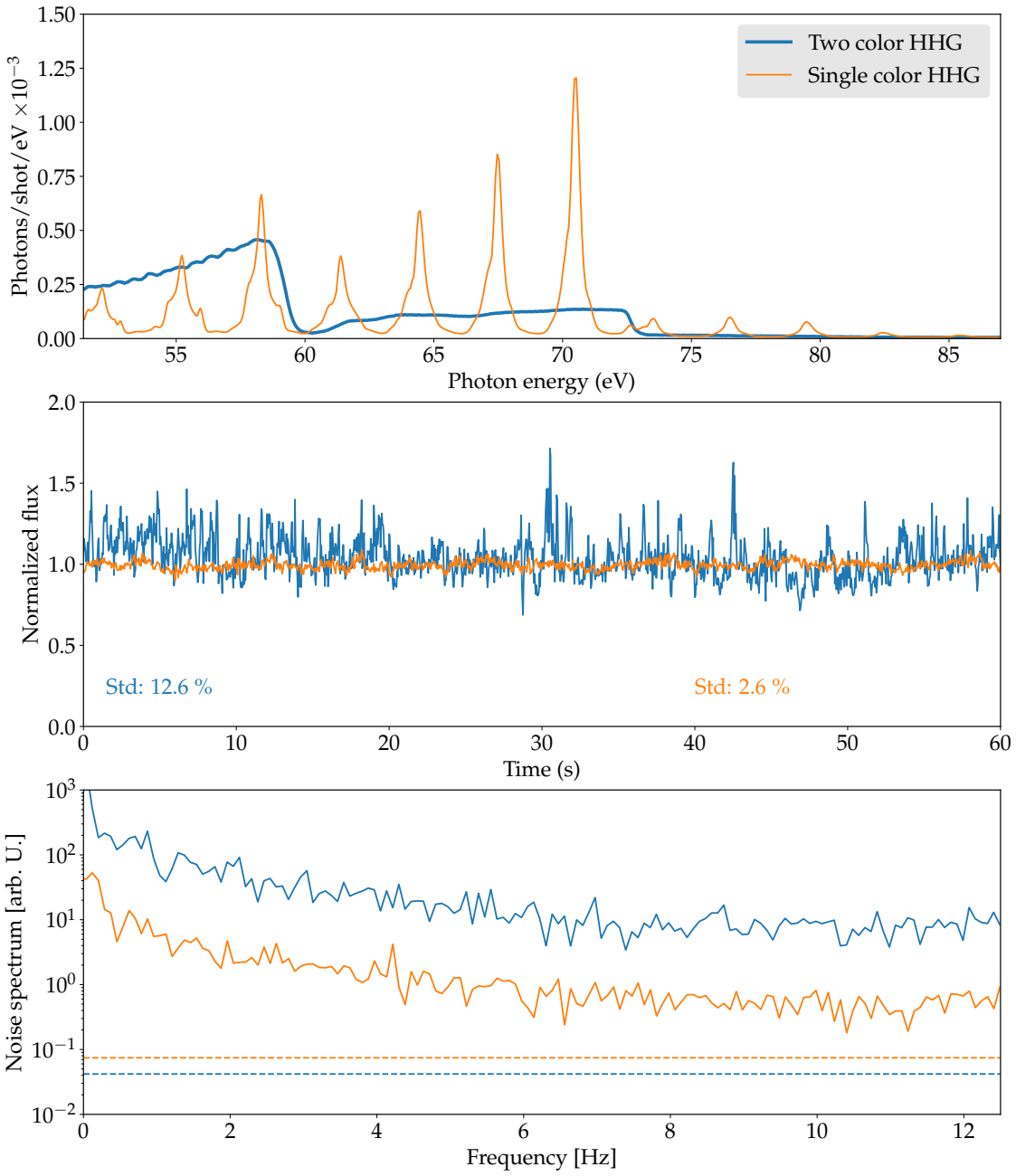

Figure 3.10: (Top) Measured absorption spectrum of lithium borohydride with a single and two-color HHG source. The integrated intensity of both sources is similar. **(Central)** Normalized total flux as a function of time on the detector. The respective total flux is the sum of the spectra shown at the top. sc-HHG shows a much lower fluctuation of total flux with a standard deviation of 2.6% compared to tc-HHG with a standard deviation of 12.6%, roughly a factor 5 larger.**(Bottom)** The noise spectrum, i.e. $|\mathcal{F}(I)|^2$ of the flux of the respective HHG source is drawn as solid line. The dashed lines are the respective shot noise limits. Both source show a very similar noise spectrum, which is just displaced by a factor of $\sigma_{tc}^2/\sigma_{sc}^2$ according to their different noise levels. The similar behavior as a function of frequency indicates a joined source of noise, namely the laser and no additional noise from the OPA itself. The higher noise in the tc-HHG is due to the higher nonlinear dependence of the tc-HHG procedure compared to the sc-HHG procedure.

3.6 Sample preparation

For x-ray absorption spectroscopy in a transmission geometry it is crucial to prepare a relatively thin simple with reasonable surface roughness. The higher the x-ray absorption cross section at the desired edge and especially the background absorption before the edge, the thinner the sample must be prepared. For the range around the Li K-edge of 50 eV-70 eV samples should be in the sub µm down to tens of nm for samples with relatively heavy elements. Lithium borohydride is one of the materials with the highest usable thickness as it only contains very light elements, especially 18 mass % hydrogen, which absorbs very weakly in the XUV, and does not contain too much lithium, which would render the absorption edge too strong. For e.g. lithium hydride with an extremely high lithium mass ratio of 87% a sub 100 nm thickness must be used due to the sharp increase of absorption at the lithium K edge. For compounds containing heavier elements like e.g. α-hematite (Fe_2O_3) [3] a sub 100 nm thickness is necessary to keep the background absorption reasonably low. Very dilute systems, i.e. low concentration of the element under study, are extremely challenging in the XUV region as the background absorption is strong and the contrast between pre and post edge is low in this case. Molecules in aqueous solution for example are currently inaccessible with XUV spectroscopy and can only be measured in the water window or in the few keV region. The water window is defined as the region from ~ 250 eV, where the carbon K edge is located and the absorption of the valence states has sufficiently declined, and the oxygen K edge at ~ 530 eV has not yet set in. Typically such samples are prepared by a typical thin film deposition technique such as chemical vapor deposition (CVD), sputtering or molecular beam epitaxy among others. For relatively thick samples deposition by evaporation of a solution is also possible.

All these techniques rely on a stable substrate that holds the actual layer and can be manipulated. For XAS in the aforementioned region the substrate should be as thin as possible, while still rigid enough to support the sample and withstand the deposition process. Additionally it must not contain elements with absorption edges close to the one(s) under study. For pump-probe spectroscopy it is favorable if the substrate is transparent for the pump beam. This is especially important for samples which are transparent for the pump as then the full pump power reaches the substrate on the bottom. In rare cases the substrate might show transient signals itself, although far away from the edges those are typically very weak. The main factor is however that the substrate might be destroyed or heat up the sample or damage the latter. The most common choice for the substrate are silicon nitride (Si_3N_4) thin films, which are commercially available down to a thickness of ~ 10 nm, with a high transmission of $T \approx 0.9$ @ 60 eV. Often for better stability and larger surface areas somewhat thicker substrates of ~ 50 nm or ~ 100 nm are used with still acceptable transmission of $T \approx 0.4$ @ 60 eV and $T \approx 0.15$ @ 60 eV respectively. The silicon nitride substrates are however relatively small with typically some mm edge length.

We decided to use diamond like carbon (DLC) as an alternative. DLC is an amorphous material made from pure carbon with a mixture of sp^3 and sp^2 bonding, i.e. chemical

[3] Here the iron M edge lies in the XUV region around ~ 50 eV, see e.g. [VWJL+13] , who used a 14 nm layer Fe_2O_3 on a 100 nm silicon nitride substrate

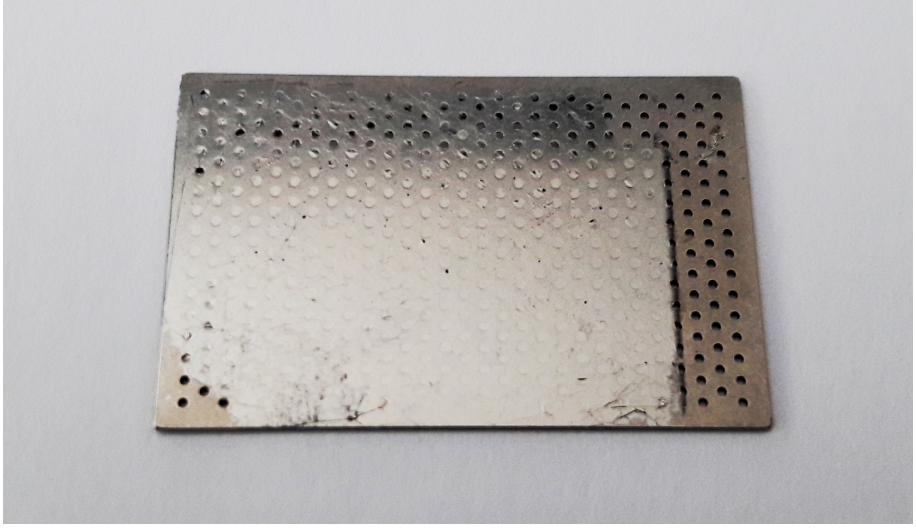

Figure 3.11: Metal support with 50 nm diamond like carbon (DLC) membrane as substrate. The dimensions of the support are 40 mm × 25 mm, which are almost completely covered by the DLC membrane.

bonding between diamond and graphite. Its main advantages over silicon nitride are that it is less brittle and can be produced and bought as few cm^2 large membranes and thickness down to 10 nm. We used a 50 nm thickness and 65 mm × 25 mm size membrane from micromatter with $T \approx 0.5$ @ 60 eV. We prepared the whole sample in the following way. The DLC membrane is put afloat in distilled water. The membrane is then taken out with the support for the experiment, which is a 40 mm × 25 mm metal plate with circular $\sim 1\,mm^2$ holes through which the experiment can be performed. The membrane and metal plate are dried under ambient conditions after which the membrane is attached to the metal plate (see Fig. 3.11). The plate with the membrane is brought into a glove box with argon atmosphere (1 ppm O_2, $-70°$ C dew point) where the air sensitive lithium borohydride can be prepared. In the glove box a saturated solution of lithium borohydride in tetrahydrofuran (THF) is prepared. We use commercially available 98% pure lithium borohydride from Sigma Aldrich. A drop of the solution is brought onto the DLC membrane with a pipette, whereas care has to be taken that no solution comes below the membrane. The solution dries within ~ 5 min and forms a ~ 1 µm thin layer. The layer is transparent and homogeneous as observed with an optical microscope. The transparency indicates the formation of a reasonably homogeneous layer. This has been confirmed in the x-ray absorption experiment where the absorption of the sample does not significantly change over typically several millimeters and via an optical microscope. The droplet forms a circular layer with ≈ 1 cm diameter, depending on the droplets size. The center is of good quality whereas at the edges the quality deteriorates.

We also tried to prepare the isoelectronic compounds $LiCH_3$ and $LiNH_2$ and the ionic compound LiCl in this fashion. All of them however do not grow uniform layers but show the formation of large grains, which renders these samples useless. The final sample is brought and attached to the spectrometer's vacuum chamber under argon atmosphere in an xyz-manipulator. A valve between the vacuum chamber and the manipulator can be

opened after the vacuum chamber is pumped to a pressure of $\sim 1 \times 10^{-6}$ mbar. The whole process ensures that the lithium borohydride layer never comes into contact with water or oxygen.

4 Coherent Raman Effect in Lithium Borohydride

4.1 Electronic, optical and vibrational properties of Lithium Borohydride

Lithium Borohydride crystallizes below 381 K in the orthorhombic space group Pnma with four units of $LiBH_4$ as shown in Fig. 4.1. It is an ionic compound with Li^+ cations and BH_4 anion groups. The BH_4 groups are almost tetrahedrally arranged [FCC08] although this was under dispute [SRCY02] for some time. At 381 K lithium borohydride undergoes a first order phase transition into the hexagonal high temperature phase with space group P63mc (see Fig. 4.2). In the following section the most recent almost tetrahedral structure from [FCC08] is used. This study uses neutron diffraction, which has a much better accuracy for proton positions.

It has a very high 18% mass portion of hydrogen, which makes it an attractive material for hydrogen storage. Hydrogen desorption and absorption have remained difficult [PM08] and require elevated temperatures and/or other special environments, which limited, together with its reactivity with air, its practical use so far.

In both the orthorhombic and hexagonal structure the lithium atom is quite close to an ideal Li^+ ion and the BH_4 group forms a tetrahedronal subunit by sp^3 hybridization quite similar to a CH_4 molecule with the excess electron from the lithium cation.

Lithium borohydride is an insulator in both the high and the low temperature phase with relatively large band gaps $\approx 7\,\mathrm{eV}$. For the remainder of this section we will describe the orthorhombic low temperature phase.

The band structure (Fig. 4.4) consist of several groups of four bands due to the four units of $LiBH_4$ in the unit cell, which are connected by the Pnma symmetry operations. The four lowest bands are composed of B2s + H1s states and the 12 other valence state are composed of B2p + H1s states. The lowest conduction band states are of Lithium and Boron 2s and 2p states [MOT+04, Ge04].

The symmetry equivalence leads to a full degeneracy in the R and S point and a partial degeneracy on the surface of the Brillouin zone, e.g. between X and S or at $Z \to U \to R$. Everywhere else these bands are split because of the interaction between the respective groups, i.e. the splitting is a measure how strong the crystal effects are or whether it is more a molecular crystal, where the splitting is relatively small. In the case of lithium

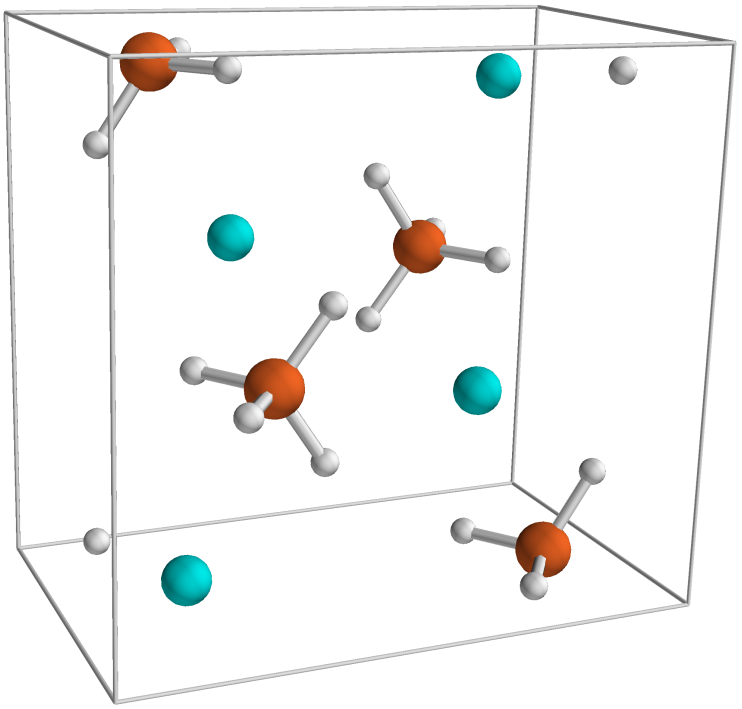

Figure 4.1: Orthorhombic unit cell of lithium borohydride at 225 K [FCC08]. Lithium atoms are depicted as green spheres, boron and hydrogen as orange and gray spheres respectively. There are four units of LiB_4 in the unit cell. Boron and hydrogen form an almost tetrahedral BH_4 anion, which is bound ionically to the lithium cation. The cell parameters are $a = 7.141$ Å, $b = 4.431$ Å and $c = 6.748$ Å. Its space group is Pnma (Nr. 62), which belongs to the D_{2h} point group.

borohydride the splitting is rather small and the bands are relatively flat, which indicates a rather weak interaction between the borohydride tetrahedrons and between different unit cells.

All orbitals, that are shown in the band structure, are predominantly located at the BH_4 tetrahedron. From a chemistry perspective this is no surprise because the ionic nature of the bond leaves the lithium atom with only two 1s core electrons and consequently all valence states belong to the BH_4 group. The species and angular-momentum-resolved density of states of lithium borohydride (Fig. 4.5) emphasizes this fact. The group of bands around -10 eV is almost exclusively of B2s + H1s character with very little Li admixture. The group below the band gap is of almost purely B2p + H1s character as expected for methane like chemistry. The overall very little density of states of lithium below the band gap is due to the ionic character of lithium borohydride and consequently very little valence occupation on the lithium sites.

A contour plot of the valence electron density, which is the density due to all orbitals in the band structure in Fig. 4.4 shows its concentration on the tetrahedrons and the approximate

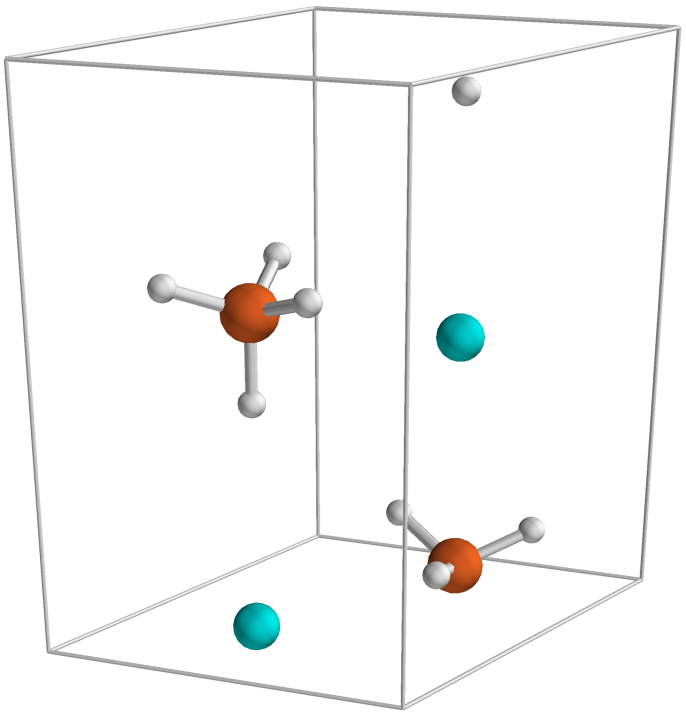

Figure 4.2: Hexagonal high temperature structure of lithium borohydride at 535 K [FCC08]. Lithium atoms are depicted as green spheres, boron and hydrogen as orange and gray spheres respectively. There are two units of LiB_4 in the unit cell. Boron and hydrogen form a tetrahedral BH_4 anion, which is bound ionically to the lithium cation. The cell parameters are $a = 4.3228$ Å and $c = 7.0368$ Å.

tetrahedral symmetry of the BH_4 groups. The valence electron density is necessarily a theoretical construct that is still helpful to emphasize the electronic properties that are responsible for the chemistry of the crystal.

All DFT calculations were performed with Quantum-Espresso [GBB+09], an open-source DFT package that uses a plane wave basis and pseudo potentials [CC76]. A kinetic energy cutoff of 40 Hartree for the plane wave basis, a Monkhorst-Pack k-grid [MP76] with $4 \times 4 \times 4$ k-points for Brillouin zone integration and the Perdew-Burke-Enzerhof (PBE) exchange correlation potential was used.

Lithium borohydride has 24 atoms in the unit cell, which leads to $3 \cdot 24 = 72$ phonon modes in total. Those are typically separated in three groups, namely acoustic phonons, external optical phonons and internal optical phonons and can be split into their irreducible representation as $11A_g + 7B_{1g} + 11B_{2g} + 7B_{3g} + 7A_u + 10B_{1u} + 6B_{2u} + 10B_{3u}$ [MOT+04]. In addition there are three acoustic phonon modes, that correspond close to the Γ point to a collective motion of all atoms in the x, y, z directions. The external optical phonons are displacements of either whole planes of atoms with respect to each other or lithium nuclei against BH_4 tetrahedrons, where the tetrahedron itself remains almost static. Internal

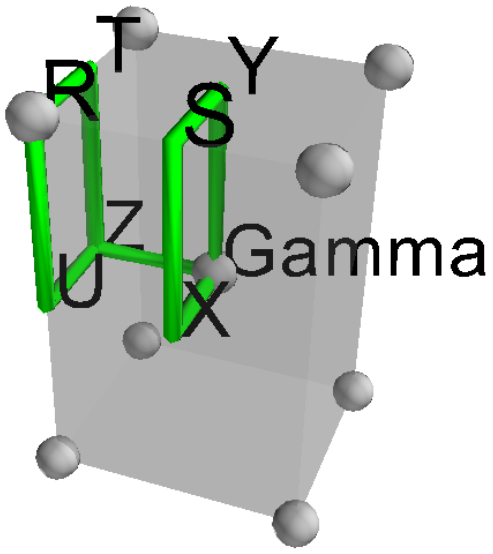

Figure 4.3: Brillouin zone of lithium borohydride together with the high symmetry path, that is used in the band structure calculations.

optical phonons are modes within the tetrahedrons. Because of the covalent bond between boron and hydrogen and the low mass of the protons, the energy scales are clearly separated between the three types of optical phonons in lithium borohydride. The internal and external modes can be separated by the gap between 500 cm^{-1} and 1000 cm^{-1}. The internal modes can be further divided into bending modes, which lie between 1100 cm^{-1} and 1400 cm^{-1} and stretching modes, which lie between 2100 cm^{-1} and 2400 cm^{-1} [MOT+04]. The internal modes are very similar to the Raman modes of the methane molecule, which has bending modes around 1500 cm^{-1} and stretching modes around 3000 cm^{-1}. The similar but somewhat blue shifted spectrum indicates a similar chemistry for methane and BH_4 anion with somewhat lower force constants, i.e weaker bonding, for the BH_4 anion compared to methane. The higher mass of carbon compared to boron does not play a role as the internal modes do not include movement of boron or lithium. An ab initio calculation of the vibrational modes of a BH_4^- molecule in vacuum with the nwchem code yields vibrational frequencies of 1060 cm^{-1}, 1180 cm^{-1} and 2280 cm^{-1} [1], which are very similar to the internal modes in lithium borohydride, especially for the stretching modes, which further shows the ionic bonding and low interaction between the cations and anions.

The assignment between experimental Raman peaks and theoretical modes is somewhat difficult as the spectral order of modes is often not correctly predicted. This can however be greatly improved by polarized Raman spectroscopy published in [GWS+11] and reprinted in Fig. 4.8. The Raman tensors of a mode with a certain irreducible representation such as A_g, B_{1g} etc. has a well defined form as seen in Eq. (4.1)

[1] For molecular BH_4^- there are only internal frequencies

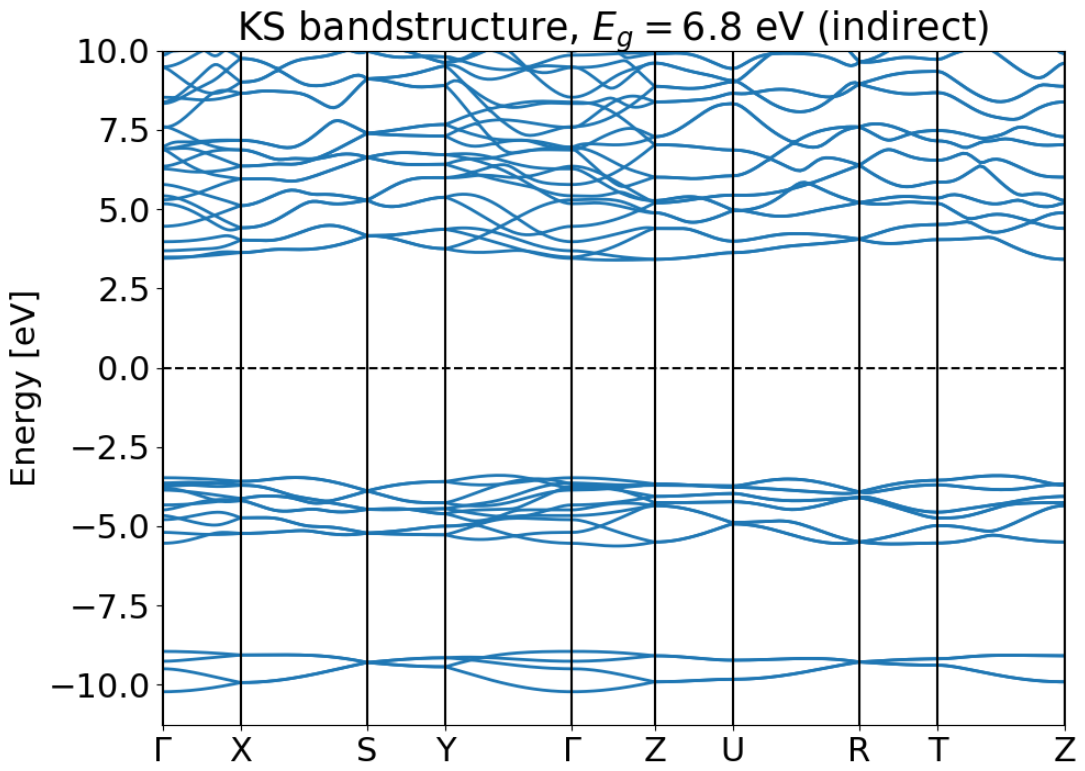

Figure 4.4: Kohn-Sham band structure of lithium borohydride calculated with quantum-espresso [GBB+09] and the PBE correlation-exchange functional [PBE96]. The experimental structure [FCC08] was used for this calculation. The DFT calculation yields a indirect band gap of 6.8 eV in the vicinity of Γ. All bands show a four fold degeneracy at the R and S point, due to the four symmetry equivalent units of $LiBH_4$, which splits off everywhere else because of the interaction between the units. All valence bands shown here represent states that predominantly occur on the BH_4 tetrahedron.

$$\frac{\partial\alpha}{\partial Q_{Ag}} = \begin{pmatrix} a & & \\ & b & \\ & & c \end{pmatrix} \qquad \frac{\partial\alpha}{\partial Q_{B1g}} = \begin{pmatrix} & d & \\ d & & \\ & & \end{pmatrix}$$
$$\frac{\partial\alpha}{\partial Q_{B2g}} = \begin{pmatrix} & e & \\ & & \\ e & & \end{pmatrix} \qquad \frac{\partial\alpha}{\partial Q_{B3g}} = \begin{pmatrix} & & \\ & & f \\ & f & \end{pmatrix} \tag{4.1}$$

This can be exploited with the use of a single crystal and polarized radiation and detection in a spontaneous Raman spectroscopy experiment. If the polarization and light propagation vector coincide with two crystal axis, certain modes, dependent on their irreducible representation, will only emit light with parallel polarization and the other modes will emit light perpendicular to it. In [GWS+11] (see Fig. 4.8) the geometry was chosen such that A_g and B_{2g} appear in parallel polarization and B_{1g} and B_{3g} appear in perpendicular polarization. This method is quite useful as the identification of the irreducible representation of a mode greatly improves the assignment of theoretical modes to the experimental ones. Theoretical prediction for the displacement, i.e. eigenvector, of

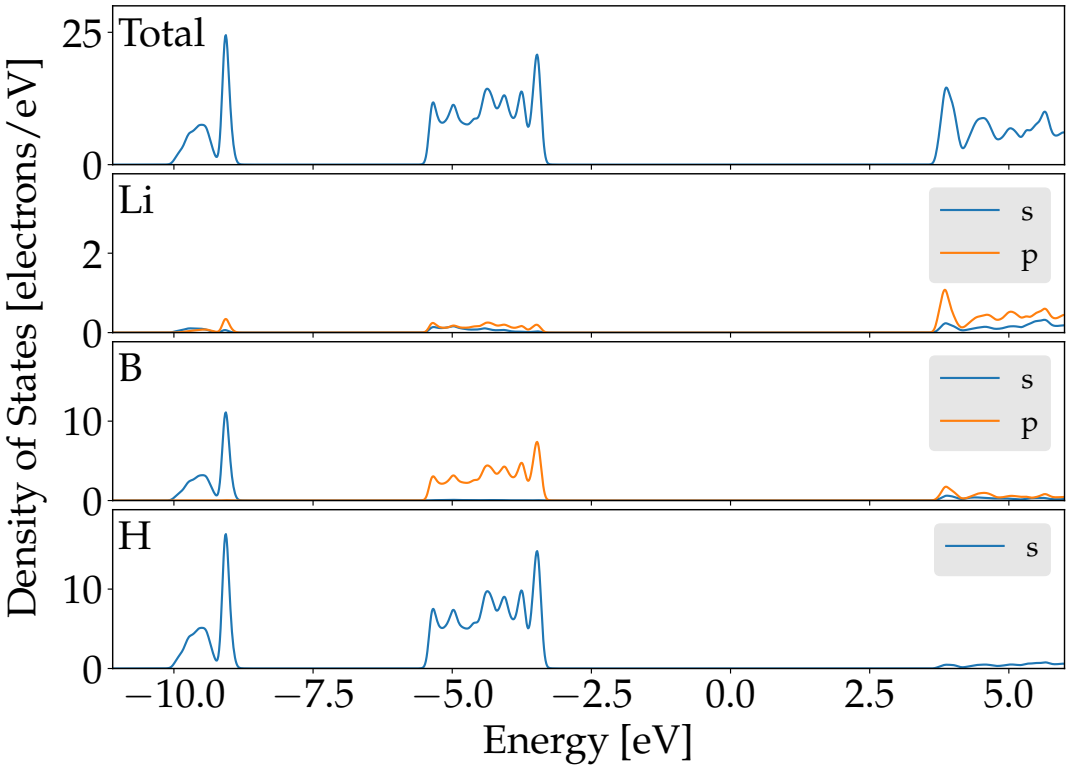

Figure 4.5: Site and angular momentum resolved density of states of lithium borohydride. The valence band is clearly dominated by the sp3 hybidized BH_4 tetrahedrons, with the lowest band being B2s + H1s and the three higher bands B2p + H1s. Due to the high ionicity of lithium borohydride the overall density of states is much lower for lithium than for the borohydride group (note the five times smaller scale for lithium). The low conduction band is still dominated by anti-bonding borohydride states, however lithium 2p states start to play a bigger role.

a mode are typically reasonably good, the amplitude and frequency however are often less accurate, which makes the assignment to experimentally observed peaks somewhat difficult, especially if several modes have similar frequencies and the energetic order of the theoretically predicted modes might be wrong. This is due to the fact that in non polarized Raman spectroscopy the experiment offers absolutely no information on the spatial shape of the mode, except that it is Raman active. Polarized Raman spectroscopy alleviates this problem, as at least the irreducible representation (or membership to a subset of representations) can be determined. For example the A_g mode at 308 cm^{-1}, which is investigated in this thesis, was formerly wrongly assigned to be B_{2g}, e.g. in[RSL+08].

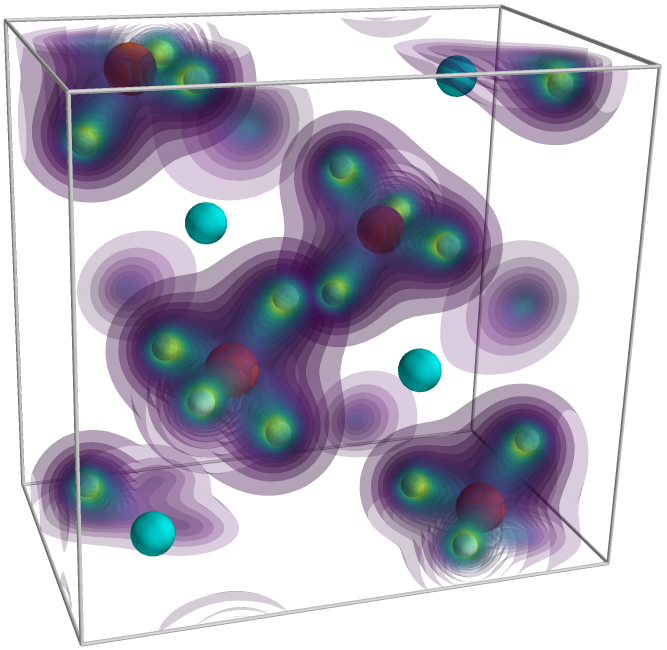

Figure 4.6: Valence electron density of lithium borohydride from first principle DFT calculations. This density is only calculated from the bands shown in Fig. 4.4 and therefore excludes lithium and boron core states. This valence electron density predominantly occurs on the borohydride tetrahedron due to the ionic bonding of the compound, which leaves lithium with only 1s, i.e. core electrons.

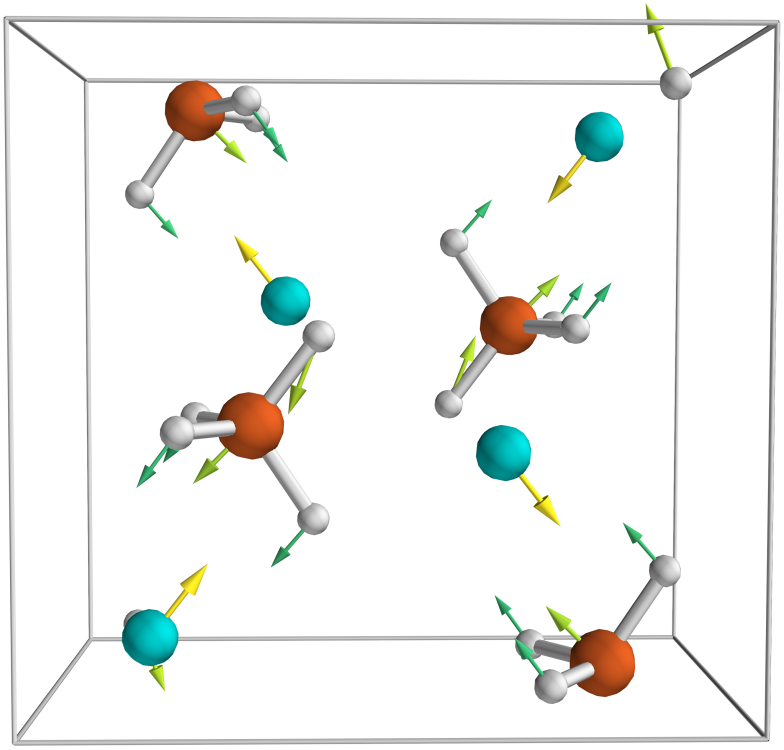

Figure 4.7: Nuclear displacement of the A_g Raman mode at 308 cm^{-1} depicted by arrows and as reported in [RSL+08]. The mode consist of similar motion of lithium and borohydride groups against each other, i.e. the lithium-borohydride distance is modulated by this mode.

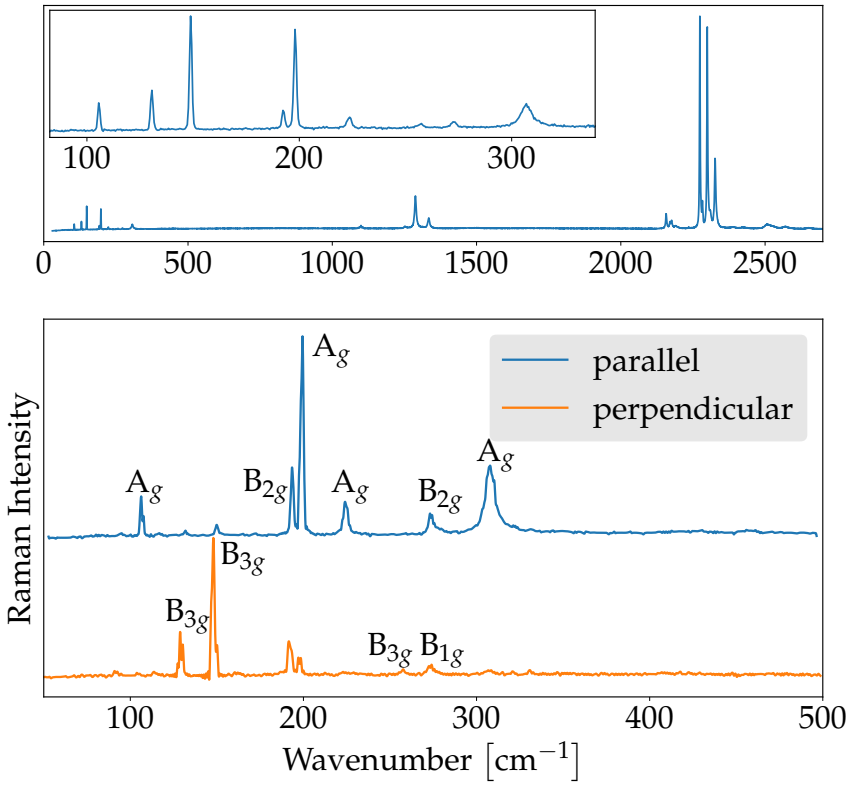

Figure 4.8: Top: Unpolarized Raman spectrum of lithium borohydride at 5 K as published in [RSL+08] and reprinted here. The Raman spectrum shows three distinct region, which can be identified as external modes between 100 cm^{-1} and 400 cm^{-1}, internal bending modes between 1200 cm^{-1} and 1400 cm^{-1} and internal bending modes between 2100 cm^{-1} and 2400 cm^{-1}. The inset shows an enlargement of the external modes in a non polarized experiment, where all Raman active modes appear in one spectrum.
Bottom: Polarized Raman spectrum of the external modes in Lithium Borohydride as measured in[GWS+11] at 5 K and reprinted here. The use of single crystal lithium borohydride and polarized radiation and detection allows for the discrimination of vibrational modes with different symmetry. In this case the configuration was chosen such that A_g and B_{2g} were visible in the parallel polarization and B_{1g} and B_{3g} were visible in the perpendicular polarization. At $\nu = 308\,cm^{-1}$ is the most high frequency external mode, which is of A_g character.

4.2 Time-resolved experiments with non-resonant Pump and XUV Probe Pulses

So far the physics and response of insulators connected to a non-resonant excitation are a relatively uncharted territory for several reasons. The response is typically almost instantaneous, in contrast to real excitations of a system, which can be very long-lived, and the response gives typically small signals in all spectroscopic techniques. If one uses a short pulse with high intensity to increase the response one needs a similarly short probe pulse to resolve the instantaneous response [2]. In lithium borohydride the response upon a femtosecond NIR with 800 nm wavelength has been studied using femtosecond x-ray diffraction [SZF+12]. Such results show an instantaneous polarization, which is due to a decrease in ionicity between the lithium cation and BH_4 anion, i.e. a relocation of electron density from BH_4 tetrahedrons to lithium cations. In this chapter we investigate the question, whether this relocation and its subsequent effects can be observed using x-ray absorption spectroscopy. For experimental reasons we chose to investigate the lithium K edge absorption spectrum, although one could also study the boron K edge. We used the experimental apparatus described in Chap. 3, a HHG XUV source and a grating based CCD spectrometer. Experimental CCD images of the XUV source with and without lithium borohydride sample are shown in Fig. 4.9 The energy dispersion is horizontal and high photon energies are to the left. The vertical axis reflects the spatial mode of the XUV beam. These images, which are raw experimental data of our apparatus, can be converted into spectra by integrating over the vertical dimension. In order to avoid unnecessary noise the integration is only performed over the relevant pixels close to the XUV beam. The result is shown in Fig. 4.10. Here the intensity on the camera with and without the $LiBH_4$ sample is plotted as a function of photon energy. The calibration procedure to convert pixel index to energy has been described in detail in Sec. 3.4. The spectrum of the HHG source is quite flat and without major modulation up to a cutoff at $\approx 72\,\mathrm{eV}$, which is due to the Al L-edge absorption from the aluminum filters in the optical path. The spectrum with sample shows an intensity, which is by a factor ~ 5 lower in the pre-edge region due to background absorption and by a factor ~ 500 at the main absorption peak [3]. The signal-to-noise ratio [4] is sufficient to resolve the low intensity at the main peak. From the two curves the absorption spectrum can be calculated according to $A = -\ln(I_{sample}/I_{source})$. One can subtract the background absorption by fitting the pre edge region with a $1/E^3$ function and subtracting the result from the whole spectrum. The absorption spectrum after this procedure is shown in Fig. 4.11 as black line. The absorption spectrum shows a strong peak at 60 eV, which is followed by a plateau region at higher energies. There is no pre-edge dipole forbidden feature as expected for a 1s→2p transition. The state and species resolved density of states (Fig. 4.5) shows lithium 2p states directly above the band gap.

[2] If one uses a long probe pulse the spike proportional to the short pump pulse in the response will be broadened and its amplitude will be reduced, which negates the advantage of the short pump pulse.

[3] Historically this peak has often been called white line because the high absorption here left the photographic plates that were used in early x-ray absorption spectroscopy underexposed.

[4] The signal to noise ratio is in the steady state case determined by the flux as signal and the electronic noise of the camera as noise.

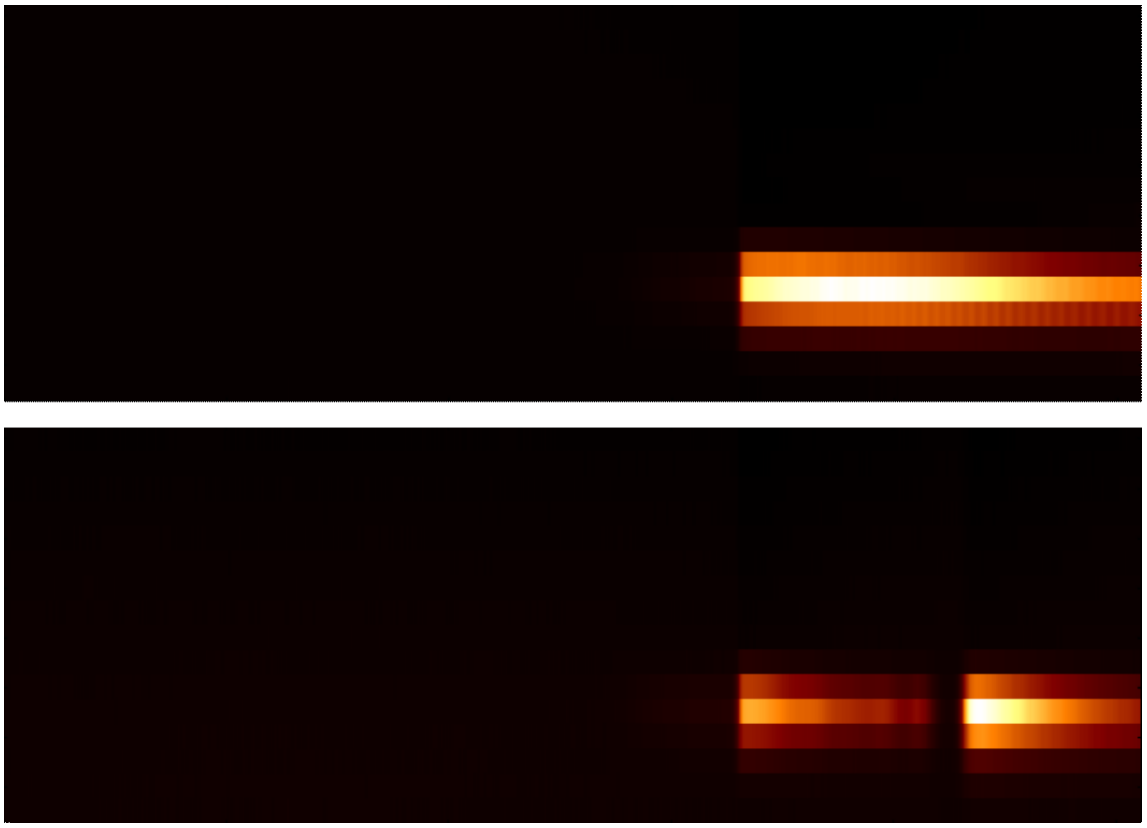

Figure 4.9: Measured CCD images of the two-color HHG spectrum without (top) and with lithium borohydride sample (bottom). The lithium k edge and the exciton peak are clearly visible in the lower image. The image consists of 1024×16 pixel and the acquisition time was 20 s for each image

Together with the excitonic effects this leads to the sharp main peak directly at the onset of the absorption. The absorption plateau can be seen as transition into higher conduction bands or transitions into free photoelectrons as the higher bands resemble more and more the free electron dispersion and states, especially above the work function. The blue and green curve show theoretical spectra with and without excitonic effect respectively. The excitonic effects were included with the BSE framework (see Sec. 2.2) and both curves were calculated by Eric L. Shirley. The difference is quite striking and together with the good agreement between experiment and the BSE calculations shows the importance of excitonic effects for the lithium borohydride Li K-edge. Experimentally the thickness of the sample was not known, so the absolute magnitude of the absorption could not be determined experimentally. In BSE the absolute energy scale is not known with good precision. Thus, in Fig. 4.11 both amplitude and position of the BSE spectrum was fitted to the experimental spectrum. The same parameters were applied to the theoretical spectrum without excitonic interaction.

In Fig. 4.12 a transmission spectrum of lithium borohydride measured using a Neon single-color (sc) HHG source is shown. Here only the plateau absorption is measured as the exciton peak is between two harmonics. In the plateau region there are four harmonics before the Al L-edge absorption of the metal filter. In our time-resolved experiments we performed both measurements using the single-color HHG source (better SNR as discussed

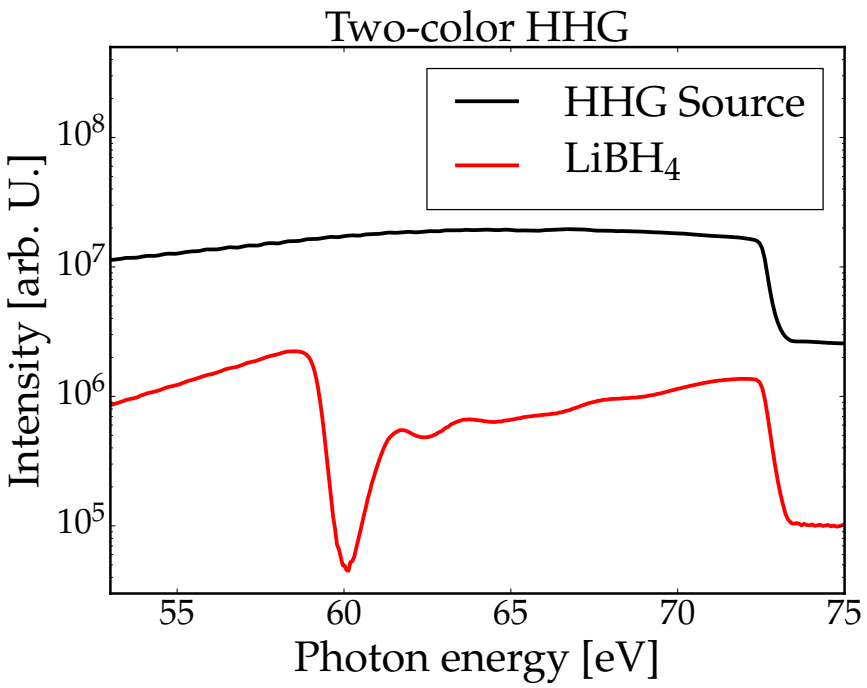

Figure 4.10: Measured XUV spectrum as extracted from Fig. 4.9. The two-color HHG spectrum is perfectly flat and continuous within the spectral resolution of the detection scheme of < 200 meV and ideally suited for absorption spectroscopy. The spectrum with sample, labeled $LiBH_4$ shows a strong excitonic white line at 60 eV with a decrease of almost two orders of magnitude compared to the pre-edge and almost four orders of magnitude compared to without sample, which shows the excellent dynamic range of the detection system.

in Sec. 3.5) and those using the two-color HHG source. The two-color source provides information in the gaps between the discrete harmonics but has a 10 times smaller SNR ratio.

With the single color experiment we are much more sensitive to changes in amplitude than shifts because the plateau region is relatively flat so a shift has little effect on the absorption at the HHG peaks.

Both, in the time-resolved experiments using the single color and the two color HHG we pumped with $\approx 2\,\mu J$, 800 nm pulses with a beam waist at the sample of $\approx 100\,\mu m$. $2\,\mu J$ was roughly half the instantaneous damage threshold, i.e. with $4\,\mu J$ the sample spot was destroyed immediately after irradiation. With $2\,\mu J$ sample degradation still occurred over a timescale of several hours so that the sample was moved after roughly one hour to a new spot. Irradiation with $4\,\mu J$ produced a hole in the sample, i.e. the full HHG spectrum was transmitted after the irradiation. The long term damage by $2\,\mu J$ on the other hand was visible as a broadening of the exciton peak. We can deduce that the irradiation with $2\,\mu J$ must lead to a structural change in the sample, which could be related to the phase transition at 381 K. Probably the structural change is a reduction in grain size of the polycrystalline sample together with an increase in lattice defects.

The single color experiments were performed on two different days with 8 hours of

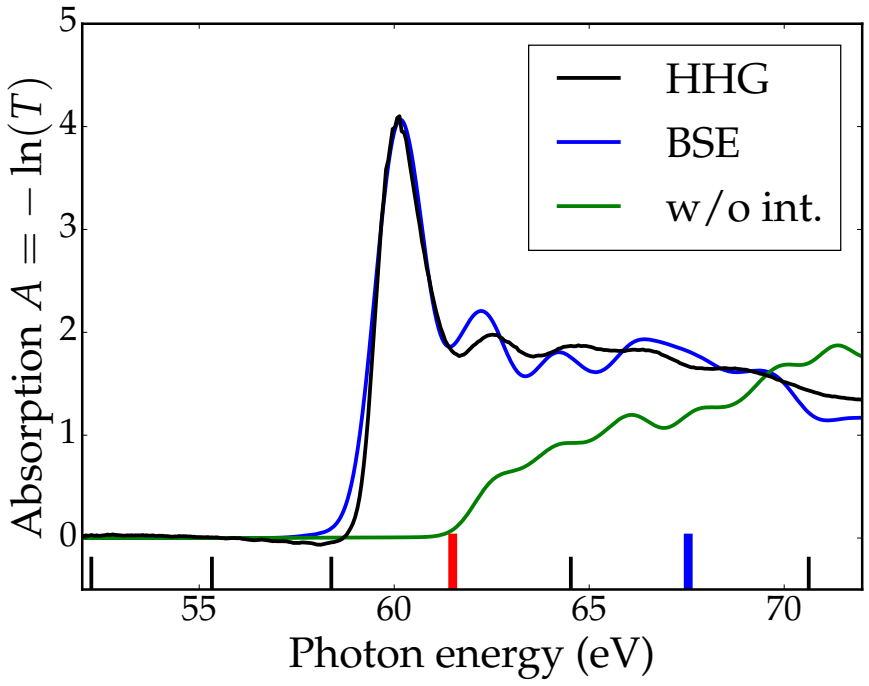

Figure 4.11: Absorption spectrum of a polycrystalline layer of lithium borohydride as measured with a two-color HHG source (black). The lithium K-edge at 60 eV shows a strong excitonic peak without pre edge features as expected for a 1s $\rightarrow$ 2p transition. The absorption spectrum calculated with the Bethe-Salpeter equation (BSE) shows excellent agreement with the measured spectrum. The exact thickness of the sample was not known and the exact position of the peak is not known in BSE, so position and amplitude of the BSE spectrum were fitted to the experimental spectrum. The fit yields a thickness of the sample of d = 0.75 µm. As comparison the theoretical spectrum without excitonic interaction (w/o int.) shows extremely poor agreement, which highlights the strongly excitonic character of the transition.

combined pure measurement time and the two color experiment on a single day with 10 hours measurement time. In both experiments the pump chopper was set to a frequency of 12.5 Hz and as a consequence the probe chopper to a frequency of 25 Hz. The exposure time of the camera was set to 20 ms, which corresponds to the full theoretical opening time of the probe chopper. For each delay 1000 frames (20 s pure measurement time, 40 s wall time) were taken in the single color experiment and 100 frames (2 s pure measurement time, 4 s wall time) in the two color experiment. The delays were linearly spaced between −100 fs-250 fs with 130 steps (SC-HHG) and −200 fs-500 fs with 500 steps (TC-HHG). The delay times were randomly sorted to rule out any systematic errors. The acquisition system directly determines, which frames are pumped and unpumped from a voltage signal of the pump chopper and saves it into different files for each delay. In a first analysis step all the images in one file are first compressed into spectra by summing over the vertical axis of the image. In a second step for each delay the relative intensity change $\frac{\Delta I}{I}$ as a function

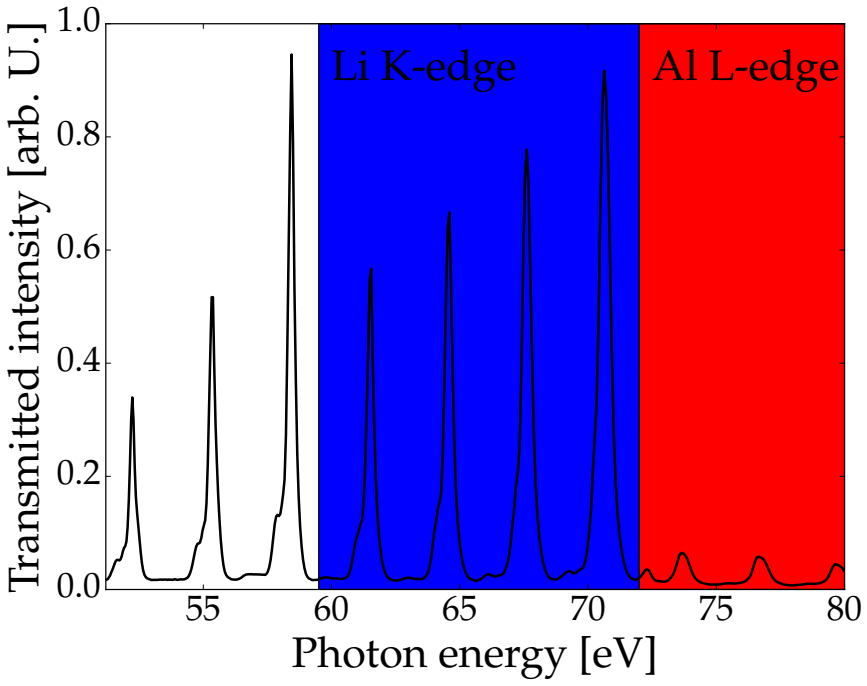

Figure 4.12: Transmitted intensity of a single color HHG source through a lithium borohydride sample. The exciton peak located at 60 eV is between two harmonics and not visible in this spectrum.

of photon energy can be calculated by summation of unpumped and pumped intensity.

$$\frac{\Delta I}{I} = 2\frac{I_p - I_{up}}{I_p + I_{up}}$$

$$I_p = \sum_i I_{p,i} \qquad\qquad I_{up} = \sum_i I_{up,i}$$

Here $I_{p,i}$ and $\sum_i I_{up,i}$ are the pumped and unpumped measured intensity of a single 20 ms acquisition, which are summed to yield the full intensity for one delay. The summed intensity is high enough so that the denominator in the relative intensity change cannot become zero through statistical fluctuations. For low changes in the relative intensity we can approximate the change in absorption as

$$\begin{aligned}\Delta A &= -\log(T + \Delta T) + \log(T) = -\log\left(1 + \frac{\Delta T}{T}\right) \\ &\approx -\frac{\Delta T}{T} = -\frac{\Delta I}{I}\end{aligned}$$

Such an absorption change is calculated for each measured delay, i.e. ≈ 700 in the single color case. Neighboring delays can now be further averaged to improve the signal-to-noise ratio, but thereby decreasing the temporal resolution. In the experiment we deliberately chose a very small step in the order of few femtoseconds, which is well below the temporal resolution of the experiment of ≈ 50 fs. Afterwards we can average over the very fine delays to improve the signal to noise ratio and determine accurate error bars. The error in

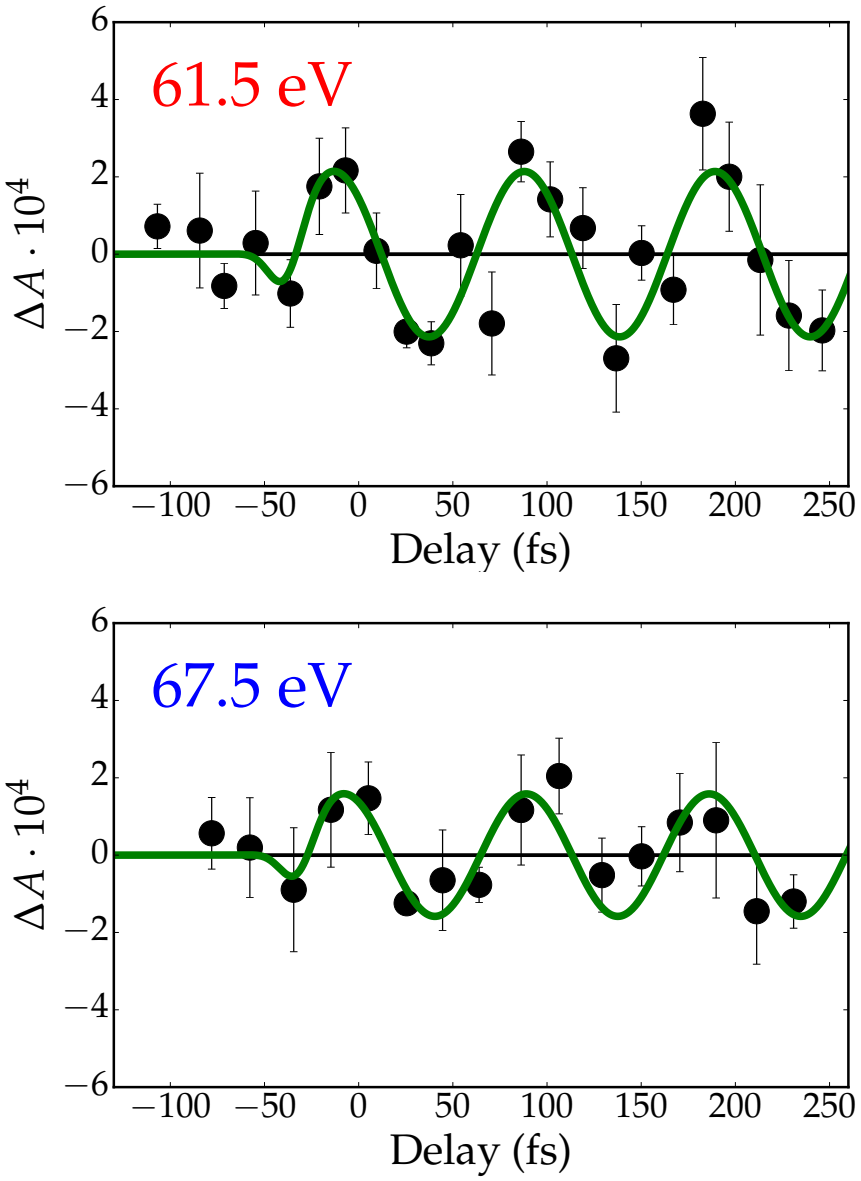

Figure 4.13: Measured transient absorption change ΔA of lithium borohydride upon excitation with an 800 nm probe pulse at photon energies of 61.5 eV and 67.5 eV. Both transients show a harmonically modulated absorption change after time delay zero. The fit (green line) was performed with the theoretical formula for the displacement of the theory of impulsive Raman scattering (Eq. (2.11)).

absorption $\delta\Delta A$ is calculated with

$$\delta\Delta A = \frac{\sqrt{\mathrm{Var}\,\Delta A_i}}{\sqrt{N_{bin}}},$$

where ΔA_i are the absorption changes included in one bin and N_{bin} the number of absorption changes in one bin. The absorption change of the 61.5 eV and 67 eV harmonic in the single color experiment with a binning of $N_{bin} = 30$ is shown in Fig. 4.13. Both transients show a harmonic oscillation with the same phase and similar amplitude of $\Delta A = 2.1(3) \times 10^{-4}$ for 61.5 eV and $\Delta A = 1.6(3) \times 10^{-4}$ for 67.5 eV

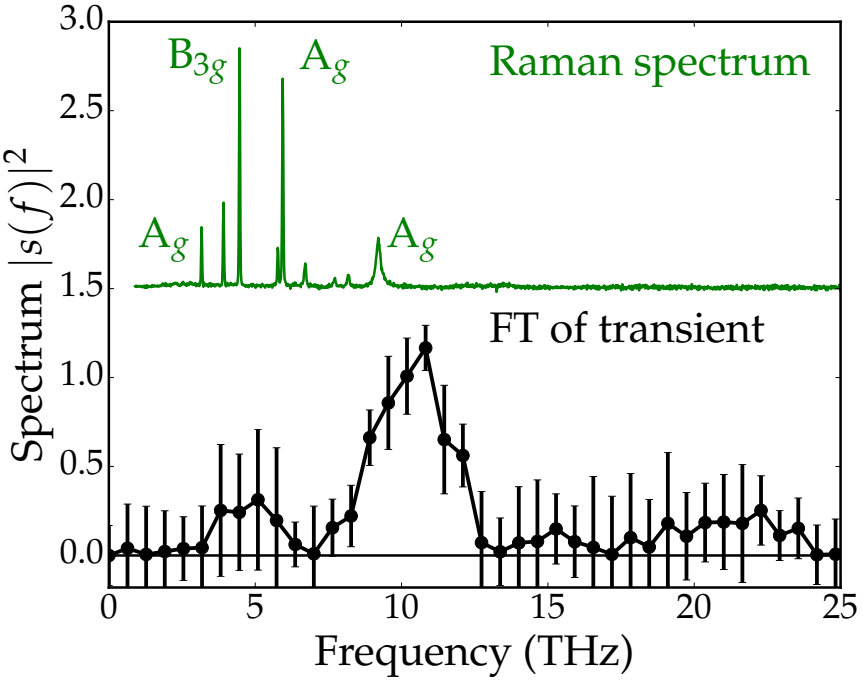

Figure 4.14: Fourier transform of the measured transient at 61.5 eV (see Fig. 4.13) in comparison with the Raman spectrum of lithium borohydride from [RSL+08]. There is only one significant frequency component in the spectrum at 10 THz, which we interpret as a coherent phonon oscillation of the Ag Raman mode.

An absorption change in the order of 10^{-4} is quite small and relatively close to our noise level. This is due the non-resonant excitation we have chosen. Resonant excitation yields typically larger and more long lived responses because of its direct effects on the XUV absorption such as Pauli blocking, band gap renormalization, conduction band electron screening and chemical shifts. The Fourier transformation of the 61.5 eV transient shows a strong peak at $f = 10$ THz, coinciding with the fit in Fig. 4.13. Other frequencies are not significant so that we conclude that there is a single dominant component that we are able to observe in our experiments.

Please note, we do not observe any additional absorption change during pump-probe overlap, i.e. at zero delay, which would be expected if the instantaneous induced polarization had a strong effect on the x-ray absorption spectrum.

Our interpretation of the observed signal is that we see an excitation of coherent phonons through impulsive stimulated Raman scattering (see Sec. 2.4.1). This type of Raman scattering excites all Raman active phonon modes, whose oscillation period is longer than the pump pulse duration. The time-dependent displacements of the nuclei affect the optical properties of the material. This is well known in all-optical [DSFI+85] experiments but (to our best knowledge) has been observed for the first time in x-ray absorption spectroscopy in this work. We used a parallel polarization for the pump and probe beam, which means that we mainly observe A_g Raman modes. We can write the change in the dielectric function, which is proportional to the change in absorption and relative intensity

as

$$\Delta\varepsilon_2(\omega_{XUV}) \approx \frac{\partial\varepsilon_2(\omega_{XUV})}{\partial q_i}\delta q \propto \frac{\partial\varepsilon_2(\omega_{XUV})}{\partial q_i}\,\mathbf{E}\cdot\frac{\partial\varepsilon_1(\omega_l)}{\partial q_i}\cdot\mathbf{E},$$

which means that the third order nonlinearity can be expressed as

$$\chi^{(3)} = \frac{\partial\varepsilon_2(\omega_{XUV})}{\partial q_i} \otimes \frac{\partial\varepsilon_1(\omega_l)}{\partial q_i}, \tag{4.2}$$

where $\otimes$ denotes the tensor product. The change in absorption, which as it is third order nonlinearity effect, is described by $\chi^{(3)}$ depends on the tensor product of the derivative of the dielectric function with respect to the phonon coordinate at the laser frequency and the XUV frequency. In the case of a polycrystalline sample one has to average over all crystal orientations. We use the scheme presented in [AT77] and find the following relative strengths:

A_g modes dominate in the non-linear signal as the tensor product of two A_g tensors is purely A_g as well. The tensor product of two non A_g tensors (with the same irreducible representation as in Eq. (4.2)) always contains an A_g irreducible representation but with much smaller percentage. In the spatial average in the parallel polarization case only A_g irreducible representations of the product tensor $\chi^{(3)}$ contribute, which favors A_g modes.

The two color experiment yields continuous information with regard to the photon energy. The measured ΔA can be seen in Fig. 4.15 a). Its ≈ 10 times higher noise than in the single color measurement however masks the signal. We performed a Fourier transform of the directly measured transients, which can be found in Fig. 4.15 b). Here above the edge significant peaks are visible at 10 THz and 18 THz are visible. We applied a Fourier filter around 10 THz, which allows us to extract only the desired frequency component (Fig. 4.15 c)). One can now apply an inverse Fourier to c) to arrive back in the time domain with only the 10 THz signal component (Fig. 4.15 d)). The Fourier filtered transient map now shows significant oscillations, which are visible for photon energies higher than 61 eV, i.e. above the Lithium K-edge and start after time delay zero. Within the delay range to up to 500 fs there is no significant decay of the oscillations, which indicates a much longer decoherence-and life time of the phonon mode.

As a next step we want to extract a transient spectrum from the experimental data. We used the following steps. We first binned the data spectrally by a factor of 10. For every spectral point we perform a fit in the time domain with the impulsive stimulated Raman displacement (Eq. (2.11)) similar to the single-color analysis (see Fig. 4.13). From this fit we know the positions of the minima and maxima of the oscillation, i.e. the phase of the oscillation. Next we average the points of the transient close to the maximums and minimums to retrieve the respective amplitude of the oscillation. The minimum and maximum of the oscillation are obviously related. We chose to determine them separately to verify the viability of our approach. This procedure is repeated for every spectral point and yields two values for each, one for the maximum and minimum respectively. The change in absorption is $\Delta A \approx 10^{-3}$, which is 5 times larger than in the single color case. The reason is probably a better spatial pump probe overlap as the transversal mode quality

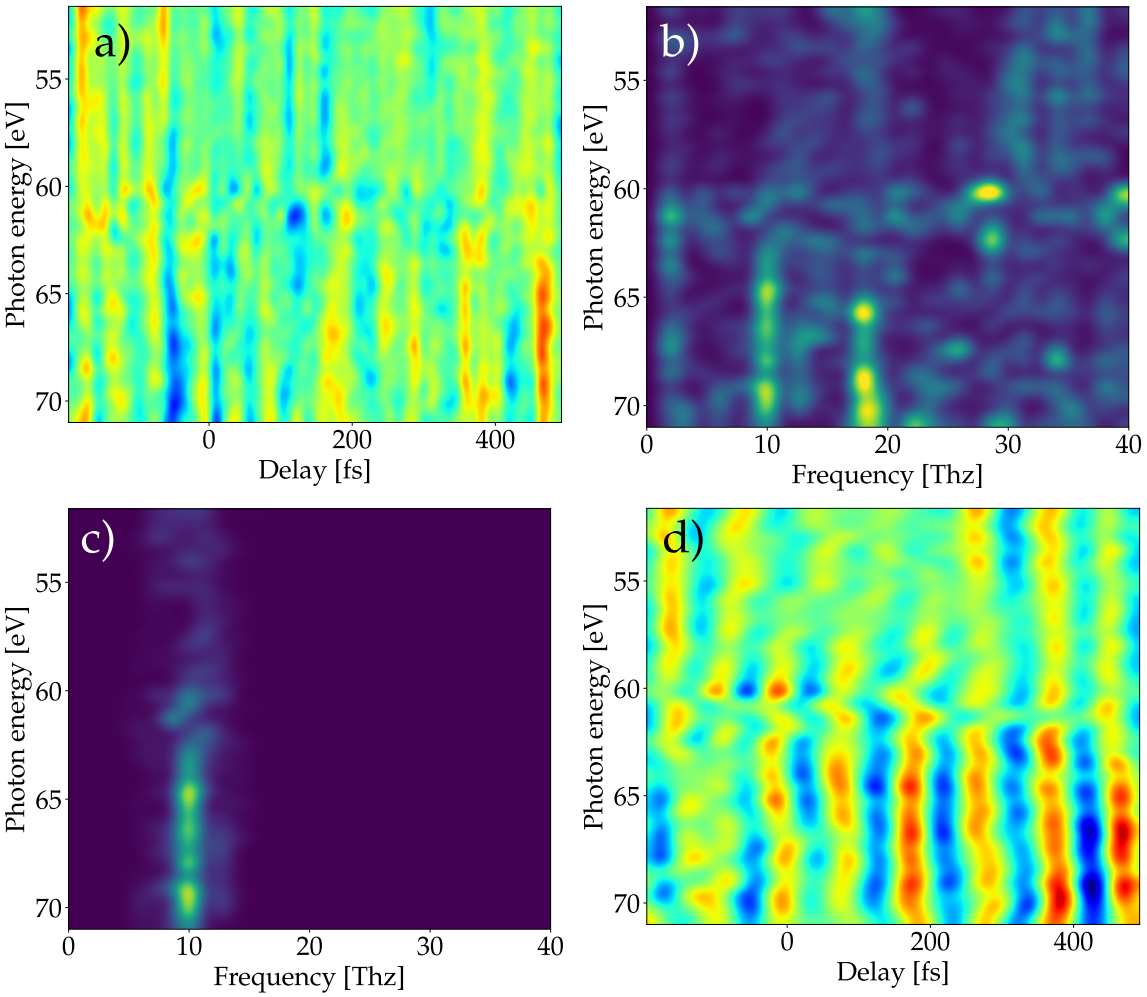

Figure 4.15: Experimental results of the two-color HHG pump-probe measurements. **a)** Measured ΔA as a function of XUV photon energy and pump-probe delay. The low SNR masks the signal here. **b)** Fourier transform of a) with respect to the delay. In the Fourier transform peaks are visible at 10 THz and 18 THz. From the single color experiment we expect a signal at 10 THz. With a Fourier filter it is possible to extract only the desired frequencies and suppress all the other ones. **c)** Fourier filter at 10 THz applied to the Fourier transformation in b). The FT is multiplied with a Gaussian function, which is centered at 10 THz. **d)** Inverse Fourier transform of c) back into the time domain. The filtered transient map now shows oscillations at 10 THz, which start around time delay zero and are visible above the edge at photon energy larger than 61 eV.

of the pump beam was improved between the two experiments. The points around the exciton peak were excluded because the low flux does not allow for a reliable measurement there. The transient spectrum shows no significant signal before the edge and a more or less constant plateau after the exciton peak. The BSE calculation shows a similar behavior although it predicts a strong change of absorption at the exciton peak, which is caused by a shift of the peak.

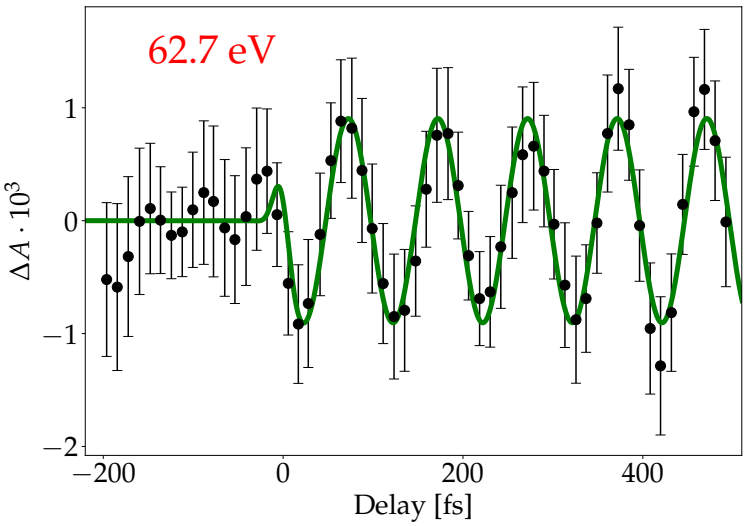

Figure 4.16: Transient absorption change ΔA ($\cdot$ with 1 standard deviation error bars) of lithium borohydride in the two color experiment at 62.7 eV after Fourier filtering. This transient is a single horizontal line from Fig. 4.15 d). An oscillation at 10 THz start around time delay zero and continues with no significant decay until the maximum delay of $\approx$ 500 fs. We fitted the transient with the ISRS theoretical prediction for the nuclear displacement (Eq. (2.11)). The fit yielded $\Delta A = 9.0(4) \times 10^{-4}$.

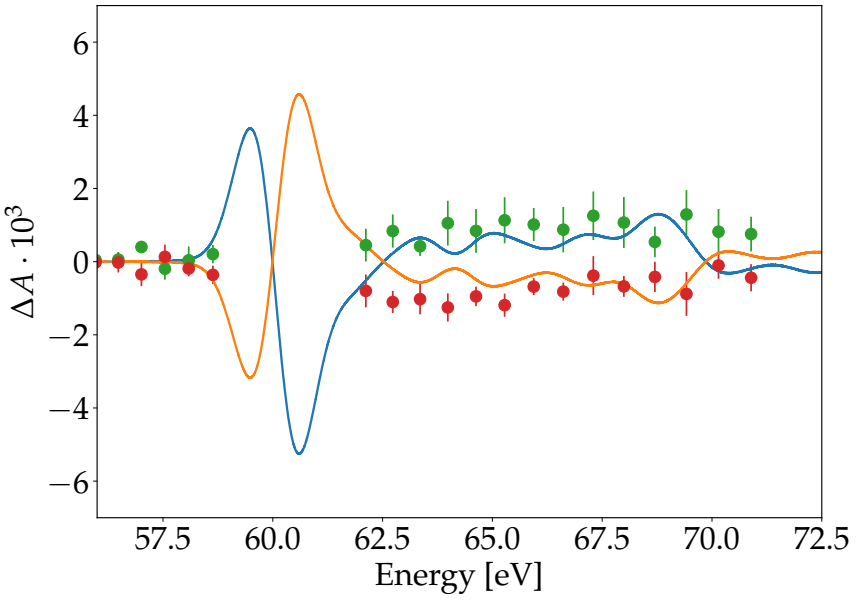

Figure 4.17: Transient spectrum as measured with two color HHG in comparison with the theoretical result from BSE with an absolute displacement of $q = 5(1) \times 10^{-4}$ Å$u^{\frac{1}{2}}$. The green and red points are the extremal points of the 10 THz oscillation in the measured transients. The absorption change calculated with BSE (solid lines) are fitted to the experimental data, which yields an absolute value for the nuclear displacement.

4.3 Absolute nuclear Displacements

Both our single color and two color experiments show the excitation of coherent Raman mode at ≈ 10 THz. The actual spatial displacement of the nuclei modulates the optical properties of the material in the lithium K edge region, which we are able to detect via absorption spectroscopy. The measured signal depends on the response of the dielectric function upon nuclear displacement, i.e. in linear approximation upon $\frac{\partial \varepsilon_2(\omega_{XUV})}{\partial q_i}$ times the amplitude q of the nuclear displacement, which in turn depends on the Raman polarizability $\frac{\partial \alpha(\omega_l)}{\partial q_i} = \varepsilon_0 V_{uc} \frac{\partial \varepsilon_0(\omega_l)}{\partial q_i}$. The absolute nuclear displacement can be determined with two different approaches. Either one can determine the response upon displacement, i.e. $\frac{\partial \varepsilon_2(\omega_{XUV})}{\partial q_i}$ via theory and compare it to the observed change in absorption. Or one can determine the Raman polarizability either by theory or in an absolute Raman experiment and calculate the displacement with the theory presented in Sec. 2.4.1. We follow both approaches; in the next section we present measurements of the Raman polarizability of lithium borohydride with a Raman scattering experiment, which together with the pump conditions in the x-ray absorption experiment determines the nuclear displacement. In Sec. 4.3.2 we use the Bethe Salpeter equation to determine $\frac{\partial \varepsilon_2(\omega_{XUV})}{\partial q_i}$ and consequently the nuclear displacement.

4.3.1 Raman-Polarizability Approach

The aim of this section is to determine the actual nuclear displacement, which was observed via x-ray absorption, using spontaneous Raman scattering in combination with the theoretical framework described in Sec. 2.4.1. The displacement according to Eq. (2.11) and Eq. (2.12) together with Eq. (2.5) depends on the electric field, which is applied, the phonon eigenvector of the mode under study and the Raman polarizability. The electric field can be determined from the pulse energy and mode parameters of the pump beam. The phonon eigenvector and Raman polarizability are harder to determine.

The absolute Raman polarizability is not measured in spontaneous Raman spectroscopy, as it requires measurement of the incoming laser intensity and scattered intensity into the full solid angle. Typical Raman experiments only measure the relative amplitude of different Raman modes and consequently polarizability relative to each other, i.e. without absolute unit. Andreas Borgschulte performed an absolute Raman measurement of lithium borohydride for us, which we will describe in the next paragraph.

We used a standard commercially available Raman spectrometer (Bruker Senterra) and calibrated it by measuring the Raman intensities of substances with known absolute Raman polarizabilities. Afterwards the Raman spectrum of lithium borohydride was measured under the same experimental conditions to ensure comparability so that the absolute Raman polarizability of lithium borohydride can be calculated. In this scheme we use a powder sample of ZnS to calibrate the spectrometer. The scattered intensity is strongly influenced by the geometry of the sample, i.e. grain size, surface roughness, powder or crystalline, so it is important to use a similar sample as with lithium borohydride, which was a powder sample.

The differential Raman cross section of a Stokes mode i [PP96] is

$$\frac{d\sigma_i}{d\Omega} = \frac{\nu_s^4}{4\varepsilon_0^2 c^4}\left|\mathbf{e}_s \frac{\partial\alpha}{\partial q_i}\mathbf{e}_l\right|^2 \frac{h(n_i+1)}{8\pi^2\nu_i} \qquad n_i = \frac{1}{\exp\left(\frac{h\nu_i}{k_B T}\right)-1}$$

Here ν_l (ν_s), $\mathbf{e}_l$ ($\mathbf{e}_s$) are the frequency and polarization of the incoming and scattered laser light and ν_i and $\frac{\partial\alpha}{\partial q_i}$ the frequency and Raman polarizability of the respective mode. The measured intensity is proportional to $\frac{d\sigma_i}{d\Omega}$ and can be expressed in the convenient form

$$I^i_{exp} = C_{exp}\left|\frac{\partial\alpha}{\partial q_i}\right|^2_{avg} \frac{n_i+1}{\nu_i}$$

C_{exp} now only depends on natural constants and the experimental conditions such as laser intensity, collected solid angle, sample thickness, quantum efficiency of the detector etc.. From a known $\left|\frac{\partial\alpha}{\partial q_i}\right|^2_{avg}$ one can determine C_{exp} as

$$C_{exp} = \frac{I_{exp}\nu_i}{(n_i+1)\left|\frac{\partial\alpha}{\partial q_i}\right|^2_{avg}} \tag{4.3}$$

C_{exp} is now a calibration for further measurements under the exact same conditions and the Raman polarizability of a different mode and sample can be determined as

$$\left|\frac{\partial\alpha}{\partial q_i}\right|^2_{avg} = \frac{I_{exp}\nu_i}{(n_i+1)C_{exp}}$$

We use a two step approach to determine $\left|\frac{\partial\alpha}{\partial q_i}\right|$ for the lithium borohydride A_g Raman mode at $\nu = 306\,\mathrm{cm}^{-1}$, which was observed in the transient x-ray absorption experiment. First we measured a ZnS mode with $\nu = 345\,\mathrm{cm}^{-1}$ at 300 K (see upper black curve in Fig. 4.18) and perform a Gaussian fit to find its intensity as $I(\mathrm{ZnS}, \nu = 345\,\mathrm{cm}^{-1}, T = 300\,\mathrm{K}) = 2.2\times10^4$ arb.U. from which we can set a calibration according to Eq. (4.3) with the literature value $\left|\frac{\partial\alpha}{\partial q}\right| = 1.8\,\text{Å}^2\mathrm{u}^{-1/2}$ [CVC82][5] We measured a Raman spectrum of lithium borohydride under the very same experimental conditions (green curve in Fig. 4.18). At room temperature the A_g $300\,\mathrm{cm}^{-1}$ mode is however severely broadened and not clearly resolved. In a first step we determine the combined Raman polarizability for the B_{2g}/A_g peaks at $\approx 190\,\mathrm{cm}^{-1}$, which at room temperature is broadened into one peak. The combined intensity for the two peaks was measured as $I(\mathrm{LiBH_4}B_{2g}/A_g, \nu = 190\,\mathrm{cm}^{-1}, T = 300\,\mathrm{K}) = 1.3\times10^4$ arb.U., which with the ZnS calibration yields

$$\left|\frac{\partial\alpha}{\partial q}\right|_{B_{2g}/A_g} = 2.5\times10^{-17}\,\mathrm{C}^2\,\mathrm{s}^2\,\mathrm{kg}^{-3/2}\,\mathrm{m}^{-1}$$
$$= 0.9\,\text{Å}^2\,\mathrm{u}^{-1/2} \quad \text{(Gaussian units[6])}$$

[5] Calleja et. al. define the Raman tensor in an old fashioned way, which can only be strictly used for one or two atomic unit cells. Their definition differs by the square root of the reduced mass and they state its unit as Å^2. The relation between the modern definition and theirs is $\frac{\partial\alpha}{\partial q} = \frac{R_{ij}}{\sqrt{M_r}}$ with $M_r = \frac{m_1 m_2}{m_1+m_2}$ the reduced mass of the material.

For the actual determination of the desired $\frac{\partial\alpha}{\partial q}$ we use a Raman spectrum measured at 5 K from Racu et. al. [RSL+08]. As we know the Raman polarizability of the A_g/B_{2g} pair at $\sim 190\,\mathrm{cm}^{-1}$ and its intensity can be determined from the spectrum as $I = 3100$ arb.U. we can easily compare this to the $300\,\mathrm{cm}^{-1}$ A_g mode within the same spectrum, whose intensity is $I(A_g, 300\,\mathrm{cm}^{-1}, 300\,\mathrm{K}) = 2400$ arb.U. The Raman polarizability is then given by

$$\begin{aligned}\left|\frac{\partial\alpha}{\partial q}\right|_{A_g} &= \left|\frac{\partial\alpha}{\partial q}\right|_{B_{2g}/A_g}\sqrt{\frac{I_{A_g}\nu_{A_g}}{I_{B_{2g}/A_g}\nu_{B_{2g}/A_g}}} \\ &= 2.7(8)\times 10^{-17}\,\mathrm{C}^2\,\mathrm{s}^2\,\mathrm{kg}^{-3/2}\,\mathrm{m}^{-1} \\ &= 1.0(3)\,\text{Å}^2\,\mathrm{u}^{-1/2} \quad \text{(Gaussian units)}\end{aligned}$$

In order to determine the error we measured the absolute Raman coefficient of Silicon (see Fig. 4.18) under the same experimental conditions as for ZnS and compared the determined value to a literature value from Aggarwal et. al. [AFS+11], where we find a 25% discrepancy from their value, which we take as the relative error of our whole scheme.

The other necessary ingredient, the phonon eigenvector, is difficult to observe experimentally as a direct observation of the displacements of the nuclei would be necessary. In principle this would be feasible by ultrafast x-ray diffraction and together with impulsive excitation of a single Raman mode . However the achievable displacements are too small to be observed with the typical spatial resolution of x-ray diffraction experiments, which is in the order of Å. Instead we use the phonon eigenvectors, which were calculated with a DFT calculation and published in [RSL+08]. The eigenvectors are typically quite accurate as they are partially fixed by the symmetry of the respective mode and other factors such as zero center of mass motion and that ab eigenvector must be normalized. In comparison the eigenvalues, i.e. the Raman frequencies and derived quantities such as intensities are less accurate.

With an absolute value for the Raman polarizability we can now use the result from the theory chapter and combine equations (2.11), (2.12) and (2.13) in order to calculate the absolute displacement of the lithium atoms under the experimental conditions

$$q = \left|\frac{\partial\alpha}{\partial q}\right|\frac{E_0^2\sigma_t}{2\sqrt{2}\omega_0}\exp\left(\frac{-\omega_0^2\sigma_t^2}{4}\right)$$

The electric field can be calculated with

$$\begin{aligned}I_0 &= \frac{2E_P}{\sqrt{\pi^3 w_0^2\sigma_t}} \approx 2\times 10^{11}\,\mathrm{W\,cm}^{-2} \\ E_0 &= \sqrt{\frac{2I_0}{c\varepsilon_0}} \approx 1\,\mathrm{V\,nm}^{-1}\end{aligned}$$

The pulse energy was $E_p \approx 2\,\mu\mathrm{J}$, the beam waist was $w_0 \approx 100\,\mu\mathrm{m}$ and the pulse duration $\sigma_t \approx 20\,\mathrm{fs}$ (FWHM=35 fs).

[6] Polarizabilities and Raman polarizabilities are often stated in Gaussian units. Here they are added for better comparability to other publications

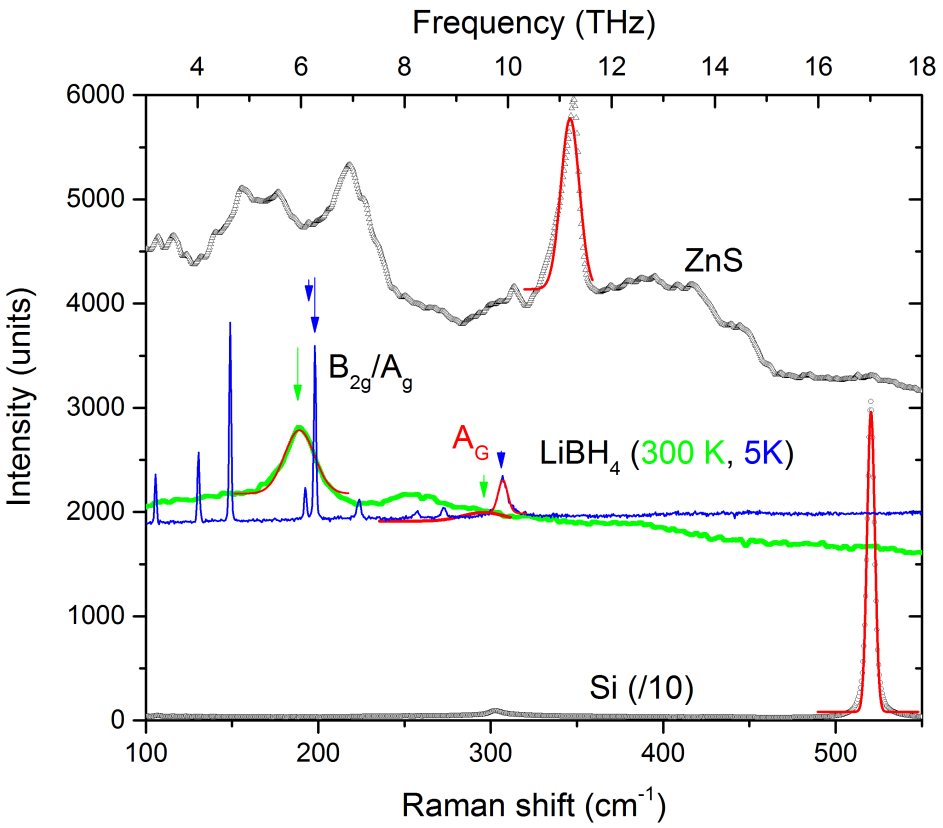

Figure 4.18: Raman measurements for the determination of the absolute Raman polarizabilities of lithium borohydride. The Raman spectra of ZnS, Si and $LiBH_4$(300 K) were all taken in the same calibrated Raman spectrometer. The known Raman polarizabilities of ZnS and Si were used to determine the absolute Raman polarizability of the ~ 190 cm^{-1} B_{2g}/A_g mode in $LiBH_4$ at 300 K. The Raman polarizability of the ~ 308 cm^{-1} A_g mode can be found through a comparison between the now calibrated spectrum at 300 K and the spectrum at 5 K, which was published in [RSL+08].

Inserting these numbers yields

$$q \approx 1.4 \times 10^{-3}\,\text{Å}u^{\frac{1}{2}}$$

where u is the atomic mass unit. The actual displacement of a lithium atom can be calculated with the phonon eigenvector $\mathbf{l}$

$$x_{Li} = \frac{1}{\sqrt{m_{Li}}}|\mathbf{l}_{Li}|q \approx 2 \times 10^{-4}\,\text{Å}$$

The mass of lithium was taken as $m_{Li} = 6.94$ u. The phonon eigenvector was taken from [RSL+08] as

$$\mathbf{l}_{Li} \approx (0.26, 0, -0.22)$$
$$|\mathbf{l}_{Li}| \approx 0.35$$

4.3.2 Bethe-Salpeter Approach

The Bethe-Salpeter equation allows for the accurate description of optical and x-ray spectra (see Sec. 2.2) In the case of lithium borohydride BSE shows excellent agreement with our experimental spectrum in Fig. 4.11. BSE works within the Born-Oppenheimer approximation (BOA), which means that the nuclear positions $\mathbf{R}$ are free parameters of BSE and all output variables can be seen as functions of the nuclear positions as well, e.g. the dielectric function $\varepsilon_2(\omega) = \varepsilon_2(\omega, \mathbf{R})$. The response with respect to a phonon mode i can be calculated with

$$\frac{\partial \varepsilon_2(\omega)}{\partial q_i} = \frac{\partial \varepsilon_2(\omega, \mathbf{R}_0 + q_i \mathbf{l}_i)}{\partial q_i},$$

where $\mathbf{R}_0$ is the known ground state configuration and $\mathbf{l}_i$ is the phonon eigenvector of mode i. For the phonon eigenvector we use a literature value published by Racu. et. al. [RSL$^+$08], which was calculated with DFT. We determined the derivative with a fourth order finite difference formula

$$\begin{aligned}\frac{\partial \varepsilon_2}{\partial q_i} = \frac{1}{\delta q}\Bigg(&-\frac{1}{12}\varepsilon_2(\mathbf{R}_0 + 2\delta q \mathbf{l}_i) + \frac{2}{3}\varepsilon_2(\mathbf{R}_0 + 1\delta q \mathbf{l}_i) \\ &-\frac{2}{3}\varepsilon_2(\mathbf{R}_0 - \delta q \mathbf{l}_i) + \frac{1}{12}\varepsilon_2(\mathbf{R}_0 - 2\delta q \mathbf{l}_i)\Bigg),\end{aligned}$$

for which we used the steps $q = \{-0.2, -0.1, 0, 0.1, 0.2\}$, i.e. $\delta q = 0.1$.

In Fig. 4.19 the linearized change of the dielectric function for $\delta q = -1, 0, 1$ is shown. Positive δq leads to a red shift of the exciton peak and an overall redistribution of oscillator strength from the peak to the post edge region, whereas negative δq leads to a blue shift of the peak and a redistribution from the post edge to the peak.

With this result at hand we can compare it to an experimental transient spectrum (Fig. 4.17). For a comparison with the experiment, we calculate the chance of absorption according to

$$\Delta A_{\text{bse}}(\omega) = d\frac{\omega}{c}\frac{\partial \varepsilon_2(\omega)}{\partial q_i}\delta q,$$

where d is the thickness of the sample and δq the amplitude of the Raman mode in the experiment. The sample thickness was determined as $d = 0.75\,\mu\text{m}$ from comparison between the linear absorption spectrum from BSE and experiment (see Fig. 4.11) The fit of both minima and maxima (yellow and blue line) yields $\delta q = 5(1) \times 10^{-4}\,\text{Å}\text{u}^{\frac{1}{2}}$. This translates to a displacement of lithium atoms of

$$|\mathbf{x}_{\text{Li}}| = 7(1) \times 10^{-5}\,\text{Å}$$

This value is in good agreement to the prediction from absolute Raman measurements and impulsive Raman theory, which yields a by a factor of two larger displacement. The latter value exhibits a relatively high uncertainty as it depends on the electric field strength within the sample, which is relatively difficult to determine accurately. The accuracy of the BSE approach depends on the validity of BSE for small displacements of nuclei, which has so far not been explored.

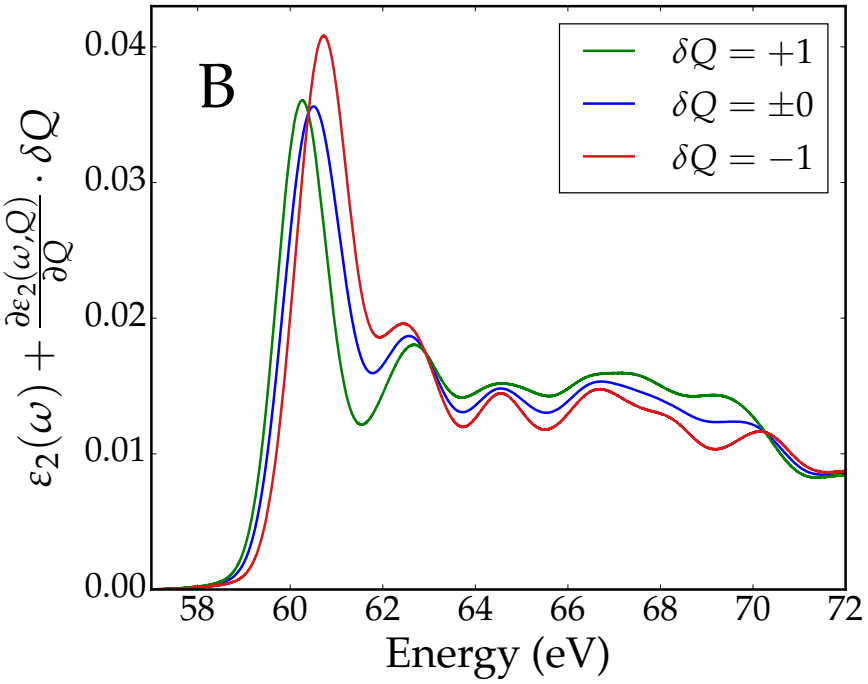

Figure 4.19: Dielectric function as a function of phonon displacement according to BSE and calculated by Eric Shirley. Here a linearized spectrum with respect to the displacement and a large displacement of $\delta Q \pm 1$ is shown for better clarity. The spectrum shows a red shift of the main peak and increase of post edge absorption for positive displacements and a blue shift and increase of the main peak and decrease of post edge absorption for negative displacements.

All in all we must conclude that we can only determine the absolute displacement in an order of magnitude fashion, where both values agree and yield a displacement in the order of 10^{-4}Å. Note that the radius of a lithium nucleus is only 2.5×10^{-5} Å, i.e. the displacement is only in the order of 5 nuclear radii.

4.4 Comparison between Results from X-ray Diffraction and XUV Absorption Spectroscopy

The transient x-ray absorption measurements presented in this chapter allow for a direct observation of coherent phonons, i.e. nuclear motion in real time. The driving mechanism of this excitation, the induced polarization, has been described using Raman polarizability. The interaction between light and electrons and electrons and nuclei is described by a term

$$H_{int} \propto \mathbf{E} \frac{\partial \alpha}{\partial q_i} \mathbf{E} q$$

While this method is quantitatively successful, the physics of the coupling remains unclear as it is hidden in the empirical Raman polarizability. In this section we will use time resolved x-ray diffraction data on lithium borohydride from Stingl. et. al. [SZF+12] to

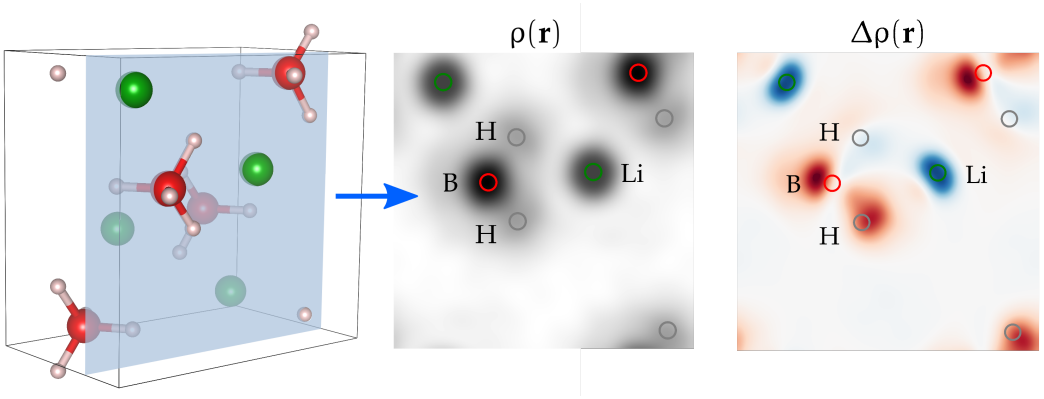

Figure 4.20: Static and transient electronic structure of lithium borohydride. **(Left)** Lithium borohydride unit cell with a $y = 1/2$ plane. All lithium and boron atoms lie in this or the equivalent $y = \frac{3}{4}$ plane and the 10 THz phonon, which was observed in this thesis, lies in this plane as well, i.e. the phonon eigenvector has no y component. **(Center)** Static electron density in the $y = 1/2$ plane as measured from x-ray diffraction and with Copper K_α spatial resolution. **(Right)** Transient electron density as measured with time resolved x-ray diffraction [SZF+12] upon non resonant excitation with a NIR pulse. The transient density shows an asymmetric decrease of charge density on the borohydride group and an approximately symmetric increase on the lithium atoms.

shed a new light on the microscopic details of Raman scattering. The x-ray diffraction experiment was performed under very similar conditions as the experiments in this thesis, e.g. at room temperature and with the same pump wavelength and similar intensity.Time resolved x-ray diffraction yields a transient electron density, i.e. the change in electron density due to the pump beam. Stingl et. al. [SZF+12] observed an instantaneous change in electron density, i.e. the change directly followed the intensity profile of the pump. They observed an electron transfer from the BH_4 anion to the Li cation, which means a decrease in ionicity. This is an extremely interesting finding as beforehand it was unclear whether the intra molecular polarizability of BH_4 tetrahedrons or intermolecular charge transfer between lithium and BH_4 would dominate the total polarizability. We will use this transient electron density to calculate the forces onto the nuclei, which is fundamentally the driving process of all Raman scattering. In Fig. 4.20 the unit cell of lithium borohydride is shown with a $y = 1/2$, hkl = 010 plane. The observed Raman mode operates completely within this plane, i.e. its eigenvector has zero y component. The center panel shows the steady state electron density (within the limited spatial resolution of the x-ray diffraction experiment) and the right panel the observed change in electron density at zero delay. Blue depicts and increase in electron density and red a decrease. The electron transfer from BH_4 tetrahedron to lithium is clearly visible as BH_4 exhibits only losses and lithium only gains. Note that the new charge around lithium is centered with respect to the nucleus and roughly symmetrical as one would expect for a simple ion. Around the BH_4 tetrahedron the transient density is highly asymmetric and not centered on the boron nucleus.

The transient Coulomb potential is defined by the Poisson equation

$$-\nabla^2 \Delta\phi_{tr} = \varepsilon_0 \delta\rho,$$

which can in the periodic case best be solved in k-space according to Eq. (2.14) and is

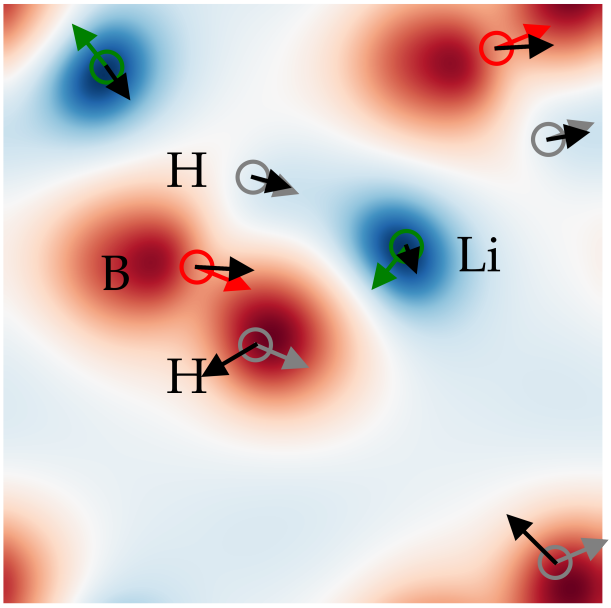

Figure 4.21: Transient Coulomb potential calculated with the transient electron density from [SZF+12] and calculated with Eq. (2.14) and Coulomb forces calculated with Eq. (2.15). The calculated forces (black arrows) show a nice overlap with the phonon eigenvector (colored arrows). In other words this confirms that irradiation with a NIR pulse of lithium borohydride leads to excitation of the A_g 10 THz Raman mode due to the electronic rearrangement caused by the femtosecond pulse and the resulting forces on the nuclei.

shown in Fig. 4.21. The forces (black arrows) onto the nuclei, which were calculated with Eq. (2.15). The transient Coulomb potential and derived forces show a strong acceleration of the boron nucleus in the direction of the phonon eigenvector (B: red, Li: green, H: gray arrows).

4.5 Optically induced Electron Transfer in Lithium Borohydride

In Sec. 4.4 we presented the transient electron density in $LiBH_4$ upon optical non-resonant excitation and as measured by Stingl et. al. [SZF+12]. In this section we will explore the underlying physics in more detail, especially the microscopic reasons for the electron transfer from the BH_4^- tetrahedron to the Li^+ ion.

As a theoretical framework we use a description of the (electronic) many-body problem as a problem of effectively non-interacting quasi-particles, as for example in DFT or the GW approximation. The single-particle properties are, within this framework, fully described by the band structure and the respective single-particle states $|\phi_i\rangle$. The wave function is the slater-determinant of the occupied single particle states and the density is simply

given by a sum over the occupied states

$$\rho(\mathbf{r}) = \sum_{i=1}^{N} |\phi_i(\mathbf{r})|^2$$

The basis of our analysis, the unperturbed system, is the standard solid state Hamiltonian in the respective approximation. The external electric field of the light wave constitutes the perturbation through a time dependent potential. The perturbed system can still be described in the basis of the single particle wave functions $|\phi_i\rangle$ of the unperturbed system. In this case the full many-body wave functions is time dependent, which translates in the non-interacting particle approximation to time dependent amplitudes of the single particle wave functions. As a very simple approximation we can reduce the whole problem to a single particle in the Hilbert space of one valence and one conduction band, i.e. a HOMO-LUMO two-level system as depicted in Fig. 4.22. The $LiBH_4$ valence band states are centered on the BH_4^- tetrahedrons due $LiBH_4$'s ionic chemistry. Many of the the conduction bands on the other hand show equal density on the lithium ion and the borohydride group. Without perturbation the ground state of our simplified system is given by the valence band state

$$|\psi\rangle = |\psi_{vb}\rangle$$

The spatially distorted potential (dotted black curve in Fig. 4.22) leads to a time dependent wave function, which is a superposition of valence and conduction band states (green curve in Fig. 4.22)

$$|\psi\rangle(t) = \alpha(t)|\psi_{vb}\rangle + \beta(t)|\psi_{cb}\rangle$$

with time dependent amplitudes $\alpha(t)$ and $\beta(t)$. This superposition state displays an increased density on the Lithium ion independent of the phase relation of the amplitudes, due to the almost vanishing density on the lithium ion of the valence state. This means that from these consideration we expect a electron transfer from the BH_4^- tetrahedron to the Li^+ ion in the case of a non-resonant external (linear) potential. In the more complex problem of all valence band electrons and with the inclusion of more than one conduction band state the qualitative result still holds as the (valence) ground state is made purely out of wave function with almost no density on the lithium ions. If we now form any superposition of various valence and conduction band wave functions they will show an increased density on the lithium ions.

In this context these superpositions are often labeled as virtual states. The reasoning behind this term is that, in the case of non-resonant excitation frequencies, the system evolves from the ground state into this transient state and back into the ground state, when the excitation is over. The process can be understood adiabatically, i.e. electrons do not change occupation of states but the states change through the external perturbation.

[7] The lowest conduction band wave functions can be divided into two groups, namely anti-bonding BH_4 states and bonding Li 2p/BH_4 states. While the former still exhibits very little density on the Lithium ion, the latter does.

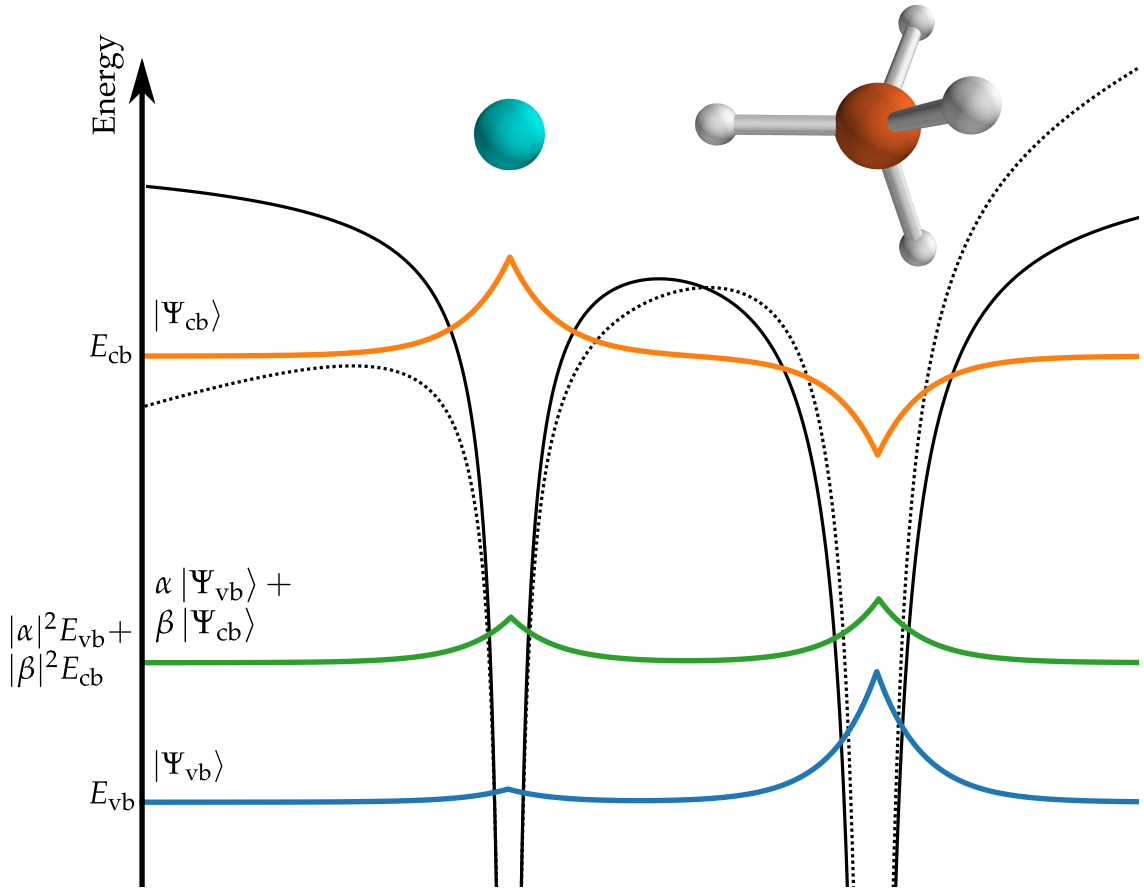

Figure 4.22: Schematic representation of the microscopic physics of the electron transfer upon non-resonant strong-field excitation in Lithium borohydride as measured and published in [SZF+12]. This figure is redrawn with slight variation from Fig. 1 in [SZF+12]. Solid and dotted black curves are the ionic (Coulomb) potentials without and with external (linear) perturbation from the external light field. All the valence band wave functions (see Fig. 4.4) are strongly localized on the BH_4^- tetrahedrons, which corresponds to the strongly ionic nature of $LiBH_4$'s chemistry. The Li^+ ions on the other hand exhibit very little density and in result $LiBH_4$ is an almost completely ionic compound. Many of the conduction band wave functions [7]on the other hand show a comparable density on the Lithium ion (see the density of states in Fig. 4.5 and iso-surface plots of the two lowest conduction band states in Fig. 4.23).

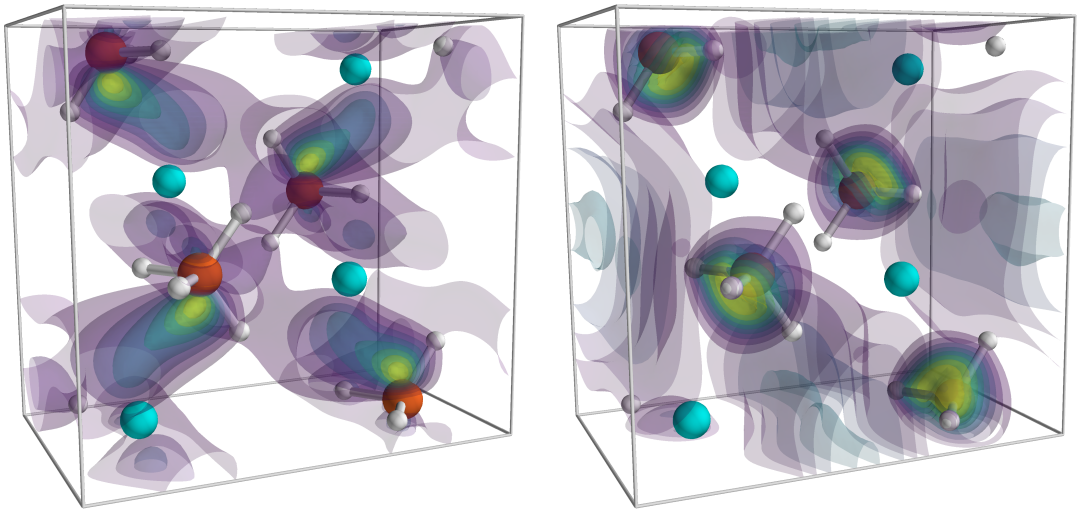

Figure 4.23: Iso-surface plot of the probability density of lowest (left) and second lowest (right) (Kohn-Sham) wave function of Lithium borohydride as calculated with Quantum-Espresso. The lowest conduction band state (left) is a bonding superposition of Li 2p and BH_4 sp^3 states. It displays significant density on the lithium ion and is one of the states, which are responsible for the electron transfer upon non-resonant excitation. The second lowest conduction band state (right) is an anti-bonding superposition within the BH_4 sp^3 states. The anti-bonding BH_4^- states are very similar to the HOMO states of Methane.

4.6 New Insights into the Raman process

The Raman effect, be it the stationary or impulsive stimulated one, is commonly understood through macroscopic, effective and often empirical parameters and theories. Here the induced polarization, whose effect on the nuclei is responsible for the Raman excitation, is described by a local and instantaneous electronic susceptibility $\chi_0(\mathbf{r}, \mathbf{r}', t - t') = \chi\ \delta(\mathbf{r} - \mathbf{r}')\delta(t - t')$ (or polarizability α for molecules). This leads to a spatially averaged polarization, which can be described by a single number χ_0, instead of the highly complex induced change of the electron density, i.e. transient electron density, which describes the exact electronic response upon the external field.

Both common descriptions, namely the empirical and the full quantum mechanical treatment (see Sec. 2.4), use these simplifications. The empirical description is build upon a linearized Taylor expansion of the electric susceptibility with respect to the vibrational coordinates q_i, i.e. $\frac{\partial \chi}{\partial q_i}$. It is typically introduced with the statement that the polarizability depends on the nuclear configuration but from the viewpoint of the nuclei one could equally well state that the configuration of the nuclei depend on the polarization. The full quantum mechanical treatment is a second order time dependent perturbation theory approach. Here the exact shape of the induced polarization is indirectly considered through the perturbed wave function $\left|\Psi^{(1)}\right\rangle$. The Raman scattering is described through Fermi's golden rule by a transition dipole moment d_{fi} (see Eq. (2.8)), which condenses the whole complicated process into a single parameter, the so called so called Raman transition polarizability tensor α_{fi} (see Eq. (2.9)). The excited state properties such as the perturbed wave function or the transient electron density as well as derived quantities such as α_{fi} are described through ground state properties, i.e. by sums over ground state wave functions.

In this thesis I present new insights into the Raman process, which are based on an observation of the exact spatial shape of the induced polarization, i.e. the transient electron density, and the direct time domain observation of the excited nuclear motion. The transient electron density upon non-resonant excitation with a near infrared pump pulse is known for lithium borohydride from a time resolved x-ray diffraction study [SZF+12]. With the transient electron density (see Fig. 4.20) we calculated the transient Coulomb potential (see Fig. 4.21) from which we derived the Lorentz force, which acts on the nuclei. This is a fascinating way to study the Raman effect as this approach directly yields the forces that act on the nuclei and are responsible for the Raman effect. The Lorentz force accelerates the nuclei, which start to oscillate spatially with various Raman modes. In a x-ray absorption experiment we observed the effect of the nuclear motion from a certain A_g 10 THz mode onto the absorption spectrum of the material. The K-edge absorption spectrum of the lithium atom under study is sensitive to its chemical environment, which is modulated by the harmonically oscillating lithium-borohydride distance. Fig. 4.24

[8] For non-resonant pulses the electron density returns into its ground state, whereas for resonant pulses it settles into a excited state. Excited states are rather long lived and spawn a multitude of other effects that would overshadow the impulsive Raman response.

depicts a schematic overview of the whole process with lithium borohydride as exemplary material.

a) The system undergoes zero point motion and is in its electronic ground state before the near infrared excitation.

b) The pump pulse distorts the electron density with its electric field. In the case of lithium borohydride a charge transfer from lithium cation to borohydride anion occurs. The distorted electron density exerts a force $\mathbf{F}_{\mathrm{Raman}}$ onto the nuclei, which changes their momentum.

c) The charge transfer is reversed when the incident pump pulse has passed. The electron density is back in its ground state as the process is fully reversible.

d) The nuclei oscillate harmonically in space due to the momentum transfer. All Raman active modes with a vibrational period T_{vib} shorter than the period of the pump light period are excited.

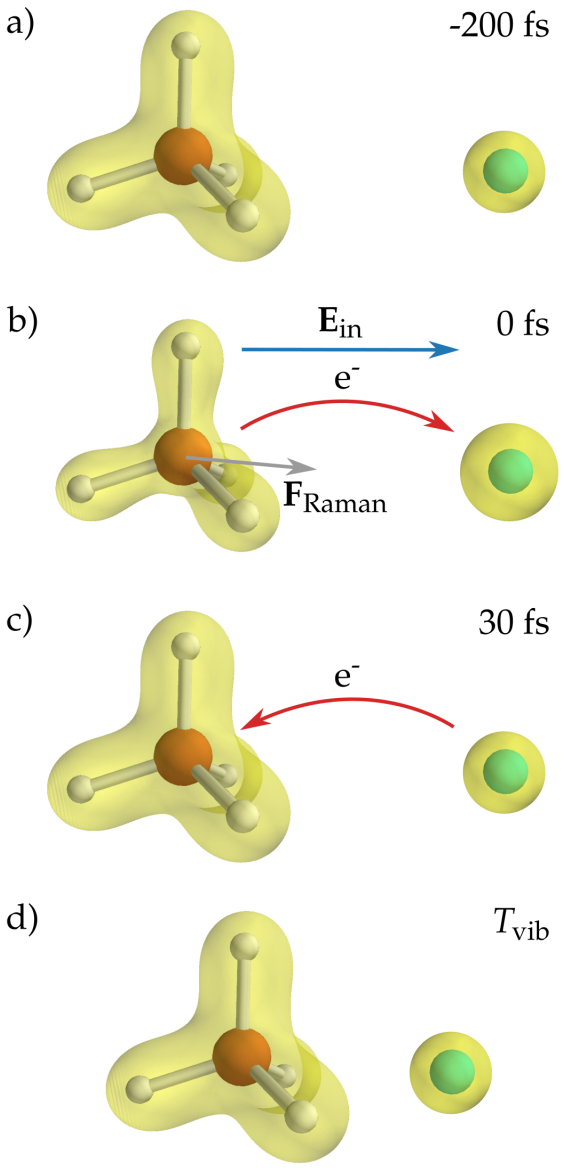

Figure 4.24: Sketch of the microscopic dynamics of the impulsive stimulated Raman process. a) The atoms or molecular building blocks, here exemplary the lithium cation and tetrahedronal BH_4 cation in lithium borohydride, are vibrationally at rest in their electronic ground state before the short non-resonant pump pulse excites the sample. The electron density is depicted by the yellow iso-surface. b) The pump pulse exerts a force onto the electron density though its electric field. The material responds through a distortion of the electron density. In the case of lithium borohydride an electron transfer from the BH_4 tetrahedron to the lithium cation takes place, which is a decrease of ionicity. The macroscopic average of this response is described by the electric susceptibility or the refractive index, i.e. the optical properties are directly related to it. The distorted electron density exerts a coulomb force $\mathbf{F}_{\text{Raman}}$ on the nuclei, in the case of lithium borohydride especially on the boron nucleus because of the anisotropic transient electron density on the tetrahedron. c) After the pump pulse the electron density returns into its steady state[8]. In this case the charge transfer is reversed. d) While the pump pulse was present the nuclei were accelerated through the distorted electron density. This leads to vibrational excitation, i.e. nuclear motion, of in general all nuclei. The various Raman active vibrational modes oscillate according to their vibrational period T_{vib}.

5 Conclusions

This thesis explores the subtle interplay between electronic and nuclear excitation in the Raman effect with time resolved extreme ultraviolet (XUV) absorption spectroscopy. Coherent stimulated Raman scattering, the type of Raman interaction we induce, is a variant of the well known Raman scattering, where a sufficiently short pulse excites nuclear vibrations coherently, i.e. with actual displacement of the nuclei. In standard Raman scattering, due to its incoherent, spontaneous nature, there is no displacement of nuclei. We were able to observe nuclear displacements as small as 10^{-4} Å in real time by their effect on the XUV absorption spectrum. Specifically we studied non-resonant near infrared (NIR) pump XUV probe absorption spectroscopy on lithium borohydride ($LiBH_4$).

Lithium borohydride is an ionic insulator with ~ 7 eV band gap, which is more than four times the photon energy of the pump pulse, which excludes direct excitations of electrons through multi-photon absorption into the conduction band. The exact electronic response of lithium borohydride upon excitation with a NIR pump pulse has been studied by Stingl et. al [SZF+12] with time resolved x-ray diffraction. They observed a quasi-instantaneous electron transfer from BH_4^- anion to Li cation, which is responsible for the relatively large dielectric function, compared to the intra-molecular polarizability of the BH_4^- group alone. This ultrafast induced polarization, or in other words transient electron density, exerts a force onto the nuclei, which are accelerated.

In the XUV absorption experiments in this thesis we concentrate on the Lithium K-edge absorption spectrum around 60 eV, which consists of a strong excitonic peak at the onset of absorption and a plateau at higher energies. Upon excitation with a NIR pulse we observe oscillatory changes in the absorption spectrum with a frequency of 10 THz, which we identify as the effect of coherent phonon excitations of an external A_g phonon mode. The coherent oscillation changes the distance between Li^+ anions and BH_4^- cations, which modifies the electronic environment around the Li anion. XUV absorption spectroscopy, especially x-ray absorption near edge spectroscopy (XANES), is highly sensitive to such changes of the chemical environment around the absorbing atom. We use two different approaches to derive the absolute displacement, which are observed in the experiment.

The first approach is to measure the absolute Raman polarizability in a calibrated Raman spectrometer with an otherwise standard Raman scattering experiment. We determine the Raman polarizability of the mode under study as $\frac{\partial \alpha}{\partial q} = 1\,\text{Å}u^{-\frac{1}{2}}$. The theory of stimulated impulsive coherent Raman can be used to determine a displacement of 2×10^{-4} Å for the lithium nuclei with the pump field inside the sample and Raman polarizability as

input parameters. This is a forward approach, which means that it predicts the nuclear displacement from the experimental conditions.

The second approach is to use the theory of the Bethe-Salpeter equation (BSE) to predict the absorption spectrum at the lithium K-edge and the change with respect to the nuclear displacement. The calculated change of the dielectric function with respect to the nuclear displacement, i.e. $\frac{\partial \varepsilon_2}{\partial q}$, can be compared to the measured change in absorption, which yields 7×10^{-5} Å. This is a backward approach as it determines the nuclear displacement from the outcome of the experiment. Both forward and backward approach yield a displacement of the lithium nucleus in the order of 10^{-4} Å.

The transient electron density from the time resolved x-ray diffraction experiment can be used to calculate a transient coulomb potential and the forces on the nuclei due to the induced electronic polarization. Those forces are responsible for the whole Raman process, so in principle the Raman amplitudes can be derived from the transient electron density if one knows the spatial shape of the phonon modes, i.e. their eigenvectors. The derived forces fit well with the 10 THz A_g Raman mode, which indicates a strong excitation of this mode as indeed observed in the experiment.

These results allow for a fascinating new insight into Raman scattering as they connect a direct observation of the driving mechanism, the induced polarization, with a direct observation of the outcome the oscillatory nuclear displacement. With XUV absorption spectroscopy nuclear displacements in the order of 10^{-4} Å were resolved with sub picosecond accuracy in the time domain.

6 Zusammenfassung

Diese Arbeit untersucht den subtilen Zusammenhang von elektronischer und nukleare Anregung beim Raman-Effekt mit der Methode der zeitaufgelösten harten UV-Spektroskopie. Wir verwenden kohärente stimulierte Raman-Streuung, ein Spezialfall der weit verbreiteten normalen Raman-Streuung. Bei dieser regt ein hinreichend kurzer kohärenter Lichtimpuls Schwingungen der Kerne an, bei denen die Kerne messbar ausgelenkt werden, wohingegen die Auslenkungen bei normaler Raman-Streuung, wegen deren inkohärenten spontanen Natur, nicht messbar sind. Wir konnten Auslenkung kleiner als 10^{-4} Å in Echtzeit durch ihren Effekt auf das harte UV-Spektrum nachweisen. Diese Ergebnisse konnten mit Lithiumborhydrid als Probe und nicht-resonanter naher Infrarotstrahlung als Anrege-und harter UV-Strahlung als Abfrageimpuls erzielt werden.

Lithiumborhydrid ist ein ionischer Isolator mit etwa 7 eV Bandlücke. Die Bandlücke beträgt somit mehr als vier mal die Photonenenergie des Anregeimpulses, was eine direkte Anregung von Elektronen in das Leitungsband durch Mehrphotonenabsorption ausschließt. Die genaue elektronische Reaktion Lithiumborhydrids auf Anregung durch nahes Infrarotlicht wurde von Stingl et. al. [SZF$^+$12] mit zeitaufgelöster Röntgenbeugung untersucht. Stingl et. al. wiesen einen quasi-instantanen Elektronentransfer vom BH_4^- Anion zum Lithium Kation nach, welcher für die hohe dielektrische Konstante im Vergleich zur puren molekularen Polarisierbarkeit des BH_4^- Tetraeders verantwortlich ist. Diese ultrakurze induzierte Polarisation, oder transiente Elektronendichte, übt eine Kraft auf die Kerne aus, welche dadurch beschleunigt werden und zu schwingen beginnen.

Zum Nachweis dieses Prozesses verwenden wir harte UV-Absorptionsspektroskopie an der Lithium K-Kante von Lithiumborhydrid bei 60 eV. Das Absorptionsspektrum besteht aus einem starken exzitonischen Anteil zu Beginn der Absorption und einem Plateau bei höheren Energien. Bei Anregung durch einen NIR-Impuls beobachteten wir eine oszillatorische Änderung des Absorptionsspektrums mit einer Frequenz von 10 THz, was wir der Modulation der interatomaren Abständen durch kohärente Phononen, und die damit einhergehende Modulation der chemischen Umgebung des absorbierenden Atoms, zuschreiben. Harte UV-Spektroskopie, insbesondere bei niedrigen Energien und nahe der Kante (engl.: x-ray absorption near edge spectroscopy (XANES)), ist hoch sensitiv auf die chemische Umgebung des jeweiligen absorbierenden Atoms. Wir verwenden zwei Ansätze um die nuklearen Auslenkungen quantitativ zu bestimmen.

Erstens messen wir die absolute Raman-Polarisierbarkeit in einem kalibrierten Raman-Spektrometer aber sonst normalen Raman-Streuungs-Aufbau und können für die im Schwingungsmode, welche in dieser Arbeit untersucht wird, diese zu $\frac{\partial \alpha}{\partial q} = 1\,\text{Å}u^{-\frac{1}{2}}$ bestimmen. Daraus folgt unter den Bedingung in unserem Experiment eine Auslenkung

von etwa 2×10^{-4} Å. Bei dieser Methode handelt es sich um einen Vorwärtsansatz, d.h. die Auslenkung der Kerne wird aus Materialkonstanten und experimentellen Bedingungen zusammen mit Theorie vorhergesagt und nicht direkt gemessen.

Zweitens verwenden wir die sog. Bethe-Salpeter Gleichung als Rahmenwerk um das Lithium-Absorptionsspektrum als Funktion der nuklearen Koordinaten zu berechnen. Die berechnete Änderung der dielektrischen Funktion, d.h. $\frac{\partial \varepsilon_2}{\partial q}$, kann mit der gemessenen Änderung der Absorption verglichen werden und daraus die Auslenkung berechnet werden. Dies ergab 7×10^{-5} Å. Bei dieser Methode handelt es sich um einen Rückwärtsansatz, welcher die Auslenkungen der Kerne aus den gemessenen Daten zurückrechnet. Beide unabhängigen Ansätze ergeben Auslenkungen in der Größenordnung von 10^{-4} Å.

Zusätzlich verwenden wir die transiente Elektronendichte aus den Röntgenbeugungsergebnissen von Stingl et. al. [SZF+12] um daraus ein transientes Coulomb-Potential und transiente Coulomb-Kräfte zu berechnen. Diese Kräfte initiieren den Raman-Prozess ausschließlich und deshalb könnten aus ihnen im Prinzip die relative Stärke der Moden im Raman-Spektrum berechnet werden, falls die räumliche Form der Moden, d.h. deren Eigenvektoren, bekannt sind. Die in dieser Arbeit berechneten Kräfte passen gut zu der 10 THz Mode, was auf eine stark Anregung ebendieser hindeutet, was im Experiment nachgewiesen werden konnte.

Zusammen erlauben diese Resultate einen faszinierenden, neuen Einblick in die mikroskopische Natur des Raman-Effekts. Sie verbinden einen direkten Nachweis des antreibenden Mechanismus, der induzierten Polarisation, mit einer direkten Beobachtung des Resultats, die oszillatorische Auslenkung der Kerne. Dabei konnten mit harter UV-Spektroskopie nukleare Auslenkungen in der Größenordnung von 10^{-4} Å mit Subpicosekundenzeitauflösung aufgelöst werden.

Bibliography

[AFS+11] Aggarwal, R. L., L. W. Farrar, S. K. Saikin, A. Aspuru-Guzik, M. Stopa, and D. L. Polla: *Measurement of the absolute Raman cross section of the optical phonon in silicon*. Solid State Communications, 151(7):553–556, April 2011.

[ARBC+05] Audebert, P., P. Renaudin, S. Bastiani-Ceccotti, J. P. Geindre, C. Chenais-Popovics, S. Tzortzakis, V. Nagels-Silvert, R. Shepherd, I. Matsushima, S. Gary, F. Girard, O. Peyrusse, and J. C. Gauthier: *Picosecond Time-Resolved X-Ray Absorption Spectroscopy of Ultrafast Aluminum Plasmas*. Physical Review Letters, 94(2):025004, January 2005.

[AT77] Andrews, D. L. and T. Thirunamachandran: *On three-dimensional rotational averages*. The Journal of Chemical Physics, 67(11):5026–5033, December 1977.

[BB13] Bragg, W. H. and W. L. Bragg: *The structure of the diamond*. Nature, 91:557, 1913.

[BJS+07] Beaud, P., S. L. Johnson, A. Streun, R. Abela, D. Abramsohn, D. Grolimund, F. Krasniqi, T. Schmidt, V. Schlott, and G. Ingold: *Spatiotemporal Stability of a Femtosecond Hard–X-Ray Undulator Source Studied by Control of Coherent Optical Phonons*. Physical Review Letters, 99(17):174801, October 2007.

[BL16] Bokhoven, Jeroen A. van and Carlo Lamberti: *X-Ray Absorption and X-Ray Emission Spectroscopy: Theory and Applications*. John Wiley & Sons, January 2016, ISBN 978-1-118-84428-1. Google-Books-ID: 0dBkCwAAQBAJ.

[BMP+09] Bressler, Ch, C. Milne, V. T. Pham, A. ElNahhas, R. M. van der Veen, W. Gawelda, S. Johnson, P. Beaud, D. Grolimund, M. Kaiser, C. N. Borca, G. Ingold, R. Abela, and M. Chergui: *Femtosecond XANES Study of the Light-Induced Spin Crossover Dynamics in an Iron(II) Complex*. Science, 323(5913):489–492, January 2009.

[Bra13a] Bragg, W. L.: *The Diffraction of Short Electromagnetic Waves by a Crystal*. Scientia, 23(45):153, 1913.

[Bra13b] Bragg, W. L.: *The structure of some crystals as indicated by their diffraction of X-rays*. Proceedings of the Royal Society of London. Series A, 89(610):248–277, 1913.

[Bra15] Bragg, William Henry: *IX. Bakerian Lecture.— X-rays and crystal structure*. Phil. Trans. R. Soc. Lond. A, 215(523-537):253–274, January 1915.

[BZG+04] Bargheer, M., N. Zhavoronkov, Y. Gritsai, J. C. Woo, D. S. Kim, M. Woerner, and T. Elsaesser: *Coherent Atomic Motions in a Nanostructure Studied by Femtosecond X-ray Diffraction*. Science, 306(5702):1771–1773, December 2004.

[CC76] Chelikowsky, James R. and Marvin L. Cohen: *Nonlocal pseudopotential calculations for the electronic structure of eleven diamond and zinc-blende semiconductors*. Physical Review B, 14(2):556–582, July 1976.

[CCF+04] Cavalleri, A., H. H. W. Chong, S. Fourmaux, T. E. Glover, P. A. Heimann, J. C. Kieffer, B. S. Mun, H. A. Padmore, and R. W. Schoenlein: *Picosecond soft x-ray absorption measurement of the photoinduced insulator-to-metal transition in vo2*. Physical Review B, 69(15):153106, April 2004.

[CM88] Chesnoy, J. and A. Mokhtari: *Resonant impulsive-stimulated Raman scattering on malachite green*. Physical Review A, 38(7):3566–3576, October 1988.

[CMU+07] Cavalieri, A. L., N. Müller, Th Uphues, V. S. Yakovlev, A. Baltuska, B. Horvath, B. Schmidt, L. Blümel, R. Holzwarth, S. Hendel, M. Drescher, U. Kleineberg, P. M. Echenique, R. Kienberger, F. Krausz, and U. Heinzmann: *Attosecond spectroscopy in condensed matter*. Nature, 449(7165):1029–1032, 2007.

[Cor93] Corkum, P. B.: *Plasma perspective on strong field multiphoton ionization*. Physical Review Letters, 71(13):1994–1997, September 1993.

[CSB+00] Cavalleri, A., C. W. Siders, F. L. H. Brown, D. M. Leitner, C. Tóth, J. A. Squier, C. P. J. Barty, K. R. Wilson, K. Sokolowski-Tinten, M. Horn von Hoegen, D. von der Linde, and M. Kammler: *Anharmonic Lattice Dynamics in Germanium Measured with Ultrafast X-Ray Diffraction*. Physical Review Letters, 85(3):586–589, July 2000.

[CSG+99] Chin, A. H., R. W. Schoenlein, T. E. Glover, P. Balling, W. P. Leemans, and C. V. Shank: *Ultrafast Structural Dynamics in InSb Probed by Time-Resolved X-Ray Diffraction*. Physical Review Letters, 83(2):336–339, July 1999.

[CTS+01] Cavalleri, A., Cs. Tóth, C. W. Siders, J. A. Squier, F. Ráksi, P. Forget, and J. C. Kieffer: *Femtosecond Structural Dynamics in vo2 during an Ultrafast Solid-Solid Phase Transition*. Physical Review Letters, 87(23):237401, November 2001.

[CVC82] Calleja, J. M., H. Vogt, and M. Cardona: *Absolute Raman scattering efficiencies of some zincblende and fluorite-type materials*. Philosophical Magazine A, 45(2):239–254, February 1982.

[Czy16] Czycholl, Gerd: *Theoretische Festkörperphysik Band 1: Grundlagen: Phononen und Elektronen in Kristallen*. Springer-Verlag Berlin Heidelberg, 2016, ISBN 978-3-662-47140-1.

[Daw67] Dawson, B.: *The covalent bond in diamond*. Proc. R. Soc. Lond. A, 298(1454):264–288, May 1967.

[dB13] Broglie, Maurice de: *Sur une nouveau procédé permettant d'obtenir la photographie des spectres de raies des rayons Röntgen*. Comptes Rendus, 157, 1913.

[Der02] Derek A. Long: *The Raman Effect: A Unified Treatment of the Theory of Raman Scattering by Molecules*. John Wiley & Sons Ltd, 2002, ISBN 0-471-49028-8.

[DRN94] Dhar, Lisa, John A. Rogers, and Keith A. Nelson: *Time-resolved vibrational spectroscopy in the impulsive limit*. Chemical Reviews, 94(1):157–193, January 1994.

[DSFI+85] De Silvestri, S., J. G. Fujimoto, E. P. Ippen, Edward B. Gamble, Leah Ruby Williams, and Keith A. Nelson: *Femtosecond time-resolved measurements of optic phonon dephasing by impulsive stimulated raman scattering in a-perylene crystal from 20 to 300 K*. Chemical Physics Letters, 116(2):146–152, May 1985.

[Dua25] Duane, William: *The Calculation of the X-Ray Diffracting Power at Points in a Crystal*. Proceedings of the National Academy of Sciences, 11(8):489–493, August 1925.

[DWN92] Dougherty, Thomas P., Gary P. Wiederrecht, and Keith A. Nelson: *Impulsive stimulated Raman scattering experiments in the polariton regime*. JOSA B, 9(12):2179–2189, December 1992.

[FCC08] Filinchuk, Yaroslav, Dmitry Chernyshov, and Radovan Cerny: *Lightest Borohydride Probed by Synchrotron X-ray Diffraction: Experiment Calls for a New Theoretical Revision*. The Journal of Physical Chemistry C, 112(28):10579–10584, July 2008.

[FFH+05] Föhlisch, A., P. Feulner, F. Hennies, A. Fink, D. Menzel, D. Sanchez-Portal, P. M. Echenique, and W. Wurth: *Direct observation of electron dynamics in the attosecond domain*. Nature, 436(7049):373–376, July 2005.

[FKL13] Friedrich, W., P. Knipping, and M. Laue: *Interferenzerscheinungen bei Röntgenstrahlen*. Annalen der Physik, 346(10):971–988, January 1913.

[FLL+88] Ferray, M., A. L'Huillier, X. F. Li, L. A. Lompre, G. Mainfray, and C. Manus: *Multiple-harmonic conversion of 1064 nm radiation in rare gases*. Journal of Physics B: Atomic, Molecular and Optical Physics, 21(3):L31, 1988.

[GBB+09] Giannozzi, Paolo, Stefano Baroni, Nicola Bonini, Matteo Calandra, Roberto Car, Carlo Cavazzoni, Davide Ceresoli, Guido L. Chiarotti, Matteo Cococcioni, Ismaila Dabo, Andrea Dal Corso, Stefano de Gironcoli, Stefano Fabris, Guido Fratesi, Ralph Gebauer, Uwe Gerstmann, Christos Gougoussis, Anton Kokalj, Michele Lazzeri, Layla Martin-Samos, Nicola Marzari, Francesco Mauri, Riccardo Mazzarello, Stefano Paolini, Alfredo Pasquarello, Lorenzo Paulatto, Carlo Sbraccia, Sandro Scandolo, Gabriele Sclauzero, Ari P. Seitsonen, Alexander Smogunov, Paolo Umari, and Renata M. Wentzcovitch: *QUANTUM ESPRESSO: a modular and open-source software project for quantum simulations of materials*. Journal of Physics: Condensed Matter, 21(39):395502, 2009.

[GBS+05] Gawelda, W., C. Bressler, M. Saes, M. Kaiser, A. N. Tarnovsky, D. Grolimund, S. L. Johnson, R. Abela, and M. Chergui: *Picosecond time-resolved x-ray absorption spectroscopy of solvated organometallic complexes*. Physica Scripta, 2005(T115):102, 2005.

[Ge04] Ge, Qingfeng: *Structure and Energetics of LiBH4 and Its Surfaces: A First-Principles Study*. The Journal of Physical Chemistry A, 108(41):8682–8690, October 2004.

[GJ14] Grenier, S. and Y. Joly: *Basics of Resonant Elastic X-ray Scattering theory*. Journal of Physics: Conference Series, 519(1):012001, 2014.

[GWS+11] Gebert, Florian, Britta Willenberg, Michiel J. van Setten, Elisa G. Bardají, Eva Roehm, Maximilian Fichtner, and Joachim Schoenes: *Polarization-dependent Raman spectroscopy of LiBH4 single crystals and Mg(BH4)2 powders*. Journal of Raman Spectroscopy, 42(9):1796–1801, 2011.

[Han31] Hanawalt, J. D.: *The Dependence of X-ray Absorption Spectra upon Chemical and Physical State*. Physical Review, 37(6):715–726, March 1931.

[Hav25] Havighurst, R. J.: *The Distribution of Diffracting Power in Sodium Chloride*. Proceedings of the National Academy of Sciences, 11(8):502–507, August 1925.

[Hav27] Havighurst, R. J.: *Electron Distribution in the Atoms of Crystals. Sodium Chloride and Lithium, Sodium and Calcium Fluorides*. Physical Review, 29(1):1–19, January 1927.

[HKK94] Haug, Hartmut, Stephen W. Koch, and Leonid V. Keldysh: *Quantum Theory of the Optical and Electronic Properties of Semiconductors*, volume 47. 1994.

[LFSK78] Laubereau, A., S. F. Fischer, K. Spanner, and W. Kaiser: *Vibrational population lifetimes of polyatomic molecules in liquids*. Chemical Physics, 31(3):335–344, July 1978.

[LIG13] LIGO Scientific Collaboration and Virgo Collaboration: *Enhanced sensitivity of the LIGO gravitational wave detector by using squeezed states of light*. Nature Photonics, 7(8):613–619, August 2013.

[LIG16] LIGO Scientific Collaboration and Virgo Collaboration: *Observation of Gravitational Waves from a Binary Black Hole Merger*. Physical Review Letters, 116(6):061102, February 2016.

[MGJ+87] McPherson, A., G. Gibson, H. Jara, U. Johann, T. S. Luk, I. A. McIntyre, K. Boyer, and C. K. Rhodes: *Studies of multiphoton production of vacuum-ultraviolet radiation in the rare gases*. JOSA B, 4(4):595–601, April 1987.

[MOT+04] Miwa, Kazutoshi, Nobuko Ohba, Shin ichi Towata, Yuko Nakamori, and Shin ichi Orimo: *First-principles study on lithium borohydride*. Physical Review B, 69(24):245120, June 2004.

[MP76] Monkhorst, Hendrik J. and James D. Pack: *Special points for Brillouin-zone integrations*. Physical Review B, 13(12):5188–5192, June 1976.

[NGL+99] Nakano, Hidetoshi, Yoshinori Goto, Peixiang Lu, Tadashi Nishikawa, and Naoshi Uesugi: *Time-resolved soft x-ray absorption spectroscopy of silicon using femtosecond laser plasma x rays*. Applied Physics Letters, 75(16):2350–2352, October 1999.

[Nor60] Nordsthand, Robert A. Van: *The Use of X-Ray K-Absorption Edges in the Study of Catalytically Active Solids*. In Eley, D. D., P. W. Selwood, and Paul B. Weisz (editors): *Advances in Catalysis*, volume 12, pages 149–187. Academic Press, January 1960.

[OB27] Oppenheimer, Robert and Max Born: *Die Quantentheorie der Moleküle*. Annalen der Physik, 84:459, 1927.

[OTPAD09] Olovsson, W, I Tanaka, P Puschnig, and C Ambrosch-Draxl: *Near-edge structures from first principles all-electron Bethe–Salpeter equation calculations*. Journal of Physics: Condensed Matter, 21(10):104205, March 2009.

[PBE96] Perdew, John P., Kieron Burke, and Matthias Ernzerhof: *Generalized Gradient Approximation Made Simple*. Physical Review Letters, 77(18):3865–3868, October 1996.

[Pla34] Placzek: *Rayleigh Streuung und Raman Effekt*, volume 6 of *Handbuch der Radiologie*. 1934.

[PLM90] Pollard, W. Thomas, Soo-Y. Lee, and Richard A. Mathies: *Wave packet theory of dynamic absorption spectra in femtosecond pump–probe experiments*. The Journal of Chemical Physics, 92(7):4012–4029, April 1990.

[PM08] Pinkerton, F. E. and M. S. Meyer: *Reversible hydrogen storage in the lithium borohydride—calcium hydride coupled system*. Journal of Alloys and Compounds, 464(1):L1–L4, September 2008.

[PP96] Porezag, Dirk and Mark R. Pederson: *Infrared intensities and Raman-scattering activities within density-functional theory*. Physical Review B, 54(11):7830–7836, September 1996.

[PSM+17] Pertot, Yoann, Cédric Schmidt, Mary Matthews, Adrien Chauvet, Martin Huppert, Vit Svoboda, Aaron von Conta, Andres Tehlar, Denitsa Baykusheva, Jean Pierre Wolf, and Hans Jakob Wörner: *Time-resolved x-ray absorption spectroscopy with a water window high-harmonic source*. Science, 355(6322):264–267, January 2017.

[PT64] Phillip, H. R. and E. A. Taft: *Kramers-Kronig Analysis of Reflectance Data for Diamond*. Physical Review, 136(5A):A1445–A1448, November 1964.

[Ram28] Raman, Chandrasekhara Venkata: *A new radiation*. Indian Association for the Cultivation of Science, 1928.

[Ray99] Rayleigh, John William Strutt: *Scientific papers*. Cambridge : University Press, 1899.

[RK28a] Raman, C. V. and K. S. Krishnan: *A New Type of Secondary Radiation*. Nature, 121(3048):501–502, March 1928.

[RK28b] Raman, C. V. and K. S. Krishnan: *The Optical Analogue of the Compton Effect*. Nature, 121(3053):711, May 1928.

[RLN16] Ramasesha, Krupa, Stephen R. Leone, and Daniel M. Neumark: *Real-Time Probing of Electron Dynamics Using Attosecond Time-Resolved Spectroscopy*. Annual Review of Physical Chemistry, 67(1):41–63, 2016.

[RPJG+99] Rose-Petruck, Christoph, Ralph Jimenez, Ting Guo, Andrea Cavalleri, Craig W. Siders, Ferenc Rksi, Jeff A. Squier, Barry C. Walker, Kent R. Wilson, and Christopher P. J. Barty: *Picosecond–milliångström lattice dynamics measured by ultrafast X-ray diffraction*. Nature, 398(6725):310–312, March 1999.

[RRU+97] Rischel, Christian, Antoine Rousse, Ingo Uschmann, Pierre Antoine Albouy, Jean Paul Geindre, Patrick Audebert, Jean Claude Gauthier, Eckhart Fröster, Jean Louis Martin, and André Antonetti: *Femtosecond time-resolved X-ray diffraction from laser-heated organic films*. Nature, 390(6659):490–492, December 1997.

[RSL+08] Racu, A. M., J. Schoenes, Z. Lodziana, A. Borgschulte, and A. Züttel: *High-Resolution Raman Spectroscopy Study of Phonon Modes in LiBH4 and LiBD4*. The Journal of Physical Chemistry A, 112(40):9716–9722, October 2008.

[RWJ+87] Ruhman, S., Leah R. Williams, Alan G. Joly, Bern. Kohler, and Keith A. Nelson: *Nonrelaxational inertial motion in carbon disulfide liquid observed by femtosecond time-resolved impulsive stimulated scattering*. The Journal of Physical Chemistry, 91(9):2237–2240, April 1987.

[RWJ+96] Raksi, Ferenc, Kent R. Wilson, Zhiming Jiang, Abdelaziz Ikhlef, Christian Y. Cote, and Jean Claude Kieffer: *Ultrafast x-ray absorption probing of a chemical reaction*. The Journal of Chemical Physics, 104(15):6066–6069, April 1996.

[SB51] Salpeter, E. E. and H. A. Bethe: *A Relativistic Equation for Bound-State Problems*. Physical Review, 84(6):1232–1242, December 1951.

[SBA+03] Saes, Melanie, Christian Bressler, Rafael Abela, Daniel Grolimund, Steven L. Johnson, Philip A. Heimann, and Majed Chergui: *Observing Photochemical Transients by Ultrafast X-Ray Absorption Spectroscopy*. Physical Review Letters, 90(4):047403, January 2003.

[SCC+00] Schoenlein, R. W., S. Chattopadhyay, H. H. W. Chong, T. E. Glover, P. A. Heimann, C. V. Shank, A. A. Zholents, and M. S. Zolotorev: *Generation of Femtosecond Pulses of Synchrotron Radiation*. Science, 287(5461):2237–2240, March 2000.

[SCST+99] Siders, C. W., A. Cavalleri, K. Sokolowski-Tinten, Cs Tóth, T. Guo, M. Kammler, M. Horn von Hoegen, K. R. Wilson, D. von der Linde, and C. P. J. Barty: *Detection of Nonthermal Melting by Ultrafast X-ray Diffraction*. Science, 286(5443):1340–1342, November 1999.

[Shi04] Shirley, Eric L.: *Ti 1s pre-edge features in rutile: a Bethe-Salpeter calculation*. Journal of Electron Spectroscopy and Related Phenomena, 136(1):77–83, May 2004.

[SLC+96] Schoenlein, R. W., W. P. Leemans, A. H. Chin, P. Volfbeyn, T. E. Glover, P. Balling, M. Zolotorev, K. J. Kim, S. Chattopadhyay, and C. V. Shank: *Femtosecond X-ray Pulses at 0.4 Å Generated by 90° Thomson Scattering: A Tool for Probing the Structural Dynamics of Materials*. Science, 274(5285):236–238, October 1996.

[SLR+15] Santomauro, F. G., A. Lübcke, J. Rittmann, E. Baldini, A. Ferrer, M. Silatani, P. Zimmermann, S. Grübel, J. A. Johnson, S. O. Mariager, P. Beaud, D. Grolimund, C. Borca, G. Ingold, S. L. Johnson, and M. Chergui: *Femtosecond X-ray absorption study of electron localization in photoexcited anatase TiO_2*. Scientific Reports, 5:14834, October 2015.

[SLS69] Sayers, D. E., F. W. Lytle, and E. A. Stern: *POINT SCATTERING THEORY OF X-RAY K-ABSORPTION FINE STRUCTURE,*. Technical report, July 1969.

[SRCY02] Soulié, J Ph, G Renaudin, R Cerny, and K Yvon: *Lithium boro-hydride LiBH4: I. Crystal structure*. Journal of Alloys and Compounds, 346(1):200–205, November 2002.

[SRP+14] Schultze, Martin, Krupa Ramasesha, C. D. Pemmaraju, S. A. Sato, D. Whitmore, A. Gandman, James S. Prell, L. J. Borja, D. Prendergast, K. Yabana, Daniel M. Neumark, and Stephen R. Leone: *Attosecond band-gap dynamics in silicon*. Science, 346(6215):1348–1352, December 2014.

[SSL71] Sayers, Dale E., Edward A. Stern, and Farrel W. Lytle: *New Technique for Investigating Noncrystalline Structures: Fourier Analysis of the Extended X-Ray—Absorption Fine Structure*. Physical Review Letters, 27(18):1204–1207, November 1971.

[Sto92] Stoehr, Joachim: *NEXAFS Spectroscopy*. Springer Series in Surface Sciences. Springer-Verlag, Berlin Heidelberg, 1992, ISBN 978-3-540-54422-7.

[SZF+12] Stingl, J., F. Zamponi, B. Freyer, M. Woerner, T. Elsaesser, and A. Borgschulte: *Electron Transfer in a Virtual Quantum State of LiBH 4 Induced by Strong Optical Fields and Mapped by Femtosecond X-Ray Diffraction*. Physical Review Letters, 109(14), October 2012.

[TCS+16] Tao, Zhensheng, Cong Chen, Tibor Szilvási, Mark Keller, Manos Mavrikakis, Henry Kapteyn, and Margaret Murnane: *Direct time-domain observation of attosecond final-state lifetimes in photoemission from solids*. Science, page aaf6793, June 2016.

[VSRK11] Vinson, J., E. L. Shirley, J. J. Rehr, and J. J. Kas: *Bethe-Salpeter Equation Calculations of Core Excitation Spectra*. Physical Review B, 83(11), March 2011. arXiv: 1010.0025.

[VTH83] Velsko, S., J. Trout, and R. M. Hochstrasser: *Quantum beating of vibrational factor group components in molecular solidsa)*. The Journal of Chemical Physics, 79(5):2114–2120, September 1983.

[VWJL+13] Vura-Weis, Josh, Chang Ming Jiang, Chong Liu, Hanwei Gao, J. Matthew Lucas, Frank M. F. de Groot, Peidong Yang, A. Paul Alivisatos, and Stephen R. Leone: *Femtosecond M2,3-Edge Spectroscopy of Transition-Metal Oxides: Photoinduced Oxidation State Change in a-Fe2o3*. The Journal of Physical Chemistry Letters, 4(21):3667–3671, November 2013.

[WLWN91] Weiner, A. M., D. E. Leaird, Gary P. Wiederrecht, and Keith A. Nelson: *Femtosecond multiple-pulse impulsive stimulated Raman scattering spectroscopy*. JOSA B, 8(6):1264–1275, June 1991.

[WRW+17] Weisshaupt, J., A. Rouzée, M. Woerner, M. J. J. Vrakking, T. Elsaesser, E. L. Shirley, and A. Borgschulte: *Ultrafast modulation of electronic structure by coherent phonon excitations*. Physical Review B, 95(8):081101, February 2017.

Erklärung zur Selbstständigkeit

Ich erkläre, dass ich die Dissertation selbständig und nur unter Verwendung der von mir gemäß §7 Abs. 3 der Promotionsordnung der Mathematisch-Naturwissenschaftlichen Fakultät, veröffentlicht im Amtlichen Mitteilungsblatt der Humboldt-Universität zu Berlin Nr. 42/2018 am 11.07.2018 angegebenen Hilfsmittel angefertigt habe.

Berlin, den , _____

Jannick Weißhaupt

Als Ansichtsexemplar genehmigt von

Berlin, den , _____

Prof. T. Elsässer